UNIVERSITY BREMEN
Master's Thesis MSc. Environmental Physics

Roughness and backscatter of the Nansen Sound sea ice plug

Mara Neudert
6008272

born in Erfurt, Germany

Supervisors:
Prof. Dr. Christian Haas
Dr. Christian Melsheimer

This thesis has been carried out with the
Sea Ice Physics Section, Alfred Wegener Institute for Polar and
Marine Research, Bremerhaven

11th August 2021

Abstract

Roughness and backscatter of the Nansen Sound sea ice plug

by Mara Neudert

The roughness of sea ice is a critical factor for the interactions between ice, atmosphere, and ocean. Roughness is interrelated with melt season processes, and sensitive to changing Arctic climatic conditions. Nansen Sound ice plug offered an opportunity to study multiyear ice (MYI) surface and bottom roughness evolution alongside Sentinel-1 backscatter changes over two consecutive melt seasons. Ice thickness and surface profiles were acquired in springs 2017, 2018, and 2019 using airborne electromagnetic induction sounding and single-beam laser altimetry. The mean ice plug thickness increased from 1.9 m in 2017 to 2.4 m in 2019.

The surveys in 2017 and 2019 included 2D surface topography from airborne laser scanning (ALS). After adapting the method developed by Hibler III (1972) for filtering of aircraft altitude variations from the single-beam profiles, we compared roughness obtained with both instruments. The root mean square (RMS) height in 50-m windows decreased slightly for the altimeter profiles while it stayed constant for the ALS digital elevation models. Roughness was also estimated from power spectral densities, and the findings are in support of a constant RMS height.

The unaltered topography, despite expected roughening from non-uniform summer ablation, was attributed to the snow cover, which masked those differences. The bottom roughness, which is represented by the ice thickness, shows a decrease in mean RMS height of about 30% on scales of 50–1000 m.

Melt pond distributions from Sentinel-2 true color images showed that spring roughness did not co-vary with summer melt pond pattern. Ice thickness was about 40 cm lower in pond covered sections of the three-year-old ice in 2019, while in 2017 this difference was only 20 cm.

The Sentinel-1 backscatter σ^0_{HH} of the ice plug increased from -21 dB in spring 2017 to -13 dB in spring 2019. The incidence angle dependence decreased over the first melt season from -0.26 dB/1° to -0.15 dB/1°. This increase in backscatter and the decrease in slope is expected for enhanced contribution of volume scattering from air bubbles in the surface ice layers of MYI.

From ERA5 Land climate reanalysis data we computed lower mean summer temperatures, significantly less melting degree-days, and later melt onsets for the years 2017 and 2018, where the ice plug was stable, compared to 2016 and 2019 where the ice disintegrated in August.

Our results demonstrate the usefulness of studying fast ice for fundamental sea ice processes and remote sensing.

List of Abbreviations

ACF	Autocovariance function
ALS	Airborne laser scanning
CAA	Canadian Arctic Archipelago
DEM	Digital elevation model
DGPS	Differential GPS
EM	Electromagnetic
FDD	Freezing degree day
FYI	First-year ice
MDD	Melting degree day
MYI	Multiyear ice
PSD	Power spectral density
RMS	Root mean square
QEI	Queen Elizabeth Islands
S1	Sentinel-1
S2	Sentinel-2
SAR	Synthetic aperture radar
SYI	Second-year ice

Contents

1 Introduction

Local and global climate is impacted by the presence of sea ice and by ice-atmosphere and ice-ocean interactions. The formation of sea ice with a high albedo results in a larger portion of short-wave solar radiation being reflected to space. In the presence of sea ice, the sensible and latent heat flux between atmosphere and ocean are reduced. Furthermore, latent heat for freezing and thawing of sea ice acts as a thermal reservoir, delaying the seasonal temperature cycle. Ocean salinity, and thereby density stratification, is altered by expulsion of brine during freezing and transport of low-salinity ice (Ebert and Curry, 1993).

Sea ice can be classified into several types, the main ones being young ice, first-year ice (FYI), and multiyear ice (MYI). Young ice is up to 30 cm thick, newly formed ice. FYI has grown to a thickness of more than 30 cm thickness during one cold season. MYI has survived at least one melt season and its thickness is increasing with age (WMO-IOC et al., 2014). Landfast sea ice is "sea ice which remains fast along the coast, where it is attached to the shore, to an ice wall, to an ice front, or over shoals, or between grounded icebergs" (Armstrong, 1972). The semi-permanent ice plug across the northern opening of Nansen Sound in the Queen Elizabeth Islands (QEI) in the Canadian Arctic Archipelago (CAA) is a MYI landfast ice feature, and one of two ice plugs that are known to have existed over the past century in the Arctic. In Copland and Mueller (2017), ice plugs are defined as small areas of consolidated perennial sea ice that formed between narrow points. Ice plugs are characterized by their historical longevity and presence over decades. Land on both sides acted as an anchor for the thick ice (Copland and Mueller, 2017).

Ice thickness distributions must be known to represent ice dynamics in high-resolution models accurately, assess the ice mass balance, and evaluate risks for marine operations. Ice thickness, in contrast to sea ice extent, is difficult to determine from satellite observations (Haas and Howell, 2015). Different ice types, and snow cover, cause sea ice density differences, hampering ice draft estimations from radar altimetry (Kern et al., 2015; Belter et al., 2020). For validation and intercomparison, ground-based sea ice draft and freeboard, along with snow depth data, need to be acquired.

Arctic sea ice extent, MYI fraction and thickness are decreasing (Comiso, 2012; Haas et al., 2008). Momentum and energy transfer between atmosphere-ice and ice-ocean are shifting, causing larger drift speeds. Leads between floes are increasing, and hence higher deformation rates from rafting and ridging. Simultaneously, MYI which typically has topographic features higher but smoother than those of FYI (Tschudi et al., 2016), is lost. This implies an increase in roughness, consequently affecting melt pond distributions and in turn changing energy balance and roughness characteristics (Beckers et al., 2015).

Roughness representation of sea ice surface is crucial for modeling and measuring drag, drift, and the vertical transport of water. Hazard assessment for marine operations requires information about roughness and thickness relations (Beckers et al., 2015). Ice roughness, as determined by deformation and aging processes, explains a significant portion of the contrasts in pond coverage and albedo between ice of different ages, and prediction of melt pond fraction is a current research subject.

The sea ice surface roughness characteristics, e.g., height and slope, are critical for electromagnetic scattering. Knowledge of roughness is therefore needed to improve identification of various ice types, retrieval of ice thickness, surface temperature and drag coefficient from satellite remote sensing data (Liu et al., 2014).

Macroscopic roughness includes a range of features on different scales. Pressure ridges, cracks, leads, ice rubble, rafted ice and hummocks are caused by dynamic deformation processes. Additionally, melt features, e.g., ponds, drainage channels, and slush are present on MYI. Ice roughness is partly obscured and altered by snow cover with dunes and sastrugis. Melt processes in summer are expected to smooth pressure ridges, while melt ponds increase the surface roughness due to the generation of vertical pond walls in former level ice areas (Von Saldern et al., 2006).

Microwave remote sensing offers the potential to effectively monitor numerous sea ice properties such as ice extent, concentration, type, and thermodynamic state, that are of interest to climate research and operational ice monitoring. C-Band SAR imaging is partially sensitive to ice surface roughness on the centimeter scale, but also to physical properties of the bulk ice.

From autumn 2016 to summer 2019, Nansen Sound ice plug stayed intact and provided the opportunity to observe the inter-annual evolution of landfast MYI throughout three years (two melt seasons). With the EM Bird towed by a Basler BT-67 three flights were conducted in springs 2017, 2018, and 2019. Ice thickness and surface height profiles were obtained by airborne electromagnetic (EM) induction sounding and single-beam laser altimetry. In addition, an airborne laser scanner (ALS) and a snow radar were employed on the flights in 2017 and 2019.

The use of laser scanners is motivated by the potential to gain new insights into 2D anisotropy of the topography of the sea ice/snow surface. Greater understanding of presumable surface roughness changes resulting from the more seasonal Arctic sea-ice regime, and improved up-scaling of in-situ to satellite data were anticipated from the use of ALS over single-beam altimeters (Beckers et al., 2015).

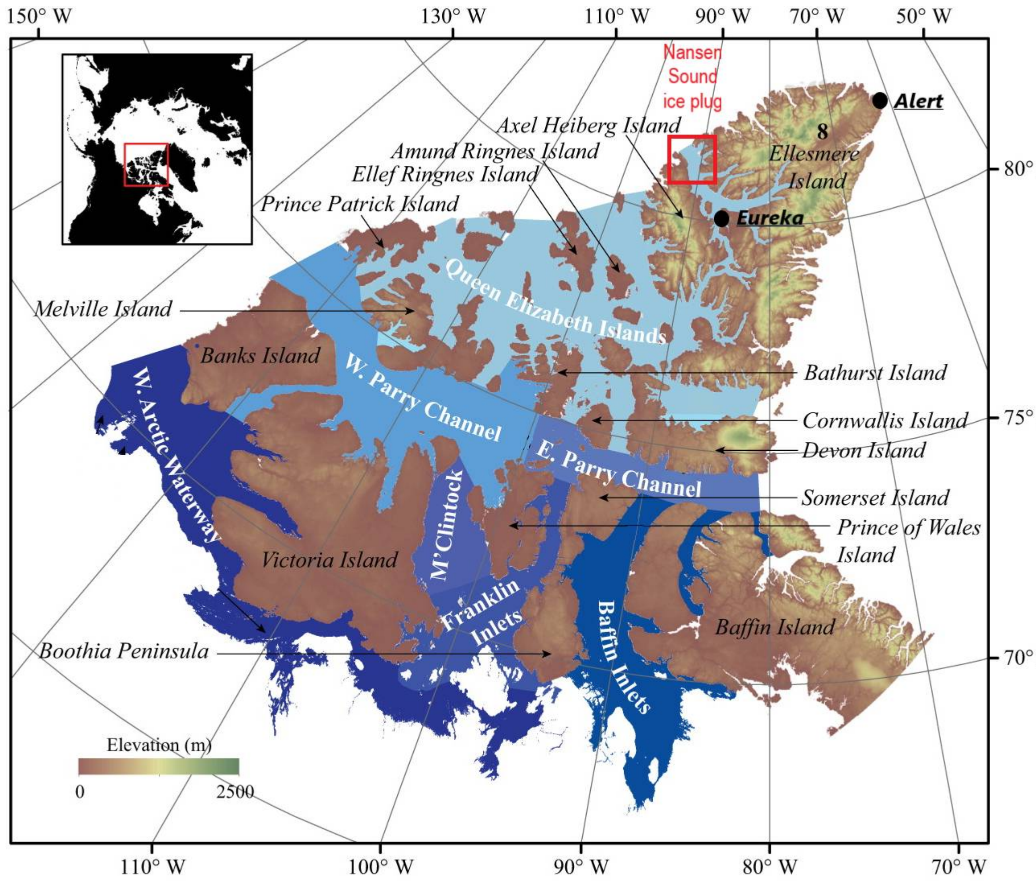

Fig. 1.1: Map of the Canadian Arctic Archipelago. Adapted from Dauginis and Brown (2021).

1.1 Objectives

The dataset of airborne measurements allowed to deduce the evolution of surface and bottom roughness parameters. The immobile ice enabled studying aspects of sea ice evolution through consecutive melt pond formation in summer and ice growth in winter that are poorly represented in climate models (Nasonova et al., 2018) and difficult to observe on mobile ice.

1.1.1 Comparison of altimeter and ALS derived surface roughness

We aim to compare the capabilities (as well as their limitations) of 1D surface profiles with 2D elevation models from ALS as a prerequisite for the subsequent surface roughness characterization. To achieve this, the altimeter data first needs to be filtered, which is a secondary objective in this work.

Processing of altimeter data

Two methods for filtering flight altitude variations from the single-beam altimeter range signal were implemented and tested with the aim to improve the method developed by Hibler III (1972).

1.1.2 Ice thickness and roughness evolution

Different roughness metrics e.g., root mean square (RMS) height, RMS slope, skewness, and kurtosis were obtained from height profiles from the single-beam laser altimeter and the laser scanner DEMs. To study the evolution of roughness over two years, a number of assumptions were tested:

The level ice in 2017 was expected to be smooth as the initial condition. The macro-scale ice surface roughness was anticipated to increase by melt season processes, where melt ponds form in topographic depressions and preferential melting occurs at sites of melt ponds (Landy et al., 2014). The melt pond distribution on Nansen Sound ice plug was obtained from Sentinel-2 images in order to discriminate between surfaces with different genesis. The smoothing of ridges cannot be taken into account since there was no ice with prominent ridges surveyed in 2017 and 2019; ice with ridges was only surveyed in 2018. It was expected that enhanced snow accumulation in depressions created by melt ponds and snow drifts obscures ice surface roughness in spring.

The surface roughness was compared to bottom roughness, derived from the EM ice thickness measurements. To our knowledge, no specific studies have been carried out to address the bottom roughness evolution of landfast MYI, but we assume the bottom roughness to be decreasing. Inter-annual changes in the ice thickness distribution might be attributed to the interplay between preferential thinning of pond-covered areas in summer and higher growth rates for thinner ice in winter.

1.1.3 Sentinel-1 backscatter evolution

Tying in with surface roughness changes over time, we aim to determine and interpret the C-band SAR backscatter evolution based on surface topography and the ice's developmental history. Incidence angle dependence of backscatter in Sentinel-1 EW product was determined and is expected to decrease after the first melt season due to altered surface layer properties enhancing volume scattering. For the same reason we expect the mean backscatter to increase with ice age.

1.1.4 Role of climatic conditions for stability

In the period from 2005 to 2020, Nansen Sound ice plug has stayed intact for only four out of the 16 years, compared to 15 out of the 16 years prior to 2005, indicating a change in the regional climate (Copland and Mueller, 2017). The meteorological conditions during the study period were assessed with the ERA5 Land reanalysis product. Radiation balance, cumulative melting-degree days (MDD), melt period duration, and wind directions were computed for 2016 to 2019. We hypothesized that inter-annual differences in summer temperatures could explain the ice plug breakup in 2016 and 2019, and the stability of the plug in 2017 and 2018. Comparative information was gathered by Copland and Mueller (2017).

2 Scientific background

2.1 The evolution of sea ice

2.1.1 Sea ice growth

Initial formation of sea ice occurs when sea water reaches its salinity-adjusted freezing point as fine spicules or plates of ice, suspended in water, called frazil ice (WMO-IOC et al., 2014). With further frazil formation, coagulates termed grease ice form. Under calm sea conditions, the formation of a thin elastic crust, the nilas, of up to 10 cm thickness follows. Under rougher conditions the frazil ice accumulates in pans that collide and thereby thicken at the edges, forming pancake ice. Eventually all pans freeze together. In WMO terms, all types of ice of frazil origin are summed up under new ice and are characterized by high salinity and random crystal orientation (Thomas and Dieckmann, 2008).

Subsequent congelation growth forms a layer of horizontally oriented crystals, usually 5 to 10 cm thick. Below this layer, further congelation growth has horizontally oriented crystals. Growth of sea ice is determined by the temperature gradient through the ice cover and the effective thermal conductivity of the ice, thereby affecting the conductive heat flux through the ice and the oceanic heat flux into the ice. The conductive heat flux at the bottom is balanced by the oceanic heat flux and the release of latent heat when ice grows. Snow acts as an insulator, due to its lower effective heat conductivity. Brine cells in the ice act as a thermal reservoir. If oceanic heat flux, radiation balance, snow properties, and turbulent fluxes are treated as constant, freezing degree-day models are the simplest way to model thermodynamic ice growth, using only air temperature as input variable (Thomas and Dieckmann, 2008).

Over time, salinity of sea ice undergoes changes. During formation, salt ions are not incorporated into the crystal lattice and instead accumulate within pores of the brine cells. The brine remains in thermal equilibrium with the surrounding ice.

The brine continues to be rejected slowly throughout the entire growing season of the first-year ice sheet. The primary mechanism is gravity drainage, where the denser brine is driven out of the seawater-ice interface through a network of near-vertical drainage channels (Shokr and Sinha, 2015).

Other desalination mechanisms are brine expulsion, where decreasing temperatures increase pressure in the cells, such that the brine gets expelled, downwards to more porous ice. Temperature gradients in the ice leave the upper end of brine cells more saline. Diffusion of salt causes the upper end to freeze and the lower end to thaw, consequently brine cells migrate downwards. During the beginning of the melt season brine cell flushing results from the vertical percolation of surface melts (Shokr and Sinha, 2015).

2.1.2 Sea ice decay

Melting starts when the surface energy balance becomes positive, first causing wetting and metamorphism of the snowpack. Snow and sea ice temperatures increase until an isothermal state is reached. At melt onset, the water cannot be held by the snow and drains to the snow-ice interface. Meltwater pools on the ice surface and changes the albedo and thereby the energy budget of the sea ice. Perovich et al. (2002), reported that distinct phases of seasonal albedo are linked to melting: dry snow cover with albedo between 0.8–0.9, melting snow (decrease from 0.8 to 0.7), pond formation (decrease from 0.7 to 0.5), pond evolution (decrease from 0.5 to 0.4), and fall freeze-up (increase from 0.4 to 0.8).

Melt ponds develop over consecutive stages with (1) topographic control, (2) hydrostatic balance, and (3) ice freeboard control. The spatial distribution of melt ponds during the first stage is largely defined by premelt ice topography (on smooth ice also by snow drift pattern). As the pond surface lies above sea level, drainage is limited. At the end of the first stage, melt pond coverage peaks (Landy et al., 2014). In the second stage, meltwater production and drainage are balanced by lateral flow of meltwater and vertical percolation. At the end of this stage, the hydraulic head reaches zero. During the third stage, changes in pond coverage are controlled by changes in freeboard. Ponds deepen due to preferential melting and can expand due to erosion of the walls.

2.1.3 Multiyear ice

At the end of the melt season, the ice that has survived will resume to thicken by congelation growth. Under constant annual climate cycles, the ice would reach equilibrium thickness between 2.5 and 5 m for thermodynamically grown MYI, depending on the climatic regime. Equilibrium would be attained in 10 to 15 years (Maykut and Untersteiner, 1971). MYI has distinctly lower salinity than FYI, making it mechanically stronger, and has a surface that is shaped by melt ponds. Deformed FIY is rough and angular. MYI on the other hand, is described as having a smoother, rolling surface (Shokr and Sinha, 2015).

2.2 Nansen Sound ice plug

Observations by Jeffries et al. (1992) describe the plug as a matrix of different ice ages and thicknesses which are subject to rearrangement. The Beaufort Gyre pushes thick, old ice from the central Arctic Basin into the narrow channels where it can get pinned by land. Intruding MYI floes freeze-in during winter, and basal freezing and snow accumulation thicken the ice. Historically, melting and in-situ fracturing were observed, but the Nansen Sound ice plug remained mostly land-fast between 1961 and 2016 (Copland and Mueller, 2017).

Nansen Sound broke up in 1962, 1971, 1998 and yearly from 2005 to 2012 (with an incomplete breakup in 2006), and again in 2015 and 2016 (Fig. 2.1). The breakup events of Sverdrup and Nansen plug were attributed to climate and synoptic conditions (Copland and Mueller, 2017). The 1998 breakup was linked to rapid melting during a warm summer, characterized by mean temperatures above 5° C at Eureka, an early melt onset, and long warm periods. Strong surface melting weakened the mechanical strength of the plug structure. Of further importance were high proportions of open water to the north of the ice plug, which impaired the protective matrix of the adjacent ice, simultaneous with strong storm systems moving through the Queen Elizabeth Islands (QEI), which fractured the weakened ice (Jeffers et al., 2001).

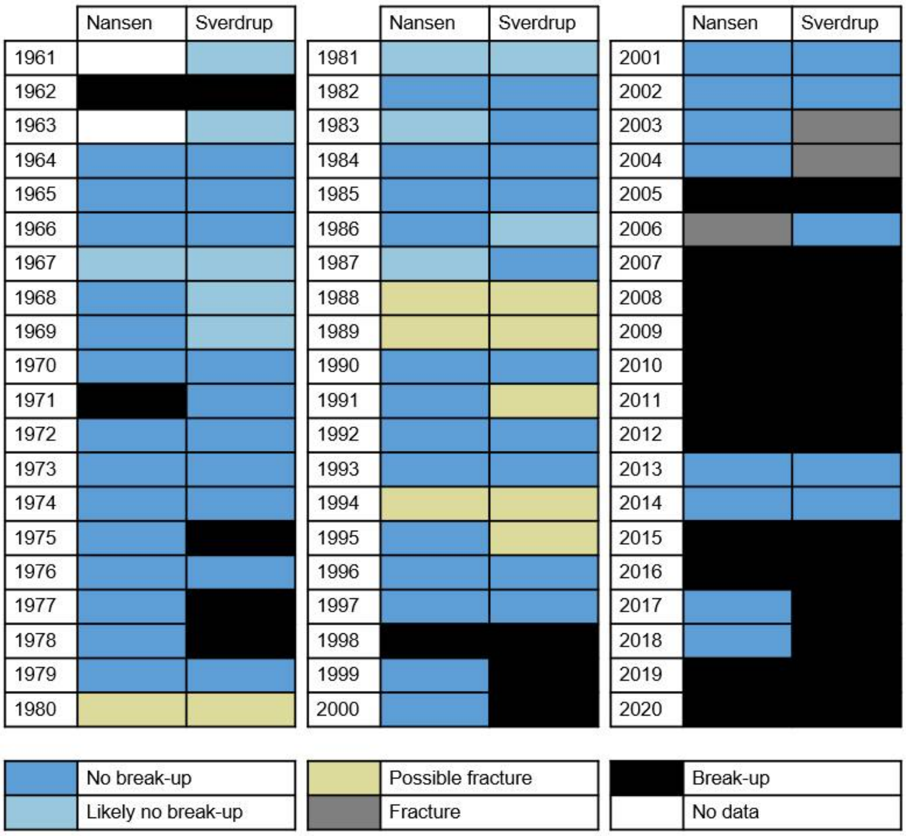

	Nansen	Sverdrup		Nansen	Sverdrup		Nansen	Sverdrup
1961	⬜	▨	1981	▨	▨	2001	🟦	🟦
1962	⬛	⬛	1982	🟦	🟦	2002	🟦	🟦
1963	⬜	▨	1983	▨	🟦	2003	🟦	▩
1964	🟦	🟦	1984	🟦	🟦	2004	🟦	▩
1965	🟦	🟦	1985	🟦	🟦	2005	⬛	⬛
1966	🟦	🟦	1986	🟦	▨	2006	▩	🟦
1967	▨	▨	1987	▨	🟦	2007	⬛	⬛
1968	🟦	▨	1988	🟨	🟨	2008	⬛	⬛
1969	🟦	▨	1989	🟨	🟨	2009	⬛	⬛
1970	🟦	🟦	1990	🟦	🟦	2010	⬛	⬛
1971	⬛	🟦	1991	🟦	🟨	2011	⬛	⬛
1972	🟦	🟦	1992	🟦	🟦	2012	⬛	⬛
1973	🟦	🟦	1993	🟦	🟦	2013	🟦	🟦
1974	🟦	🟦	1994	🟨	🟨	2014	🟦	🟦
1975	🟦	⬛	1995	🟦	🟨	2015	⬛	⬛
1976	🟦	🟦	1996	🟦	🟦	2016	⬛	⬛
1977	🟦	⬛	1997	🟦	🟦	2017	🟦	⬛
1978	🟦	⬛	1998	⬛	⬛	2018	🟦	⬛
1979	🟦	🟦	1999	🟦	⬛	2019	⬛	⬛
1980	🟨	🟨	2000	🟦	⬛	2020	⬛	⬛

🟦	No break-up	🟨	Possible fracture	⬛	Break-up
▨	Likely no break-up	▩	Fracture	⬜	No data

Fig. 2.1: Recorded breakup and fracture events of the Nansen and Sverdrup ice plugs from 1961–2020. Adapted from Copland and Mueller (2017)

2.2.1 Historical ice thickness measurements

Ice thickness of the Nansen Sound ice plug in 1970–1971 was reported to increase from 6 m to 10 m southwards (Copland and Mueller, 2017). Before the breakup in 1971, the plug extended 53 km with hummock heights increasing from 1.5 m to 3 m from northeast to southwest with an average ice thickness of 4 m (Serson, 1972). The ice was 21 to 39 years old at that time.

The ice plug had regrown to an extent of 26 km by 1979. In 1980 newly added sections of second-year ice were attached at both ends. Sadler and Serson (1981) observed the ice plug's surface height variations qualitatively in March 1980 as less pronounced compared to 1971, with hummocks of 1–2 m height and the northeast smoothed by packed snow. When they returned in October they found hummocks of 1.5–2.5 m height with vertical melt pond walls of 0.5–1 m.

They also conducted ice thickness measurements along a transect in October 1980. The second-year ice strip at the southern edge was on average 3.5 m thick and the older part had a mean thickness of 5 m (maximum 8.65 m on an ablated ridge, minimum 0.3 m on a refrozen lead).

With respect to stability of the ice plug, they assessed that the tidal cracks "are small and do not appear to be working", but tension cracks (from temperature gradients or between different ice types) exist and seemed to begin at points of stress with the land (Sadler and Serson, 1981).

2.3 Ice thickness in the CAA

Records of landfast ice thickness provide annual measures of ice growth that can almost entirely be attributed to atmospheric forcing with negligible deep ocean influence on local ice formation (Howell et al., 2016). Thus, the seasonal behavior of landfast ice, such as Nansen Sound ice plug, can provide useful information for understanding the interannual variability of ice thickness in both landfast and offshore ice.

Weekly ice thickness and snow thickness measurements of landfast FYI from 1960–2014 at Eureka and Alert station (Fig. 1.1) showed linear ice thickness growth over the winter season, peaking in late May at 2.27±0.23 m and 1.98±0.22 m, respectively. The mean snow thickness is 17.6±5.8 cm at Eureka and 18.4±6.2 cm at Alert for the period Oct–May. Over the 50-year record, ice thinning is statistically significant with 0.24 m and 0.26 m at Eureka and Alert, respectively. The months March–May exhibit a warming trend of 0.32–0.44 °C/decade, June–August 0.1–0.21 °C/decade and Sept–Oct 0.66–0.68°C/decade with the largest warming at Eureka (Howell et al., 2016).

Inter-annual variability in ice thickness was largely attributed to differences in snow thickness. For years where snow thickness reached about 30 cm in April, e.g. 2005–2006, the ice at Eureka was 70 cm thinner compared to years where snow depth peaked at 15 cm e.g., winter 1966-1967 (Howell et al., 2016).

The ocean adjacent to the northern opening of Nansen Sound is covered by the thickest and most heavily ridged sea ice in the world. The ice is typically older than four years (Maslanik et al., 2007) and regional mean ice thickness can reach 5 m (Haas and Howell, 2015). Ice adjacent to the QEI circulates within the anticyclonic Beaufort Gyre that may trap ice for several decades. High ice pressure and shear along the northwest coast of the QEI result from this motion, creating the deformed ice floes, which drift into the sounds and may have characteristics significantly different from locally-formed ice (Melling, 2002).

2.4 Roughness of sea ice

Sea ice has a surface topography that is a superposition of roughness on different scales. This can be attributed to different physical forcings. Bare ice, snow grains, and frost flowers with scales less than 10 cm make up the micro-scale roughness, largely responsible for surface scattering in the microwave regime.

Measured surface profiles in this work have a resolution of about 25 cm for the ALS, 50 cm for the single beam altimeter profiles, and 5 m for ice thickness measurements. Roughness on the micro-scale cannot be resolved.

Macro-scale roughness (mainly snowdrifts, melt pond walls) up to a scale of 100 m become dominant. On larger scales roughness is determined by the type of ice, namely ridged or level ice (Landy et al., 2015).

Quantifying surface roughness in the natural environment remains a challenge. For airborne measurement acquisition, footprint-scale uncertainties associated with sensor position (yaw and pitch angles, and slant range distortion) and the absence of a level reference surface on MYI complicate the retrieval of meaningful roughness parameters (Nasonova et al., 2018).

Beckers et al. (2015) compared the traditional method of single-beam laser altimetry with airborne laser scanning. They estimated the surface roughness for the altimeter with the standard deviation of the relative surface elevation in five-data-point moving windows, then compared this parameter to the standard deviation of the relative surface elevation from each scan line for the laser scanner. Off-nadir features (blocks, ridges) were missed by the laser altimeter, leading to an over- or underestimation of roughness by the altimeter, dependent on feature direction and location. For some flights in the Fram Strait, subsections at any fraction of the complete profile length did not reproduce the statistics of the complete flight, indicating strong heterogeneity in roughness. Their results imply non-stationary characteristics of the statistical properties of the sea ice surface in the Fram Strait.

2.4.1 Roughness linked to melt season processes

Landy et al. (2014) describe the surface topography evolution linked to melt ponds on seasonal landfast FYI in the CAA with terrestrial laser scanning and snow and ice sampling. They found that during Stage 1 melt ponds formed in local topographic depressions on all but the highest premelt elevations. Melt ponds were confined within the lowest 0.2 m of premelt surface heights on the smoother sea ice in 2012, compared to the lowest 0.6 m on the (relatively) rougher ice in 2011. In both years, the coverage remained high across a wide range of premelt elevations throughout Stage 2 and 3, indicating that the depth of those ponds that initially formed at higher elevations must have deepened to ensure a hydraulic head of zero everywhere. They found melt pond walls steepening in the late melt season in 2011.

Attempts have been made to quantify relationships between winter sea ice thickness, winter surface roughness, and spring melt pond fraction for an area comprising a mixture of landfast FYI and MYI in the CAA (Nasonova et al., 2018). From RADARSAT-2 Fine Quad-polarization SAR images, objects representing unique ice floes in Victoria Strait in April 2015 were created. GeoEye image pixels were classified as either melt pond or ice. Classified surfaces were overlapped by the footprint (120 m) of an airborne EM ice thickness and 2D laser scanner survey conducted in April, resulting in a melt pond fraction per floe within the footprint and an according estimate of mean ice thickness and roughness.

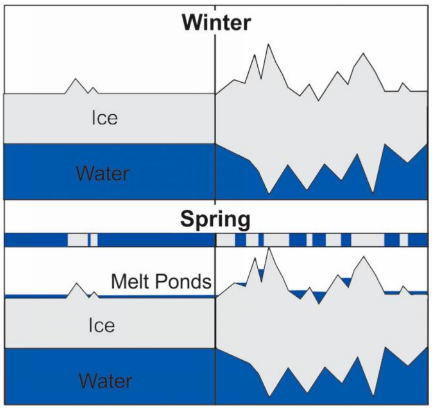

Fig. 2.2: Schematic of melt pond formation hypothesis as described by Landy et al. (2014) and Nasonova et al. (2018). Winter cross-section of pre-melt conditions of thin smooth sea ice and thick rough sea ice. Corresponding spring cross-section, showing smooth ice covered extensively by melt ponds. Right panel shows lower melt pond coverage due to high surface topography variation. Blue and grey bar in the center illustrates the melt pond extent as seen from above. Adapted from Nasonova et al. (2018).

A strong negative correlation between mean thickness and melt pond fraction for FYI and MYI was found and attributed to deformation, as illustrated in Fig. 2.2. FYI with small mean thickness that has not undergone dynamic forcing is smooth, and hence will experience widespread flooding. Conversely, FYI that has undergone ridging will constrain melt water into deeper surface depressions. Furthermore, a moderate negative correlation of surface roughness with melt pond fraction for FYI was found, however no statistically significant correlation for melt pond fraction was found for MYI. Differential weathering could explain the absence of a pond fraction–roughness correlation for MYI. MYI that is rough on large scales can comprise smooth sections from earlier melting seasons. These sections can become flooded easily, leading to a higher melt pond fraction than on uniformly weathered, smoother MYI.

Nasonova et al. (2018) further noted that on the scales of the floes (0.01–0.31 km^2), snow roughness masked the ice surface roughness. Using 2.4 km long moving averages removed the snow redistribution roughness. For the smoothed surface roughness the correlation strength between FYI roughness and melt pond fraction increased.

2.5 Roughness characterization

Surface roughness (or simply roughness) describes the interface between two media. Roughness is quantified by the random height deviation from the quasi-deterministic plane approximation of a larger region. Plenty of methods exist to quantify roughness on a mean surface, assuming that only random variations exist.

Statistical methods can be divided into parametric and functional. Commonly used parametric estimators for sea ice surface roughness are e.g., RMS height σ (Segal et al., 2020) along with skewness, and kurtosis (Beckers et al., 2015;

Von Saldern et al., 2006; Liu et al., 2014). Also RMS of the average local slope (Liu et al., 2014) can be used as a proxy for roughness.
Functional methods are capable of representing roughness at a large range of wavelengths. Frequently used are autocorrelation functions, from which correlation lengths l_c are calculated e.g., Von Saldern et al. (2006) and Liu et al. (2014). Power spectral density functions are also used to describe surface roughness across different spatial scales (Hibler and LeSchack, 1972; Liu et al., 2014).
Sea ice surface roughness is highly scale-dependent, ranging from scales of a specific feature (cm) to whole sea-ice floes (km). In general, roughness of natural surfaces is only poorly modeled by a stationary random process. Mean height, standard deviation, standard deviation of the slope, and autocorrelation length do not represent estimates of the true values in this case. They are not constant, but depend on the profile length, and thus cannot be used to compare profiles across different length scales (Von Saldern et al., 2006).

2.5.1 RMS height, RMS slope, skewness, and kurtosis

For sampled profiles, the longest wavelength contributing to the roughness calculation is inherently limited by the profile length. The shortest measurable wavelength is twice the sample spacing, according to the Nyquist sampling theorem. Those bandwidth limits cause errors for a profile with N samples, given by $z_n = z(x_n)$, that would not occur for continuous and finite functions. Therefore, all expressions for numerical values are called estimators, commonly indicated by a hat over the estimated quantity (Stover, 2012).
The **root mean square height** of the discrete, random one-dimensional surface profile with N height measurements z_n along x_n is estimated by

$$\sigma \cong \hat{\sigma} = \left[\frac{1}{N-1} \sum_{n=0}^{N-1} \left(z_n^2 - \hat{\bar{z}} \right)^2 \right]^{1/2} \tag{2.1}$$

where N is the number of samples and the mean is $\hat{\bar{z}} = \frac{1}{N} \sum_{n=0}^{N-1} z_n$ and $n = 0, 1, 2, ...N-1$ (Stover, 2012). The **root mean square slope** m is estimated by

$$m \cong \hat{m} = \left[\frac{1}{N-1} \sum_{n=1}^{N-1} \left(\frac{z_n - z_{n-1}}{x_n - x_{n-1}} - \hat{\bar{z'}} \right)^2 \right]^{1/2} \tag{2.2}$$

where

$$\hat{\bar{z'}} = \frac{1}{N-1} \sum_{n=1}^{N-1} \left(\frac{z_n - z_{n-1}}{x_n - x_{n-1}} \right) \tag{2.3}$$

σ is related to the distribution function $P(z)$ of surface heights by the second central moment

$$\sigma = \left[\int_{-\infty}^{+\infty} z^2 P(z) dz \right]^{1/2} \tag{2.4}$$

Higher moments of the distribution function can be used to describe non Gaussian properties of surface roughness. For the discrete case, **skewness** μ_3 and **kurtosis** μ_4 are estimated by

$$\mu_3 = \frac{1}{N\,\sigma^3} \sum_{n=0}^{N-1} \left(z_n - \hat{\bar{z}}\right)^3 \tag{2.5}$$

$$\mu_4 = \frac{1}{N\,\sigma^4} \sum_{n=0}^{N-1} \left(z_n - \hat{\bar{z}}\right)^4 \tag{2.6}$$

As the skewness of a normal distribution is zero, any symmetric data should have a skewness near zero. However, surface heights relative to the local level height have a lower bound at 0 and are expected to be skewed right, indicated by positive skewness values. Kurtosis is a measure of how broad a distribution is i.e., the amplitude of the modal peak in relation to the strength and length of the tails of the distribution. The kurtosis for a standard normal distribution is three, thus kurtosis is sometimes expressed as **excess kurtosis** by $\mu_4 - 3$. The excess kurtosis is used in this thesis and referred to as kurtosis from now on.

An illustration of skewess and kurtosis along with a surface profile at early and late melt season can be found in Fig. 2.3. With aging of the ice an increase in skewness is expected, resulting from the removal of the highest elevations by melting, compare to the idealized depiction of surface profiles with negative and positive in Fig. 2.3 A.

A surface shaped by drained melt ponds will have a smaller kurtosis than a snow covered surface in spring. An example of a surface profile at ears and late melt stage is shown in 2.3 B. In a simplified view, areas covered by melt ponds will reach a common low elevation at the end of the melt season, while ares unaffected by ponds retain their higher premelt surface elevation, hence a bi-modal component is introduced to the surface height distribution, leading to a smaller kurtosis.

In principle, all the parameters above can be calculated for two-dimensional profiles. However, calculating a slope always implies a fixed direction on the surface.

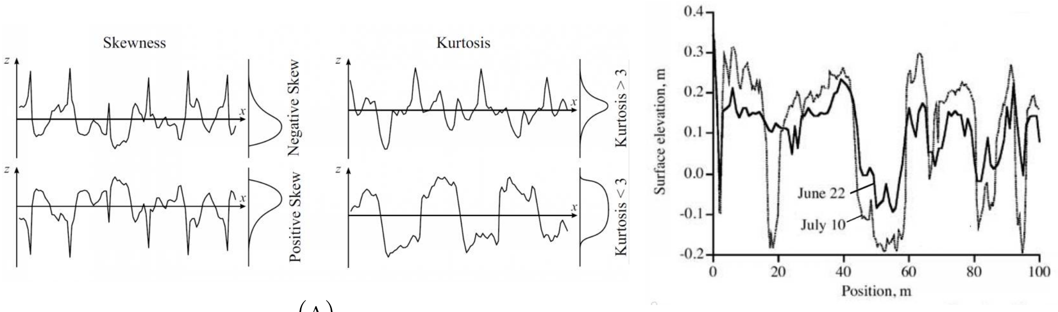

(A)

(B)

FIG. 2.3: (A) Illustration of profiles with different skewness and kurtosis, adapted from Magsipoc et al. (2020). (B) Example of a surface profile at early and late melt season, adapted from Eicken et al. (2004).

2.5.2 Power spectral density

Power spectral density function (PSD) and autocovariance function (ACF) can be calculated from the profile and enhance surface characterization beyond the profile parameters described in the previous section (conversely, they can be calculated calculated from the PSD). Stover (2012) states that the PSD is the preferred route because, as it expresses roughness as a function of spatial frequency, it displays the required bandwidth limits for the sampled profile. Furthermore, the PSD can be more accurately corrected for known deviations from ideal instrument response, which mis used to compare how well the flight altitude was filtered from the recorded altimeter heights.

Before generating the PSD estimator, the assumption that sample profile values represent the constant-mean surface microtopography only must be valid and the ACF depends on the lag distance only, which is that the process must fulfill weak-sense stationarity (see Florescu (2014), p. 299, for a definition of weak-sense stationarity).

The PSD of a continuous profile $z(x)$ of finite length L is calculated taking its Fourier transform

$$Z(f_x, L) = \int_{-L/2}^{L/2} z(x)\, \mathrm{e}^{-j2\pi f_x x}\, dx \tag{2.7}$$

where f_x denotes spatial frequency (in x direction) (Stover, 2012). The PSD function in one dimension, denoted as $S_1(f_x)$, is given by

$$PSD = S_1(f_x) = \lim_{L\to\infty} \frac{1}{L} \left| Z(f_x, L) \right|^2 \tag{2.8}$$

Various surface statistics can be found by calculating the even moments of the PSD. The odd moments evaluate to zero because of symmetry. Bandwidth-limited values of the RMS roughness and RMS slope are the zeroth and second order moment

$$\sigma^2 = 2 \int_{f_{min}}^{f_{max}} (2\pi f_x)^0 \, S_1(f_x) \, df_x \tag{2.9}$$

$$m^2 = 2 \int_{f_{min}}^{f_{max}} (2\pi f_x)^2 \, S_1(f_x) \, df_x \tag{2.10}$$

The factor 2 accounts for the integration over only the positive side of the symmetrical spectrum and f_{min} and f_{max} define the spatial bandwidth over which σ and m are defined (Stover, 2012).

Welch's method

Welch's method (Welch, 1967) is commonly used to estimate the PSD by sectioning the discrete profile $z(l), (l = 0, ..., N-1)$ into K segments of length L covering the entire record of length N. The expression for the PSD estimator for these sequences of L samples $z(l)$ is then

$$S_k(f_n) = \frac{L}{U} \left| \sum_{l=0}^{L-1} z_k(l) \, W(l) \, \exp\left(-\frac{j2\pi k \, l}{L} \right) \right|^2 \quad k = 1, 2, ..., K \tag{2.11}$$

where $f_n = n/L$ for $n = 0, ..., L/2$ and

$$U = \frac{1}{L} \sum_{l=0}^{L-1} W^2(l) \tag{2.12}$$

$W(j)$ is a window function to reduce "ringing" from the sudden on- and off-set at $l = 0$ and $L-1$ (Welch, 1967). The PSD estimate $S(\hat{f_n})$ is the average of the PSDs of the K sequences

$$\hat{S}(f_n) = \frac{1}{K} \sum_{k=1}^{K} S_k(f_n) \tag{2.13}$$

PSD of a sea ice surface profile

Hibler and LeSchack (1972) calculated power spectra of surface ice profiles from both young and multi-year ice laser profiles as observed during the winter in the central Polar Basin (fig. 2.4).

The Young Ice profile has a greater amplitude for all wavelengths shorter than 20 m, while for spatial periods longer than 20 m the Multiyear Ice has greater amplitude. Hibler and LeSchack (1972) interpret this as an effect of weathering, which smooths small scale roughness but adds undulations on longer spatial scales. They note that this was indeed observed in the field.

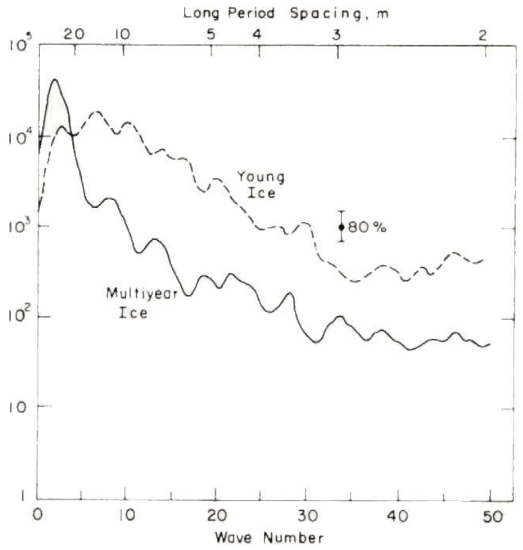

FIG. 2.4: Power spectra of two sea ice surface profiles, from Hibler and LeSchack (1972)

2.5.3 Autocorrelation function and correlation length

The autocovariance function $C(\tau)$ for discrete detrended profiles with constant mean μ and lag τ is

$$\begin{aligned} \operatorname{cov}\left[z(x), z(x+\tau)\right] &= \big\langle \{z(x)-\mu\}\{z(x+\tau)-\mu\} \big\rangle & (2.14) \\ &= \big\langle \{z(x)\}\{z(x+\tau)\} - \mu^2 \big\rangle & (2.15) \\ &= C(\tau) & (2.16) \end{aligned}$$

The autocovariance can be made dimensionless by normalizing by $C(0)$ which is the "a priori" variance of the process: $C(0) = \langle (z(x)-\mu)^2 = \sigma^2 \rangle$ to arrive at the autocorrelation $\rho(\tau)$

$$\rho(\tau) = C(\tau)/C(0) = C(\tau)/\sigma^2 \tag{2.17}$$

The auto-correlation provides the same information as the PSD, but in slip space (units of distance) instead of spatial frequency space (units of inverse distance) because the autocorrelation function $C(\tau)$ and the power spectrum $S(f_x)$ are a Fourier transform pair

$$C(\tau) = \int_{-\infty}^{\infty} S(f_x)\, \mathrm{e}^{j2\pi f_x x}\, dx \tag{2.18}$$

The lag length l_c where the auto-correlation function has dropped to 1/e represents the lateral dimension of surface structure (Stover, 2012). Alternative definitions for correlation length exist to account for the fact that natural surfaces are not modeled by a stationary random process resulting in an exponential ACF. At some length scales natural surfaces exhibit inverse power law behavior between roughness amplitude and spatial frequency. Autocorrelation length can also defined as the integral (or sum in the discrete case) of the squared ACF, or in the same manner from the PSD, according to

$$l_c = \frac{2}{\sigma^4} \int_0^\infty C^2(\tau) d\tau = \frac{2}{\sigma^4} \int_0^\infty S_1^2(f_x) df_x \tag{2.19}$$

2.5.4 Semivariogram

Semivariograms are widely used in geostatistics, and are appealing because they relieve the constraint on wide-sense stationarity. For this purpose one assumes that if the mean is not constant everywhere, it would be for small lags $|h|$, so that the expected differences would be zero

$$\big\langle z(x) - z(x+\tau) \big\rangle = 0 \tag{2.20}$$

The second concept is to replace the ACF by the variances of differences as measures of spatial relation, which, like the ACF, depended on the lag and not on absolute position.

$$\begin{align} \text{var}\left[z(x) - z(x+\tau)\right] &= \big\langle \{z(x) - z(x+\tau)\}^2 \big\rangle \tag{2.21} \\ &= 2\gamma(\tau) \tag{2.22} \end{align}$$

The quantity $\gamma(\tau)$ is known as the semivariance at lag τ. For wide-sense stationary processes the variogram and the covariance are equivalent, and from their definitions in equations 2.16 and 2.22: $\gamma(\tau) = C(0) - C(\tau)$. The semivariance can be estimated wider range of circumstances, which has made it much mor useful than the covariance (Webster and Oliver, 2007).
Semivariograms can be modeled by a negative exponential model (Fig. 2.5).

$$\gamma(\tau) = b + C_0 \cdot \left(1 - e^{-\frac{\tau}{a}}\right) \tag{2.23}$$

where b, the nugget, is set to zero, and a is the range parameter. The sill is C_0. In most of these models the variance has a maximum, which is the a priori variance of the process, known in geostatistics as the sill variance. The exponential variogram approaches the sill asymptotically. For practical purposes the distance at which γ equals 95% of the sill variance is the effective range. Above this range the variable is said to be uncorrelated (Webster and Oliver, 2007).

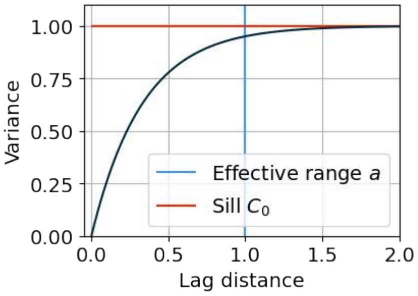

FIG. 2.5: Exponential semivariogram model with nugget $b = 0$, sill $C_0 = 1$ and range $a = 0.333$.

2.5.5 Fractal dimension

In the context of 1D profiles, a fractal is a mathematical description of the scaling properties of an irregular geometry. A parameter to describe non-stationary ice surfaces is the fractal dimension.

PSDs in the form of $S_1(k) = C \cdot k^{-\alpha}$, where $k = 2\pi/\lambda$ is the wavenumber along the profile, are modeled by self-affine fractals. The scaling is described by the fractal dimension D. It can be shown that D is the slope of the PSD on a log-log plot by

$$D = 2.5 - \alpha/2 \tag{2.24}$$

(Brown, 1987). D is between the topological dimension (1 for a profile, 2 for an area) and the Euclidean dimension (2 for a profile, 3 for an area). Higher values of D indicate rougher surfaces. Natural surfaces often display fractal properties only over a specific length scale or exhibit distinct scaling regimes at different length scales. On scales larger than a certain cut-off, the surface may still be characterized as a realization of a stationary random process (Von Saldern et al., 2006).

The fractal dimension's usefulness is that within the known fractal dimension, one can simulate the rough surface according to certain functions of fractal characteristics and calculate other related parameters. For sea ice surfaces Von Saldern et al. (2006) report fractal dimensions of 1.3–1.9 from altimeter data. For sea ice draft Gneiting et al. (2012) determined fractal dimensions of 1.2–1.5 from upward looking sonar.

2.6 Microwave remote sensing of sea ice

The scattering of microwaves by sea ice and the overlying snow cover is sensitive to minor variations in its geophysical properties and can be obtained from remote sensing by synthetic aperture radar (SAR). Sentinel-1 (S1) is an ongoing SAR mission providing nearly complete coverage of the Arctic sea ice every six days (Torres et al., 2012). The two spacecraft operate at a center frequency of 5.405 GHz at C-band. C-band is located at frequencies of 4–8 GHz, with corresponding wavelengths of 7.5–3.75 cm. The two satellites, S1A and S1B, share the same near-polar orbital plane with a 180° orbital phase difference.

The quantity of interest is the backscattering coefficient σ^0 of sea ice. σ^0 can be imagined as the strength of reflection by a conducting sphere. The backscattering coefficient is related to the radar equation for the measured power P_r of an echo received at a microwave antenna according to

$$P_r = P_t \frac{G^2 \lambda^2 \sigma}{(4\pi)^3 R^4} \iff \sigma = P_r \frac{(4\pi)^3 R^4}{P_t G^2 \lambda^2} \tag{2.25}$$

$$\sigma^0 = \frac{\sigma}{A} \tag{2.26}$$

where P_t is the transmitted power, G is the antenna gain, λ is the transmitted wavelength, and R is the range of the target from the radar antenna. Those parameters are known through instrument calibration. The only property dependent on the target properties is the target's radar cross-section σ. σ^0 is the area-normalized radar cross-section (or backscattering coefficient) normally expressed in decibels. σ^0 varies significantly with incidence angle, wavelength, polarization, and with changing properties of the scattering surface (Ulaby and Long, 2015).

In general, backscatter from a medium is a function of its geometric and dielectric properties. Dielectric behavior is quantified by the relative dielectric permittivity $\epsilon_r = \epsilon' + j\epsilon''$, where the loss factor is the complex part. At a given frequency, the loss factor determines the decrease of signal power density p with depth z according to

$$p(z) = p(z = 0) \cdot \exp^{\frac{2\pi}{\lambda} \frac{\epsilon'}{\sqrt{\epsilon''}} z} \tag{2.27}$$

The penetration depth δ is conventionally the depth z where p has decreased to 1/e of the incident power at the surface with

$$\delta = \frac{\lambda}{2\pi} \frac{\sqrt{\epsilon''}}{\epsilon'} \tag{2.28}$$

The penetration depth of sea ice increases with decreasing temperature and decreasing ice salinity, which determines the contribution of backscatter originating from multiple scattering in the ice interior, the so called volume scattering. For snow-covered sea ice, volume scattering from the bulk, and surface scattering at the snow-ice interface both contribute to the returned signal.

Sentinel-1 can receive and transmit waves in horizontal (H) and vertical (V) polarization. Surface scattering will cause phase shifts of 180° or 0° (0° for odd bounce scattering, 180° for double bouncing at two right-angled surfaces) and therefore not depolarize the wave. Surface scattering largely depends on orientation and roughness of the surface (Ulaby and Long, 2015). Volume scattering (many scattering events) phase shifts can take any value between 0° and 180°, but usually vary around 45°, causing a depolarization of the incident wave, recorded in the HV signal (Shokr and Sinha, 2015).

2.6.1 Backscatter and sea ice evolution

FYI has a high loss factor due to high salinity, and respectively low penetration depths, which prevents most volume scattering. The penetration depths for FYI in C-band are in the order of 5–20 cm. Thus, the energy reflected to the radar is low, except for sharply angular pressure ridges. The loss factor of dry snow is so low that the snow has little effect on sea-ice radar measurements made in winter.

Typical penetration depths for MYI are in the decimeter range, due to lower salinity. Pockets that were occupied by brine in the FYI are now small air bubbles that contribute significantly to volume scattering. The supposedly rougher, melt pond-shaped surface additionally enhances scattering. However, MYI pressure ridges tend to be more rounded, have fewer large voids, and are not as steep-sloped. Their scattering cross sections are not as distinct from the surrounding MYI as for FYI ridges (Ulaby and Long, 2015).

2.6.2 Backscatter and roughness

Sophisticated surface scattering models allowed to address the dependence of the backscattering coefficient σ^0 on surface roughness. In practice, one characterizes the surfaces by only their centimeter-scale roughness statistics, because larger scale roughness does not contribute to incoherent scattering and can be treated as a mean surface (Ulaby and Long, 2015).
The shape of the surface height correlation function, RMS height, and correlation length all influence the backscatter depending on incidence angles. To illustrate the influence of surface roughness, the simulated backscatter of surfaces with exponential correlation functions and RMS height values of 1.5 cm and 0.5 cm is shown in Fig. 2.6, right panel. The surface with larger RMS height has a larger backscatter than the surface with lower RMS height. For HH polarization, the incidence angle dependence for the rougher surface is weaker, while HV incidence angle dependence does not change with variations in RMS height. For otherwise constant parameters, a Gaussian ACF causes a steeper incidence angle dependence for both polarizations than an exponential correlation function, as illustrated in Fig. 2.6, left panel.

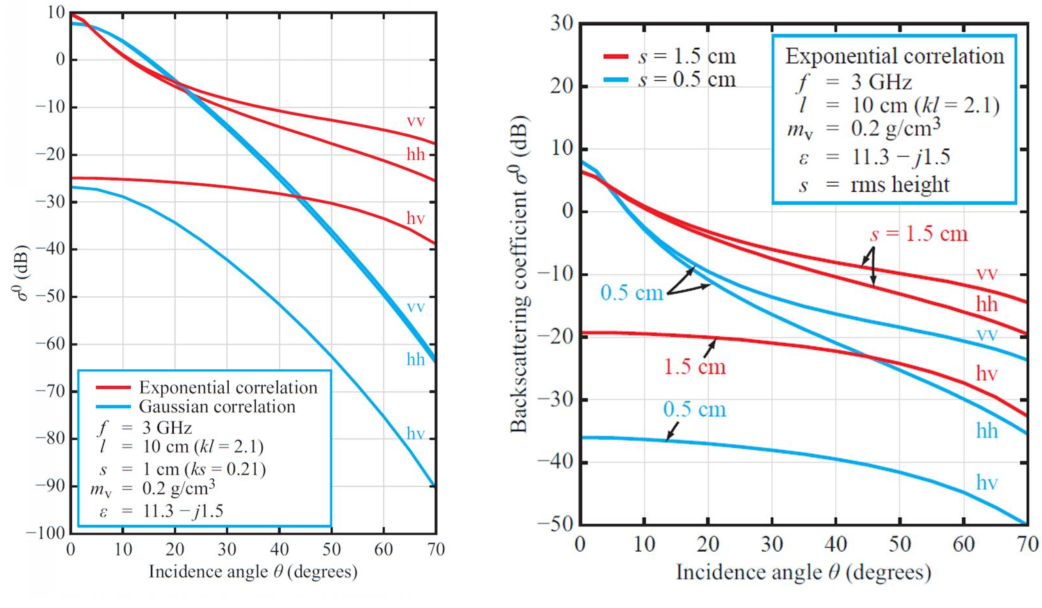

(A) (B)

Fig. 2.6: Backscatter response to two surfaces with (A) different correlation functions and (B) different RMS heights at 3 GHz, modeled with I2EM. (Ulaby and Long, 2015)

Segal et al. (2020) provide an analysis of the correlation between roughness and HH backcatter. RMS height from gridded ALS points with a resolution of 1 m x 1 m (swath width 400 m, vertical accuracy 10 cm or better) is used as a roughness estimate for FYI and MYI in the CAA. The HH backscatter has a significant positive linear correlation with RMS roughness for FYI ($R^2 = 0.58$), but not for MYI.

2.6.3 Incidence angle dependence of backscatter

It is known that the incidence angle of a radar signal onto a surface influences the intensity of the backscatter signal (Carsey, 1992). In SAR images like Sentinel-1 extra wide-swath (EW) images, this effect is visible as a trend of image brightness in range direction, with generally higher backscatter values for small incidence angles and lower backscatter values for large incidence angles θ. Different surface types show varying rates of decrease in backscatter with θ. For SAR geometry refer to Fig. 2.7.

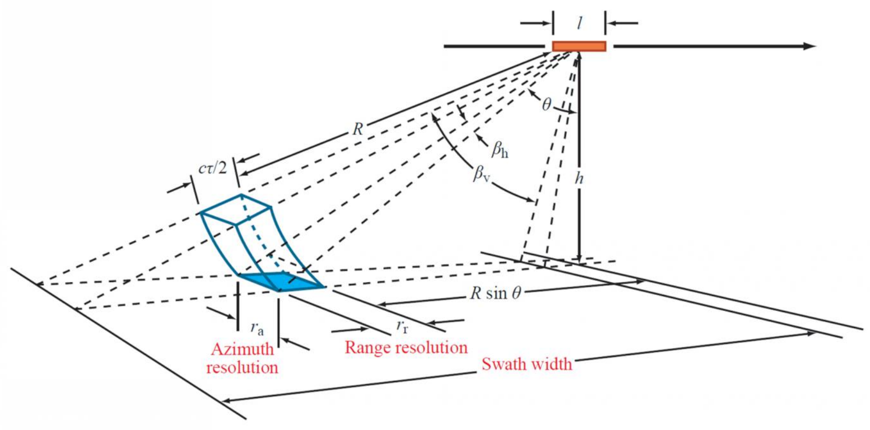

Fig. 2.7: SAR geometry, with antenna length l, incidence angle θ, slant range R, pulse length τ, speed of light c, horizontal beamwidth β_h, vertical beamwidth β_v. Adapted from Ulaby and Long (2015).

Aldenhoff et al. (2020) studied the incidence angle dependence of smooth and deformed FYI, and MYI (divided into predominantly second year ice and ice older than 3 years). Manual classification of the ice in pairwise Sentinel-1 EW images (different time, same location) resulted in 240 FYI samples and 320 MYI samples. Linear regression was done on the sample-wise HH and HV backscatter change vs incidence angle change. The R^2 values for all cases, as well as the analysis of the residuals of the model, indicate that a linear model is a valid choice, confirming previous work, showing that a linear approximation is a good approximation for the relationship for angles between 20–50°. The highest incidence angle dependence was found for smooth FYI with -0.24 and -0.16 dB/1° for HH and HV polarization, respectively. Deformed FYI shows slightly lower slopes (-0.20 and -0.11 dB/1°, for HH and HV). The old MYI has the lowest slopes (-0.10 and -0.04 dB/1°, for HH and HV), followed by MYI (-0.15 and -0.07 dB/1°, for HH and HV). The slopes are constant over time and are deemed representative for winter conditions in the Beaufort Sea.

For FYI, surface scattering is the dominant mechanism, which is more affected by incidence angle changes than volume and multiple scattering, which gets more important the older the ice becomes. Furthermore, the cross-polarization backscatter signal originates from multiple scattering events (volume scattering) and therefore shows a lower dependence on incidence angle compared to the co-polarization channel (Aldenhoff et al., 2020). They note that is likely that the incidence angle distribution for smooth FYI follows the noise floor (-28 dB) rather than the real incidence angle dependence at cross-polarization, because backscatter intensities for this ice type are at or below that noise floor.

The dependence of RADARSAT-2 σ^0_{HH} and σ^0_{HV} of snow covered on smooth FYI at the end of winter on incidence angles between 26–37° is studied by Gill et al. (2015). Thin (7.7 cm), medium (20.5 cm) and thick (36.4 cm) snow covers exhibits similar slopes for HH and higher slopes for HV compared to those reported by Aldenhoff et al. (2020): The slopes for HH and HV polarisation are -0.27 and -0.24 dB/1° for thin snow, -0.25 and -0.25 dB/1° for medium snow, and -0.33 and -0.25 dB/1° for thick snow, respectively. They observed an increase in σ^0_{HH} and σ^0_{HV} with an increase in snow thickness, which they attributed to the elevated brine volume in the basal layer, forming larger brine coated snowgrains, presenting an additional volume scattering component to the total scattering.

3 Materials and Methods

Airborne ice thickness surveys over Nansen Sound ice plug were carried out on 30 March 2017, 6 May 2018, and 2 April 2019. In 2017 and 2019, an additional laser scanner (ALS) was installed in the aircraft, which provides two-dimensional roughness information. Snow depth from snow radar is available for 2017 and 2019. The first section of this chapter is dedicated to the airborne survey data acquisition and processing.

This dataset is complemented by MODIS true color images and Sentinel-2 true color images to assess the formation, evolution, and breakup of the ice on Nansen Sound. Annual minimum ice plug extent, approximate start and end of surface melt, and classification of the surface at maximum melt pond coverage are extracted to help interpret ice thickness and roughness evolution.

Sentinel-1 radar backscatter scenes around the dates of the flights for various incidence angles are used to address evolution of backscatter and incidence angle dependence.

Radiation balance, mean summer and winter temperatures, cumulative melting and freezing degree days, total precipitation, and wind speeds are extracted from ERA5 Land climate reanalysis for the years 2016–2019.

3.1 EM ice thickness

Ice thickness measurements were carried out by EM induction sounding with a sensor system, the EM Bird, towed under a Basler BT-67 at a height of 10–20 m above the surface. The distance between instrument and surface was measured with a single-beam laser altimeter.

3.1.1 EM measurement principle

The primary components for induction sounding are the transmitter and receiver coils. A primary field H_z^P is generated at the transmitter coil with a frequency of 4060 Hz. Ice has a very low conductivity of 0–50 mS/m and is penetrated without creating any significant secondary field. In contrast, seawater has high conductivity of 2400–2700 mS/m, leading to eddy currents, and consequently to a secondary magnetic field H_z^S, whose amplitude and phase is measured with the receiving coil (Haas et al., 2009).

The normalized secondary magnetic field is $Z = H_z^S/H_z^P$. Z is complex and is usually described as in-phase component I and quadrature component Q.

For sea ice thickness mapping, the EM Bird altitude h_{EM} over the conductive sea surface is the parameter of interest. The presence of sea ice increases h_{EM}

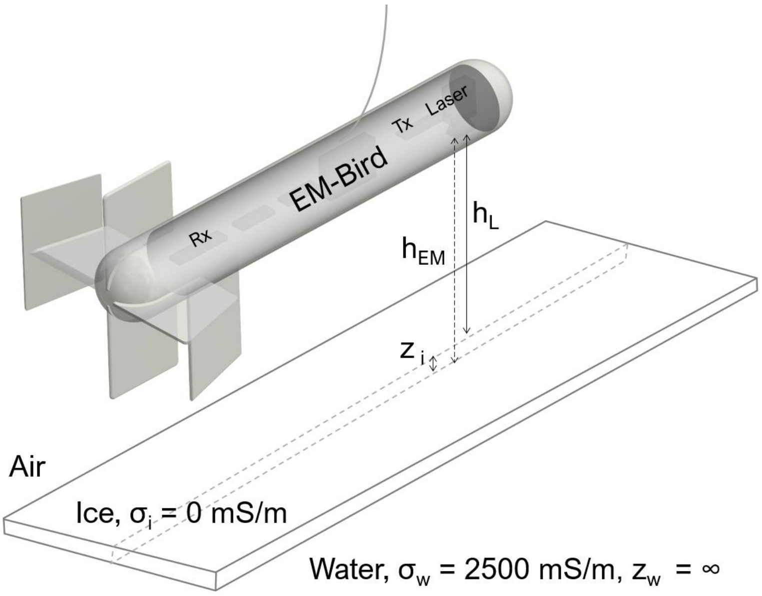

FIG. 3.1: Sketch of the EM Bird with transmitter coil (Tx) and receiver coil (Rx), not shown are bucking coil, calibration coil, computer, Differential Global Positioning System (DGPS), and wireless network antenna. Distance h_{EM} as inferred from the EM fields and h_L distance between snow/ice surface measured by laser altimeter. Figure is not drawn to scale.

for a known bird height h_L above the surface by the ice plus snow thickness z_i

$$z_i = h_{EM} - h_L \tag{3.1}$$

h_L is measured by the single-beam altimeter. Further assumptions are negligible ice conductivity, known seawater conductivity, and horizontal layering (Haas et al., 2009). A negative exponential function of the distance h_{EM} between bird and sea surface models the normalized secondary magnetic field $Z(h_{EM})$

$$Z(h_{EM}) = B_0 + B_1 \cdot \exp(-C \cdot h_{EM}) \tag{3.2}$$

This is a first approximation to the layered half-space response and is justified in the vast majority of common situations in sea ice thickness mapping (Pfaffling et al., 2007). The coefficients B_0, B_1 and C are found by fitting the measured curve to the synthetic half-space model curve for open water with a conductivity of 2500 mS/m within a height range given by the variations of bird altitude (10–25 m). The resulting ice plus snow thickness (hereafter ice thickness) is given by Equ. 3.1.

Following Haas et al. (2009), only the Inphase component is inverted, because the Quadrature signal is weaker, more affected by noise and has a larger drift. Gain and Phase are also adjusted according to Haas et al. (2009).

When flown at 10–20 m above the surface, the EM Bird has a footprint of 45–60 m. Therefore, ice thicknesses are representative of the mean thickness in this area. Signal processing at 10 Hz and a speed of 50 m/s results in an average point spacing of about 5 m.

If existent, open leads with an ice thickness of 0 m are used to calibrate the ice thickness retrievals, providing an accuracy of EM measurements of ±0.1 m over level ice. However, over the fast ice in the CAA, leads of sufficient width in winter are seldom and none were present in vicinity of the ice plug in the three surveys. Therefore, thickness retrievals can be more sensitive to uncertainties in drift and calibration, amounting to an accuracy of ±0.15 m over level ice (Haas and Howell, 2015). The uncertainties of level ice thickness retrievals most strongly affect the accuracy of the modal thickness. Over ridges, ice thickness can be underestimated by 50% or more due to conducting channels in ridge keels. Consequently, uncertainties over ridges affect the magnitude and length of the tails of ice thickness distributions and by that the mean ice thickness (Haas and Howell, 2015).

3.2 Processing of altimeter data

The employed Riegl LD 90 altimeter has a measurement rate of 10 Hz and a wavelength of 905 nm. The recorded altimeter ranges represent the distance between surface and instrument and therefore depend on flight altitude. Information about the absolute height of the EM Bird with respect to a fixed reference system e.g., from Differential GPS (DGPS), is missing for most flights. The altimeter profiles show a high-frequency signal, superimposed on the mostly low-frequency aircraft altitude variations. Filtering is necessary to obtain surface roughness information. The goal is to describe all roughness on scale smaller than a certain cut-off wavelength as a deviation from a "local level surface height".

Hibler III (1972) describes a three-step method for filtering the altitude variations caused by the aircraft motion: First, a high pass filter is applied to the profile, which comes with the problem of depressing ridges. This arises from the non-Gaussian properties of the ice-air interface. The surface height statistics rather follow a Log-Normal distribution. Second, a set of minimum points, each next minimum 12.7–139.7 m ahead of the previous minimum is recorded. The data point spacing is 1.27 m. In the third step, a low pass filter is applied. The transition band of wavelengths for this step must be specified accurately and depends on the aircraft, which makes automatizing impossible (Hibler III, 1972). The shortcomings of this process are motivation to search for an alternative, more flexible approach.

Here, the x-axis is the cumulative distance between the geographical locations of the data points, spaced about 50–70 cm. The y-axis is the recorded single-beam laser altimeter height. Two modifications of the method by Hibler III (1972) are developed and tested.

3.2.1 Iterative fit

I have implemented a method where I fit a spline to the raw range profile and subsequently weigh all points that fall above the spline[1] higher than those that fall below, as illustrated in see the first panel in Fig. 3.2. Since the measured ranges are the distance between EM Bird and surface, the largest ranges are representative of the local level surface. A new spline is fitted to the weighted data points. This process is repeated until the change between subsequent iterations gets small.

The outlined procedure would result in a good approximation for the concave part of the curve, but not for the convex part; see the first panel in Fig. 3.2 for an example. Two things can help navigate this problem: Placing knots more densely in the convex part, but that would imply a change of wavelengths that get filtered between convex and concave sections. A second approach, which was tested here, is weighting data in convex sections of the spline higher than data in concave sections. The filtering uses the following steps:

1. An initial spline $B_0(x)$ is fitted to h_L (Spline 1 in Fig. 3.2, panel B). The spacing of knots is chosen to be 100 m, which corresponds to every 200th data point.

2. The second derivative of spline $B_0(x)$ is evaluated for concavity and convexity, this is passed onto the weights w by weighing points above the spline with $w = 1$ and points below with $w_{below,\,convex} = 5\, w_{below,\,concave} = 5 \cdot 0.01 = 0.05$.

3. With those weights, a new spline $B_i(x)$ is fitted. This process is repeated N times, until subsequent splines have a mean deviation of y values of less than 1 mm, which was achieved after 5 iterations (see Spline N in Fig. 3.2, panel B). The resulting surface heights above local level surface height are $h_N = B_N(x) - h_L$ (Fig. 3.2, panel C).

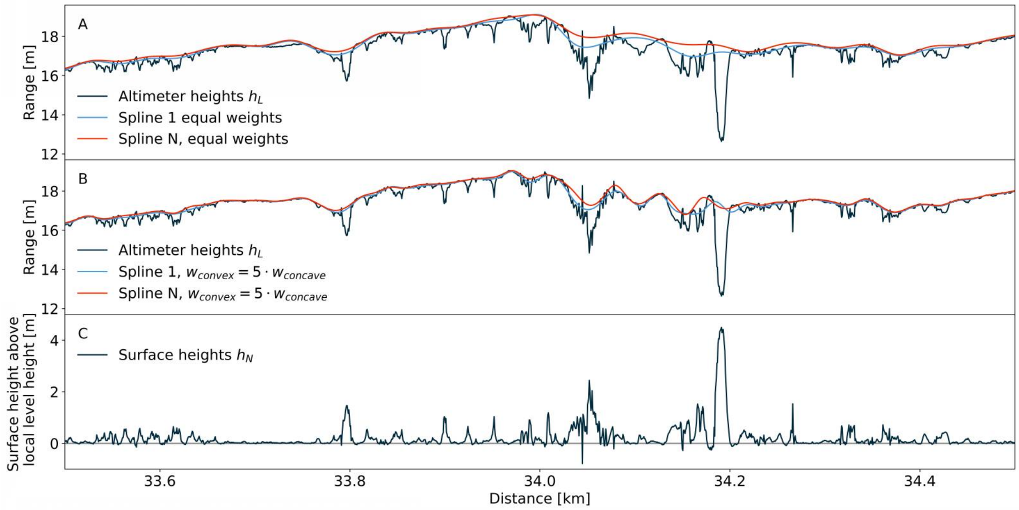

Fig. 3.2: Iterative fitting procedure. (A) Fit with equal weights for all data points. (B) Fit with higher weights in convex sections. (C) Resulting surface heights h_N.

---

[1] The Python package "rpy2" provides the interface "robjects" to facilitate the use of R by Python programmers. We use the function "smooth.spline" to fit a cubic spline to the given data. When specifying only the number of knots (results in equally spaced knots) or the x positions of the knots to be used, the smoothing parameter of the ridge regression is determined by leave-one-out cross-validation.

3.2.2 Modified version of Hibler's method

The second approach implements Hibler's process with a modification in the third step (Fig. 3.3):

1. Again, an initial spline $B_0(x)$ with knots spaced by about 100 m is fitted to h_L.

2. Subtract the spline $B_0(x)$ from h_L and find the local maxima in intervals defined by the roots of the second derivative of $B_0(x)$ so that one maximum is recorded after each change in curvature. All these local maxima get connected linearly.

3. The linear interpolation is smoothed, by evaluating it at all x values and choosing 100 m as knot spacing again, the smoothed curve is $B_{max}(x)$. The resulting surface heights are $h_H = B_0(x) + B_{max}(x) - h_L$

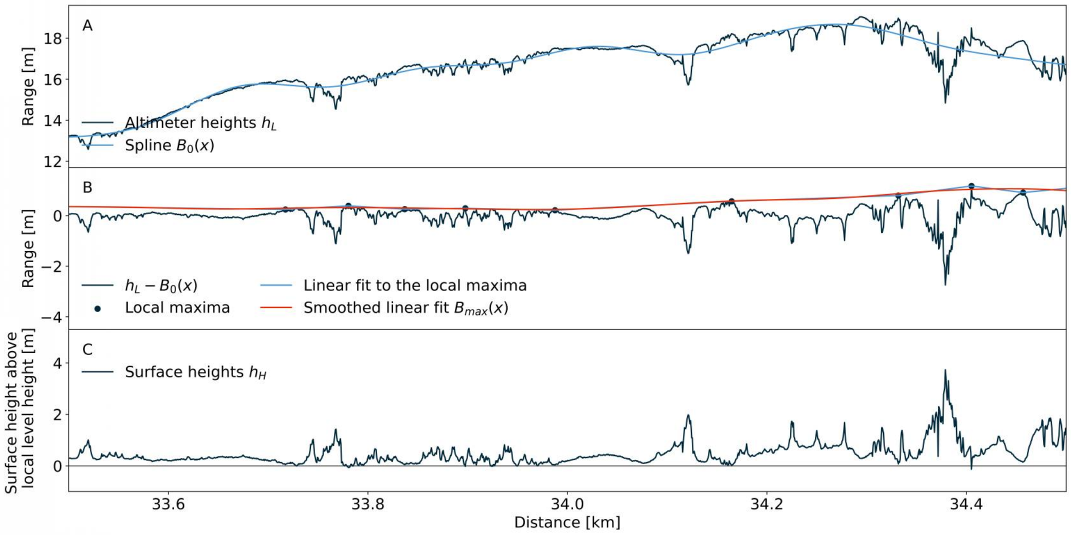

FIG. 3.3: Modified version of Hibler's method. (A) Step 1: Initial spline. (B) Step 2 and 3: Fit to local maxima. (C) Resulting surface heights h_H.

3.2.3 Validation of filtering methods

Available IceBird DGPS data

For 2018, the fit results can be evaluated against the DGPS heights of the EM Bird, which represent the height with respect to the reference ellipsoid. Fig. 3.4 A, shows the DGPS height profile h_{DGPS} alongside the laser altimeter ranges h_L. The mean DGPS height is expected to show a near constant offset from the mean altimeter ranges, corresponding to the local offset between mean reference ellipsoid WGS84 and mean the surface height. "NGA EGM96 Geoid Calculator" gives an offset between 9.94–11.33 m (National Geospatial Intelligence Agency, 2021). The value determined for the offset is $h_{offset} = \overline{h_{\mathrm{DGPS}}} - \overline{h_L} = 10.36$ m. After correcting the altimeter ranges by subtracting

the DGPS heights and the offset (Fig. 3.4 B) a trend in the signal can be seen, which is accounted for by further subtracting a polynomial of third degree $C(x)$. Fig. 3.4, panel C shows the obtained heights $h_{\text{corrected by DGPS}} = h_{\text{DGPS}} - h_L - h_{offset} - C(x)$, where large oscillations are still present. They could be explained by a combination of GPS errors, and pitch and roll of the Bird.
Those large-scale height oscillations are not present in the filtered profiles in Fig. 3.4, panela D and E, respectively. Enlarged views of the results from $h_{\text{corrected by DGPS}}$ compared to h_N and h_H are given in Fig. 3.5.
A simple correction of altimeter heights by the DGPS signal is not useful, however the DGPS signal contains information on the wavelength range where aircraft altitude variations dominate the altimeter signal. This will be used in the following to evaluate the filtering methods.

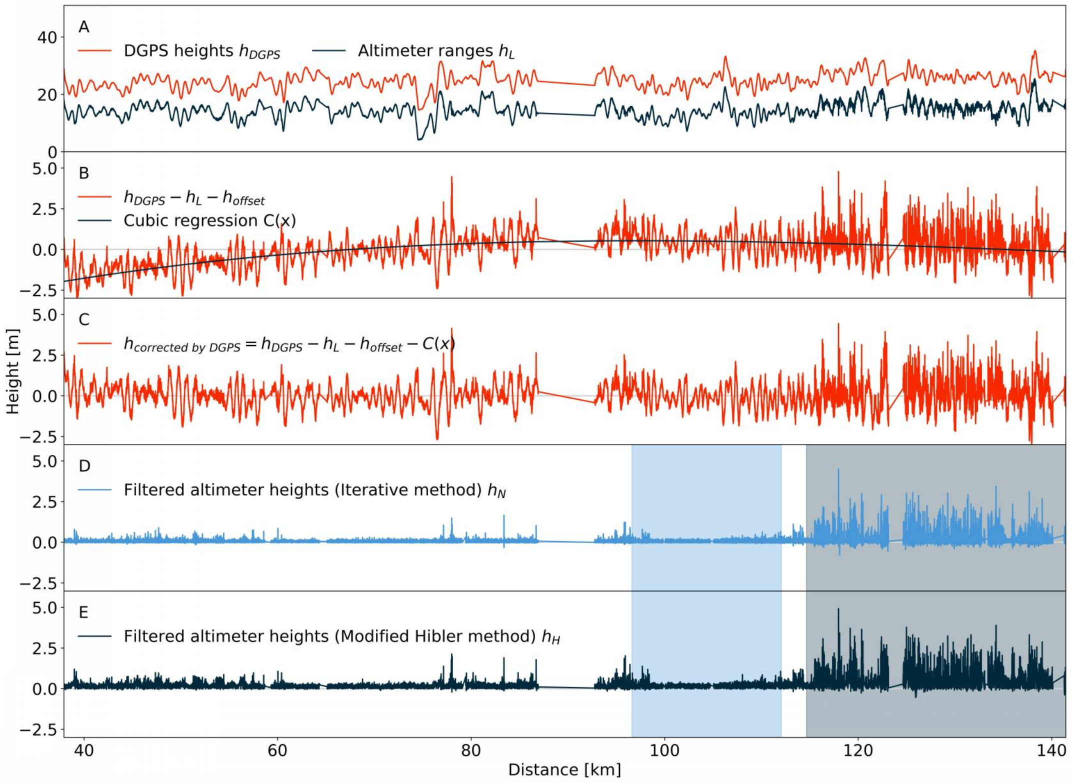

Fig. 3.4: Overview of the surface height profiles for 2018. (A) Offset between DGPS heights H_{DGPS} and altimeter ranges h_L. (B) Correction of DGPS profile with a spline $C(x)$. (C) Result of the subtraction of the DGPS heights from the altimeter profiles. (D) Profile of filtered altimeter heights h_N from iterative fit. (E) Profile of filtered altimeter heights h_H from the modified Hibler method.

From the histogram of obtained surface profiles from both fitting procedures, and the correction by the DGPS signal in Fig. 3.6 it becomes apparent how fitting will influence the modal thickness, and essential for roughness, the tail of the height distributions. The quality of both fit results depends on the knot spacing for the initial splines, which was a guess, but will be justified with the signal coherence in the following section.

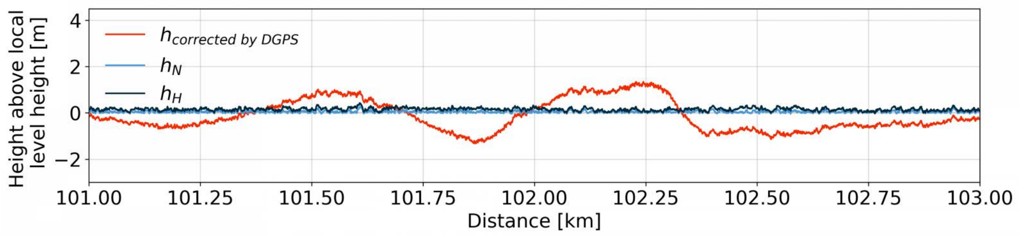

(A) Surface height profiles for a section with small height variations. The large scale low-frequency variations in $h_{\text{corrected by dGPS}}$ are visible and indicate insufficient correction, due to pitch and roll.

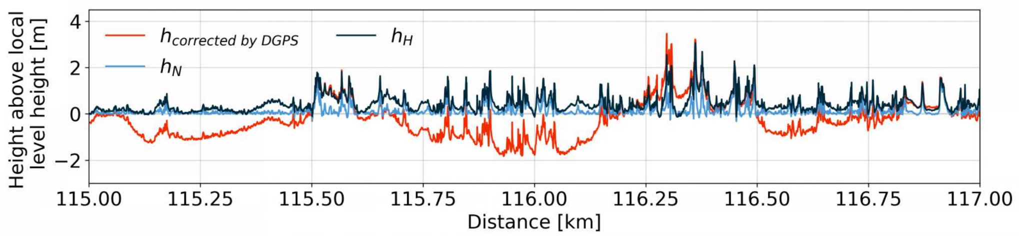

(B) Surface height profiles for a section with large height variations. Note that the variability height at 115.75–116.0 km is underestimated by both fits and the variability at around 116.4 km might be overestimated by h_N.

FIG. 3.5: Subsections of the obtained surface height profiles. Altimeter ranges after subtracting the DGPS heights $h_{\text{corrected by dGPS}}$ (red), height profiles from the iterative method h_N (blue) and from the modified Hibler method h_H (black).

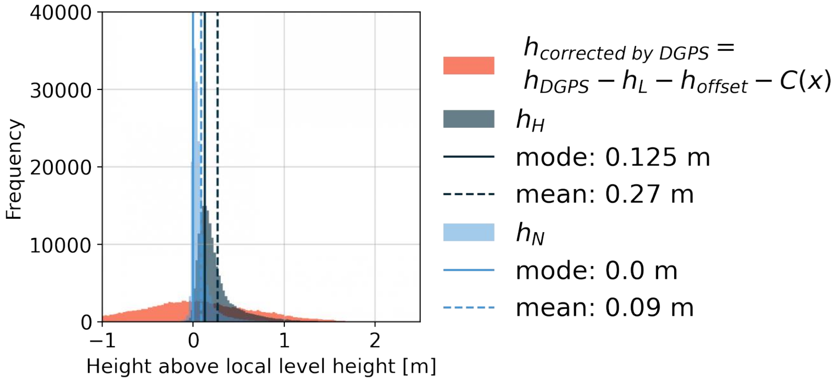

FIG. 3.6: Histogram of retrieved surface heights for the entire flight in 2018. $h_{\text{corrected by DGPS}}$ (red), h_H from the modified Hibler method (black), and h_N height from the iterative method (blue).

Signal coherence

We use Welch's method to estimate the PSD of altimeter ranges h_L and DGPS height h_{DGPS} after resampling both profiles to a continuous time axis with intervals of 0.01 s (corresponding to 100 Hz). The magnitude-squared coherence is a measure that estimates the extent to which one real- or complex-valued signal can be predicted from another real- or complex-valued signal using a linear model. It is also used as a measure of the similarities in the frequency content of two signals (Bendat and Piersol, 1986). The coherence $C_{a,b}$ of two signals a and b is given by

$$C_{a,b} = \frac{|P_{a,b}|^2}{P_{a,a} \cdot P_{b,b}} \tag{3.3}$$

where $P_{a,b}$ is the cross-spectral density of a and b.

The coherence $C_{h_{\mathrm{DGPS}},h_L}$ is around 1 for frequencies lower than 10^{-1} Hz, with a rapid decline for higher frequencies (Fig. 3.7). This transition band from 0.1–0.5 Hz corresponds to length between 500–100 m. The low coherence at short length scales can be attributed to the dominance of surface roughness, influencing h_L but not h_{DGPS}. The fitted surface elevations should be coherent with the altimeter ranges at those small length scales, i.e. the coherence of h_H with the altimeter signal h_L should ideally be $C_{h_H,h_L} = 1 - C_{h_{\mathrm{DGPS}},h_L}$.

The middle and right panels in Fig. 3.7 show the respective coherence estimates for the fitting methods described above, together with the desired coherence function. The transition from low to high coherence is between 0.2–0.5 Hz (250–100 m). The coherence function of the modified Hibler fit resembles the desired curve from the left panel reasonably well. The rougher surface is captured better than the smooth surface.

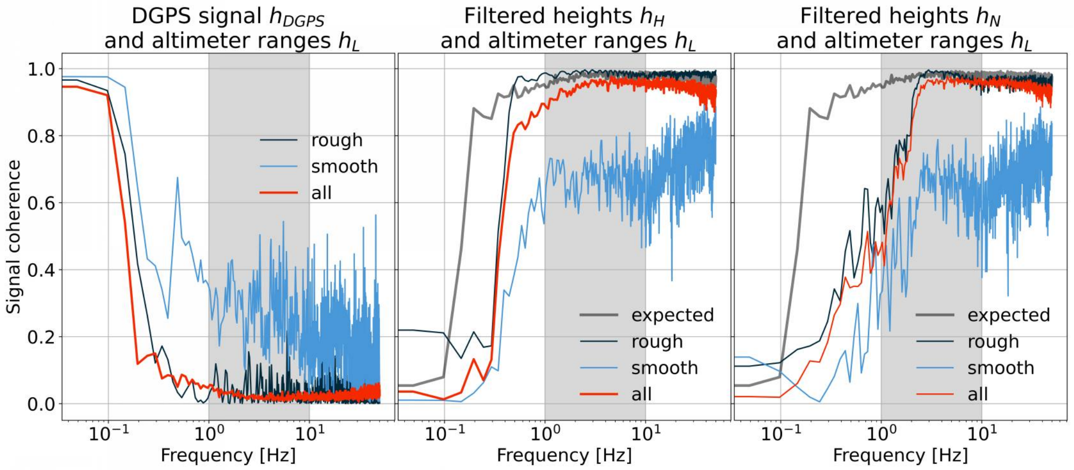

FIG. 3.7: Left: Coherence of DGPS signal h_{DGPS} and altimeter signal h_L. Center/Right: Coherence of altimeter signal h_L and surface heights h_H/ h_N. The curves for rough and smooth ice are obtained from the sections highlighted in Fig. 3.4.

Comparison with Hibler's original algorithm

Fig. 3.8 shows the same information as the right graph in Fig. 3.7, but for the fitted heights $h_{H_{original}}$ with the original Hibler method. The transition band is wider than for the modified Hibler method, where the transition is sharper.

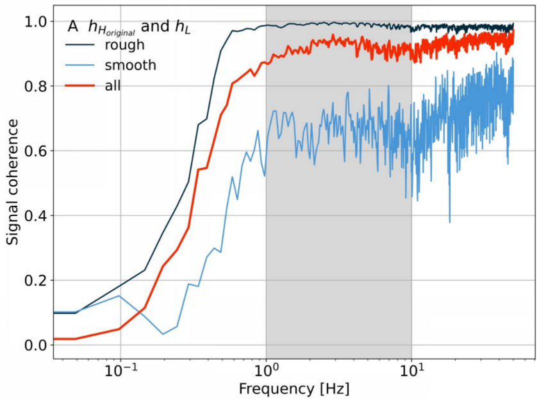

Fig. 3.8: Coherence of the DGPS signal h_{DGPS} and surface height signal $h_{H_{original}}$ after filtering with the original Hibler method.

3.3 Digital elevation models from ALS

A laser scanner was mounted on the Polar5/6 aircraft in 2017 and 2019. Its near-infrared laser is measuring surface elevation with accuracy and precision of 25 mm. It was operating with a pulse repetition frequency of 50 kHz, measuring the surface elevation in cross-track aperture angle of ±30°. The data were calibrated and georeferenced to the WGS84 datum and interpolated to a regular 0.25 m × 0.25 m grid to obtain a digital elevation model (DEM) of the sea ice surface (Ricker et al., 2014).

The heights at the coordinates of the EM measurements are extracted and will be referred to as ALS nadir heights. Fig. 3.9 illustrates the EM measurements' spacing and footprint on the gridded ALS data.

Larger jumps in elevation occur in 2017 e.g., around 92 km in Fig. 3.10, refer to Fig. A.1 in the Appendix for more details. This section is excluded for further analysis. The anomalies are attributed to gaps in the GPS height (V. Helm, personal communication, June 10, 2021). Missing GPS data also lead to incorrect referencing to ellipsoidal height, as the extracted ALS nadir heights in 2017 have an implausible mean height of -2.13 m above the ellipsoid.

For the MYI section in 2019, only data for the flight at high altitude is available, where the grid cells have a resolution of 50 cm instead of 25 cm. Additionally, this DEM has a tilt perpendicular to the flight direction, see A.2 in the Appendix. This tilt does not seem to affect the elevations within the footprint of the EM measurements notably. For reasons of data quality, we restrict the roughness analysis to the calculation of parameters within the footprint of the EM measurements, where the absolute values of the elevation, and the tilt are not impacting the results.

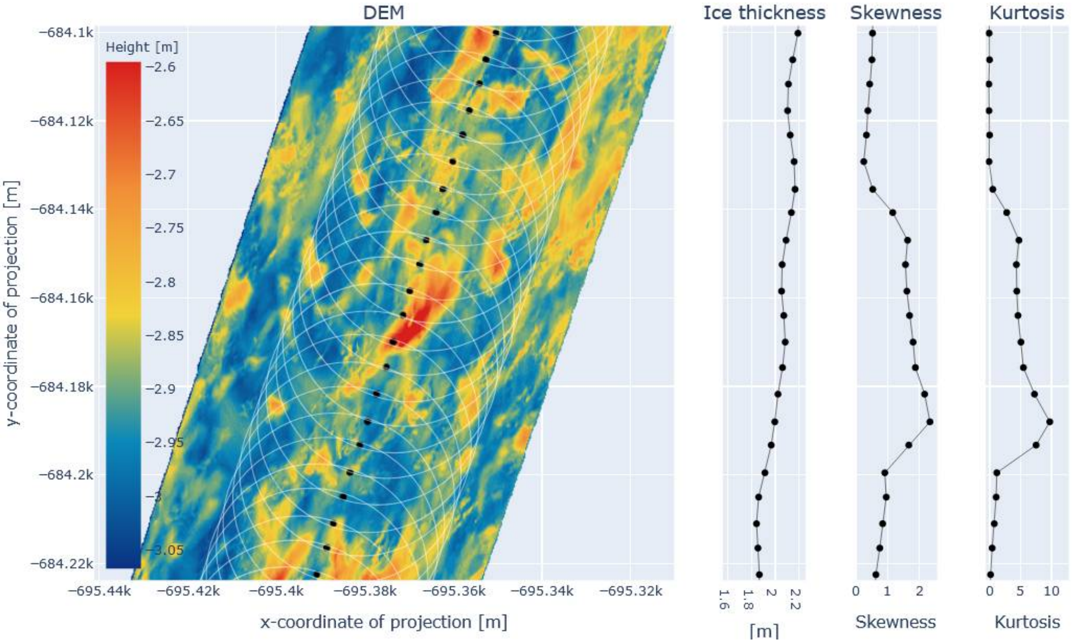

Fig. 3.9: Examples of ALS DEM with EM measurement locations (black markers), and approximate EM footprint (white circles). Skewness and kurtosis for each data point are calculated from the DEM pixels within each footprint.

The respective mean nadir elevation is subtracted from the nadir elevations for a qualitative comparison of the coincident ALS and altimeter profiles in Fig. 3.10. Several prominent peaks in surface height are visible in the fitted heights from the single-beam altimeter and the ALS nadir elevations, increasing confidence in the altimeter height filtering. In contrast, the larger-scale undulations most prominent in 2017 are removed in the single-beam profile.

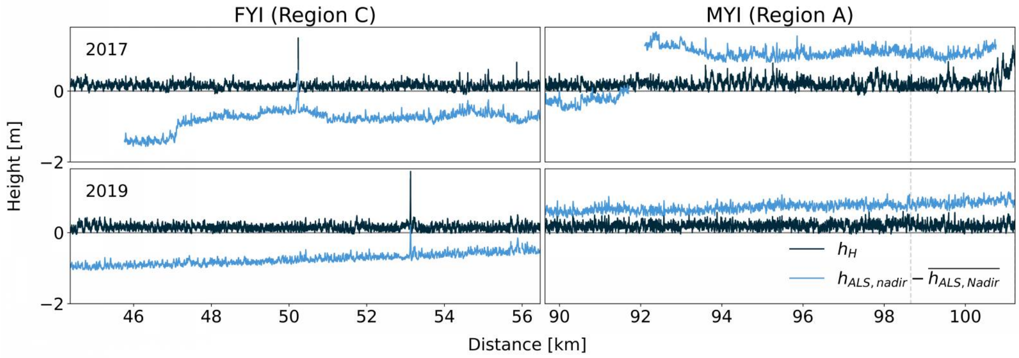

Fig. 3.10: Fitted single-beam surface heights h_H (black) and ALS nadir elevations (blue).

3.4 Snow depth from snow radar

The snow radar is an airborne, ultra-wideband 2–18 GHz, frequency modulated continuous-wave, quad-polarized microwave radar, i.e., SnowRadar version Snow5, developed at the University of Kansas, KS, USA. Snow depth is estimated according to detected air-snow and snow-ice interfaces, assuming a constant climatological snow density of 300 kg/m^3. The instrument and retrieval algorithm are not suitable for deformed ice. Altitudes larger than 100 m, high pitch and roll values, and retrieved snow depths above 1.5 m are assigned to NaN to snow depth values. The uncertainty is 4.2 cm and the mean bias is 0.64 cm. The instrument footprint at flight altitude is about 2 m in diameter (Jutila et al., 2021).

3.5 Calculation of roughness parameters

3.5.1 RMS height, RMS slope, skewness, and kurtosis

The equations for RMS height σ (Equ. 2.1), RMS slope m (Equ. 2.3), skewness and excess kurtosis (Equ. 2.6) from Chapter 2 are used with a sliding window of a length of approximately 50 m (for bottom roughness also 500 m) for the 1D profiles of surface height and ice thickness. Circles of 50 m diameter centered on the EM measurement locations for the ALS DEMs are used as windows to estimate those parameters for the ALS data, except the RMS slope.

3.5.2 PSD and fractal dimension

The power spectral densities for the altimeter profile of h_H for the different regions and years are estimated with Welch's method as described in Chapter 2 and implemented in Python package "scipy". The bandwidth limited RMS values (see Equ. 2.10) are calculated by integration from $f_{min} = 1/100$ m^{-1} to $f_{max} = 2/d$. The lower limit of 1/100 m^{-1} represents the wavelength of about 100 m above which the aircraft motion filtering becomes effective. d is the sampling distance of about 0.5 m.

The fractal dimension D is determined as the slope of the PSD on the log-log plot with the same limits of f_{min} and f_{max} as for the RMS height estimation according to Equ. 2.24. The estimated correlation lengths are calculated with the discrete version of Equ. 2.19.

In a similar manner, the PSD for ice thickness and all derived parameters are calculated, with $f_{min} = 1/1000$ m^{-1} and $f_{max} = 1/50$ m^{-1} where the upper limit is chosen to be the footprint diameter of the EM method, at higher frequencies the PSD would be a function of the smoothing from the overlapping footprints.

3.5.3 Semivariogram

Semivariograms are calculated for 1000 m sections of the profile, starting every 250 m. The maximum lag distance is set to 500 m. The resulting family of experimental variograms for surface heights and ice thickness for the different years and regions are fitted with an exponential model (Equ. 2.23). One mean semivariogram and model for each year and region is calculated, from where the mean range and sill are determined.

3.6 MODIS images

Corrected Reflectance images from the Moderate Resolution Imaging Spectroradiometer (MODIS) in GeoTIFF format is available from the Worldview website from February 2000 to present (NASA, 2021b). Band 1 (Red) has a sensor resolution of 250 m, Band 4 (Blue) and Band 3 (Green) have sensor resolutions of 500 m. Hence, Band 1 is used to sharpen the other bands. Imagery resolution is 250 m, and the temporal resolution is daily for high latitudes. The MODIS Corrected Reflectance algorithm utilizes the calibrated, geolocated radiances (MODIS Level 1B data) and is not a standard, science quality product. The algorithm is designed to provide natural-looking images by removing atmospheric effects, such as Rayleigh scattering (NASA, 2021a).

Images of Nansen Sound are inspected for cloud coverage; cloud-free images from spring 2016 to autumn 2019 are downloaded. The images serve as reference for approximate annual start and end dates of the melt season, melt pond distributions, and annual minimum ice plug extent.

3.6.1 Selecting survey sections for inter-annual comparison

The selection of profile sections suitable for comparison is based on the availability and spatial proximity of EM data in the three years. Unfortunately, flight tracks were not ideally located, i.e., they are not in close proximity.

The chosen sections for comparison of the landfast MYI are Regions A and B in Fig. 3.11. Region A comprises 11.6 km of data. Region B is a 2.6 km long subset of region A. Region A can be used to compare conditions in 2017 to 2019, while only the subset B is used to include the 2018 profile in comparisons. This is done to assure similar ice types, as the survey in 2018 was off to the east, where the considerably thicker and more rugged Old MYI was present. Region C (12.2 km) was selected to compare the MYI evolution with the seasonal landfast ice on the Nansen Sound, hereafter simply called FYI.

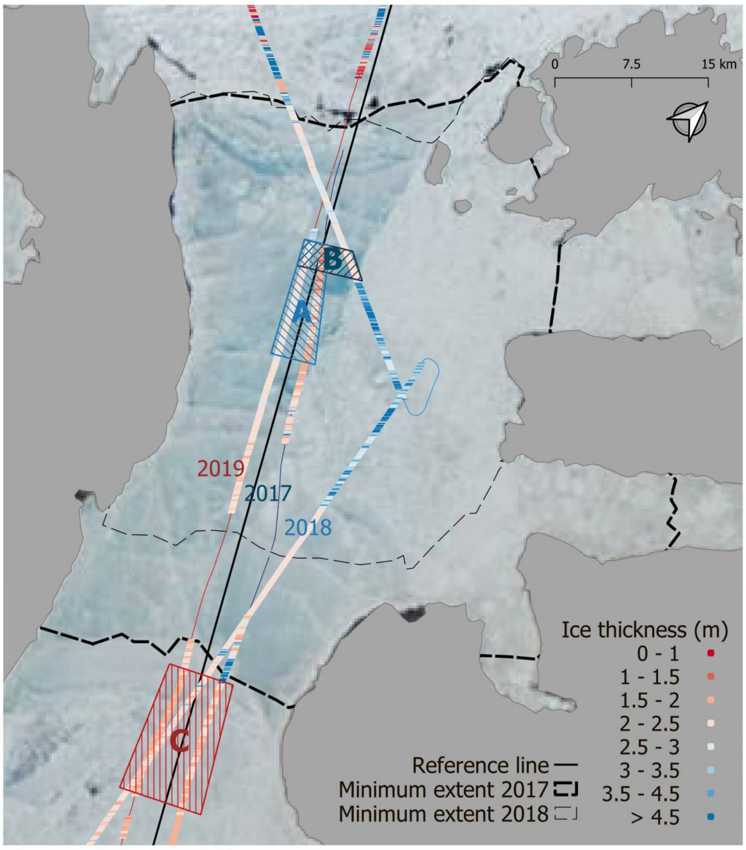

FIG. 3.11: Ice thickness for the surveys in 2017, 2018, and 2019. Regions A, B, and C are the sections which will be used for inter-annual comparison throughout this document.

3.7 Sentinel-2 images

Sentinel-2 is a multispectral satellite operated by the European Space Agency which acquires 13 spectral bands. The Level-1C products have radiometric and geometric corrections including ortho-rectification and spatial registration on a global reference system.

Level-1C scenes are downloaded and processed with the Semi-Automatic Classification Plugin (SCP) 7.8.6 in QGIS (Congedo, 2016). Cloud masks allow to filter scenes for low cloud cover (ESA, 2015b). True color images are created from Band 2 (Blue, central wavelength 0.490 μm), Band 3 (Green, central wavelength 0.560 μm), and Band 4 (Red, central wavelength 0.665 μm). All bands have a resolution of 10 m.

One image with the largest melt pond coverage and simultaneously low cloud cover is selected for summer 2017 and one for summer 2018. Those images were acquired on 17 July 2017 and 4 July 2018.

3.7.1 K-means clustering for surface classification

Clustering is the grouping of pixels based on spectral similarity for a multispectral image. The classes produced by clustering (i.e., the clusters) have no

surface type definition, consequently the user must assign a label to each class. The following K-means algorithm provided in SCP will be used:
At first, the user defines the number of clusters k expected in the image. Starting spectral signatures (seeds) are selected randomly.
Each pixel represents a d-dimensional vector $\mathbf{x}$, where d is the number of bands. An image with n pixels is a set of observations ($\mathbf{x}_1$, $\mathbf{x}_2$, ... , $\mathbf{x}_n$). For k clusters, the n observations are partitioned in sets $\mathbf{S} = \{S_1, S_2, ...S_k\}$. The average spectral signature $\boldsymbol{\mu}_i$ is calculated for each cluster of pixels S_i. The objective is to minimize the within-cluster sum of squared deviations

$$\arg\min_{\mathbf{S}} \sum_{i=1}^{k} \sum_{\mathbf{x} \in S_i} \|\mathbf{x} - \boldsymbol{\mu}_i\|^2 \tag{3.4}$$

The K-means algorithm works in two steps: The assignment step, where each observation is assigned to the cluster with the nearest mean; and the update steps where the means for each cluster are recalculated. This process is repeated until the maximum number of iterations is reached. The algorithm does not guarantee convergence to the global optimum. The result may depend on the initial clusters (Wikipedia, 2021).
The algorithm is run for the RGB bandsets of the two images with $k = 10$ clusters. The maximum number of iterations is set to 10. After the last iteration, a GeoTIFF is produced (Fig. 3.12 and 3.13). The surface types were assigned to the clusters by visual comparison with the true color representation of the bands. The resulting classes are listed below.

TABLE 3.1: Class numbers of the 10 clusters, and assigned surface type

Class No.	Surface types
0	unclassified
1	land
2	dark melt pond
3	melt pond
4	grey ice
5	white ice
6	bright white ice
7-10	land

All pixels below the EM tracks were assigned a class from 2–6. Class 2 and 3 will later be compiled as "pond" class and class 4–6 as "ice" class. The classes of the pixels coincident with the EM survey tracks are extracted from the GeoTIFFs. We call the fraction of pixels classified as "pond" melt pond fraction f_p.

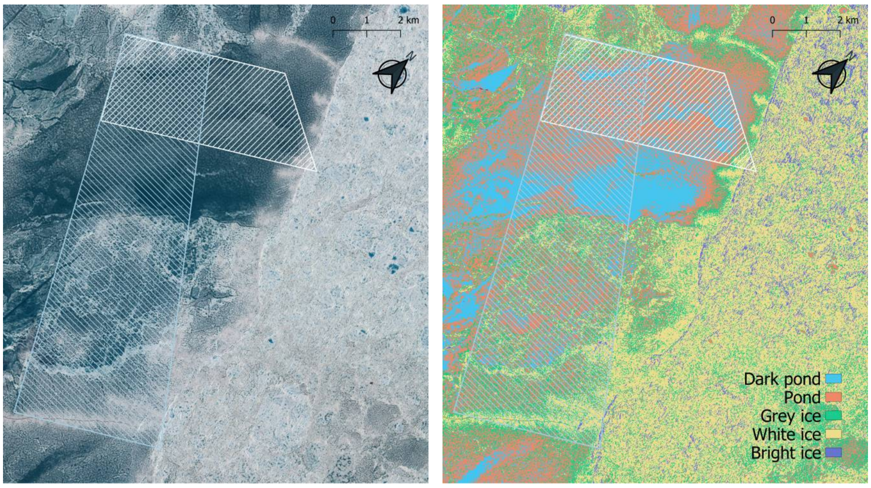

(A) RGB true color image (B) Clustering results

FIG. 3.12: Subsets of S2 scenes for the ice plug region acquired on 17 July 2017

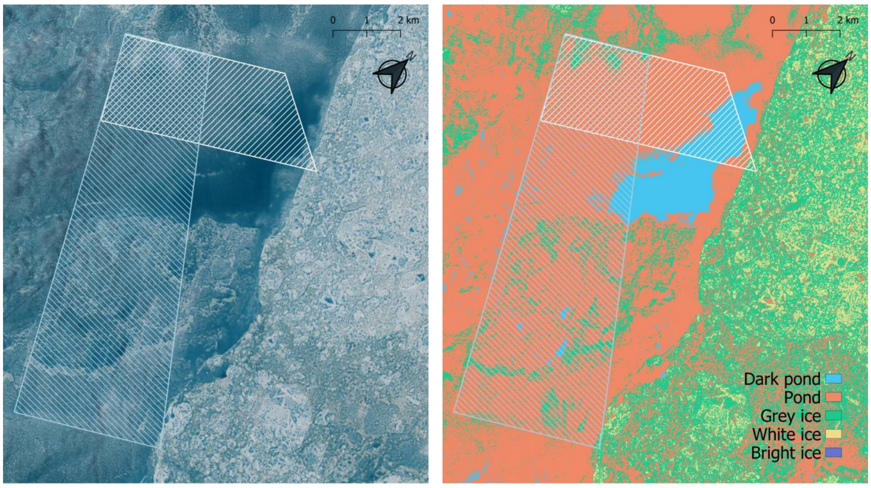

(A) RGB true color image (B) Clustering results

FIG. 3.13: Subsets of S2 scenes for the ice plug region acquired on 4 July 2018

3.8 Sentinel-1 backscatter

3.8.1 Data selection

Sentinel-1 Level 1 C-Band scenes for early spring 2017, 2018, and 2019, as well as for autumn 2016, 2017, and 2018 were obtained through Copernicus Open Access Hub (ESA, 2021). Level-1 product in Extra Wide (EW) swath mode comprises five subswaths of georeferenced and ground range detected SAR data at a swath of 400 km and 20 m by 40 m range by azimuth resolution. The product was downloaded in dual-polarization (horizontal transmit and receive polarization + horizontal transmit and vertical receive polarization, HH + HV) (ESA, 2015a).

For each spring and each autumn, five images are used to determine the incidence angle dependence of backscatter. The time periods of image acquisition for early spring are 2017-03-29 to 04-03, 2018-03-28 to 04-06, and 2019-04-01 to 04-03. For autumn, times after freezing were selected: 2017-09-01 to 09-05 and 2018-09-01 to 09-05. A list of all products used can be found in B.1 in the Appendix.

3.8.2 Processing with SNAP

The products are processed using the Sentinel Application Platform (SNAP). The processing steps in SNAP are:

- Radiometric calibration for output of σ^0. The calibration is reversing the scaling factor applied during Level 1 product generation. A constant offset, and a range dependent gain, which includes the absolute calibration constant, is applied. The information needed is included as an annotation in the Sentinel-1 product (Filipponi, 2019).
- Creation of a spatial subset
- A Geometric Ellipsoid correction, the Average Height Range-Doppler is applied. Range-Doppler correction uses the orbit state vector information to correct the geometric distortion caused by the side-looking geometry (Filipponi, 2019). Stereographic North Pole is selected as target Coordinate Reference System. An additional band with incidence angles θ is created.
- Export to GeoTIFF format for visualization in QGIS

The σ^0 and incidence angle values of the pixels coincident with the EM measurements are extracted and used in the further analysis of backscatter evolution.

3.8.3 Backscatter dependence on incidence angle

For each season, the mean incidence angle θ and the mean backscatter σ^0 over all five scenes is calculated for the FYI region and ice plug (see Tab. B.2). The mean incidence angles fall between 30–37°, so the mean backscatter is indeed comparable across seasons.

The slope σ^0/θ for each season is obtained through linear regression of the scatter plot. R^2 values for all cases indicate that a linear model is a valid choice for the incidence angle range of Sentinel-1. The obtained slopes are tabulated in Tab. B.3 in the Appendix.

3.9 ERA5 climate reanalysis data

ERA5 is made available by the European Centre for Medium-Range Weather Forecasts (ECMWF) as the latest reanalysis product. The ERA5 data set extends back to 1950, has global coverage, with a horizontal resolution of 31 km. ERA5 includes various newly reprocessed data sets and recent instruments that could not be ingested in ERA-Interim, the predecessor (Hersbach et al., 2020). ERA5 Land provides hourly analysis and forecast fields with a higher resolution of 9 km for the land component of Earth's surface.

ERA5 Land data for the surface level was downloaded through the Climate Data Store website (ECMWF, 2021) for January 2016 to December 2019 with a temporal resolution of 12 h. For the location of Nansen Sound the spatial resolution corresponds to grid cells with dimensions of 1.6 km in longitudinal direction and and 11.1 km in latitudinal direction. An overview of the downloaded variables can be found in the Appendix in Tab. B.4.

A subset of the data around the coast of the ice plug is used to obtain field means (Fig. 3.14). Grid cells with no contact to the coastline are removed to minimize the influence of mountain topography on the climate parameters. The temperature field in Fig. 3.14 illustrates the effect of cooler temperatures in the adjacent mountainous areas compared to cells with lower elevation at the coast. For each variable, the average and standard deviation over the selected grid cells is calculated. The standard deviation serves an estimator for the variability of the respective variable within the region.

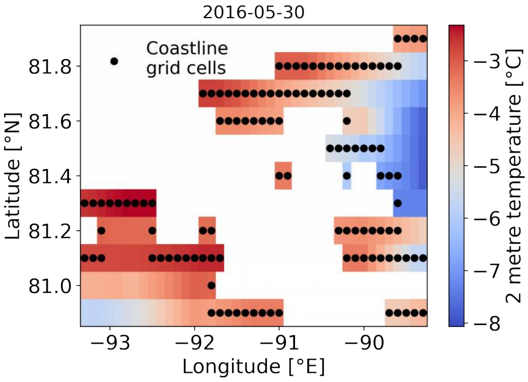

FIG. 3.14: ERA5 Land grid cell subset around the Nansen Sound ice plug. Only pixels with a coast are used to avoid cells with higher elevation above sea level.

3.9.1 Surface energy budget

The net surface energy budget is calculated as the sum of surface net solar radiation ssr, surface net thermal radiation str, surface latent heat flux slhf and surface sensible heat flux sshf. All heat fluxes at 0:00 UTC for a certain date are the accumulated fluxes of the previous 24 h. To convert from J s^{-1} m^{-2} to W m^{-2} we divide by 86400 s, which gives the net surface energy budget

$$\text{net surface energy budget} = (\text{ssr} + \text{str} + \text{sshf} + \text{slhf})/86400s \qquad (3.5)$$

Seasonal means of the total radiation for the summer seasons (June–August) and the remainder of the year (September–May) are calculated, along with total precipitation and mean temperature. The values are given in Tab. 4.6 in Chapter 4.

3.9.2 Mean temperatures and melt season onset and duration

To account for the daily temperature cycle, the 2-m temperature field was downloaded for 3 h intervals (instead of the 12 h used for all other variables) from which the daily mean temperature is obtained. Due to the freezing temperature of salt water being the important value for sea ice formation, we define the melt period as the period with daily mean temperatures above -1.80°C. The melt onset and offset dates, the melt period duration, and the mean temperatures during the respective melting seasons are computed. The same quantities are calculated analogously for the freezing season.

3.9.3 Melting and freezing degree day sums

The melting degree day sum MDD is the sum of daily average temperatures above -1.80°C over one year. Analogously, the freezing degree day sum FDD as the sum of daily average temperatures below -1.80°C over one year is used to address potential for ice growth in winter.

$$MDD = \sum_{365d} T_{\geq -1.8°C} \tag{3.6}$$

$$FDD = \sum_{365d} T_{< -1.8°C} \tag{3.7}$$

The obtained values are tabulated in Chapter 4, Tab 4.7 and Tab. 4.8.

3.9.4 Wind speed

The 10-m wind speed v in m s^{-1} is calculated from the u- and v-wind components according to

$$v = \sqrt{u_{10}^2 + v_{10}^2} \tag{3.8}$$

The wind speed is assessed for anomalously strong winds and wind directions during the breakup periods in 2016 and 2019, the values are listed in the Appendix, Tab. B.6 and B.5. In this course, striking differences in surface pressure and in precipitation are also investigated.

3.9.5 Estimation of summer ablation

The relative importance of the summer net surface radiation and the MDDs are compared by their estimated contribution to summer ablation. Assuming that the entire net radiation $\frac{Q_{net}}{A}$ is consumed by latent heat for thawing ice and snow, the total melt water mass per square meter $\frac{m_{total}}{A}$ is given by

$$\frac{Q_{net}}{A} = \frac{m_{total}}{A} \cdot L \tag{3.9}$$

where $L = 334$ kJ/kg is the standard latent heat of fusion for water. It is reasonable to assume that all snow of depth d_{snow} was melted each summer before ice ablation started. Treating snow density as constant with $\rho_{snow} = 300$ kg/m^3, and ice density also as constant with $\rho_{ice} = 900$ kg/m^3 we get the ice ablation Δd_{ice}

$$\Delta d_{ice} = \frac{\frac{m_{total}}{A} - d_{snow} \cdot \frac{\rho_{snow}}{A}}{\rho_{ice}} \tag{3.10}$$

For the snow depths in 2017 and 2019, the available mean snow depth obtained by the snow radar will be used. For 2016 and 2018 we assume a snow depth of 20 cm.

For the influence of MDDs on ablation, it is necessary to know the positive degree-day factor k. For ablation on the Greenland ice sheet these values range from $k_{ice} = 8$ mm water equivalent (w.e) per MDD to 12 mm w.e per MDD, for albedo between 0.5 and 0.3 (Braithwaite, 1995). The value for snow is $k_{snow} =$ 3 mm w.e per MDD. The ice ablation is then

$$\Delta d_{ice} = k_{ice} \cdot MDD - \frac{d_{snow}}{k_{snow}} \tag{3.11}$$

A lower and an upper bound for the ablation is calculated for the lower and upper bound of k_{ice}. The ablation estimate from the MDD model is neglecting the heat needed to warm the ice and snow to the melting point, and the heat flux from the ocean.

4 Results

4.1 Ice plug formation, evolution, and breakup

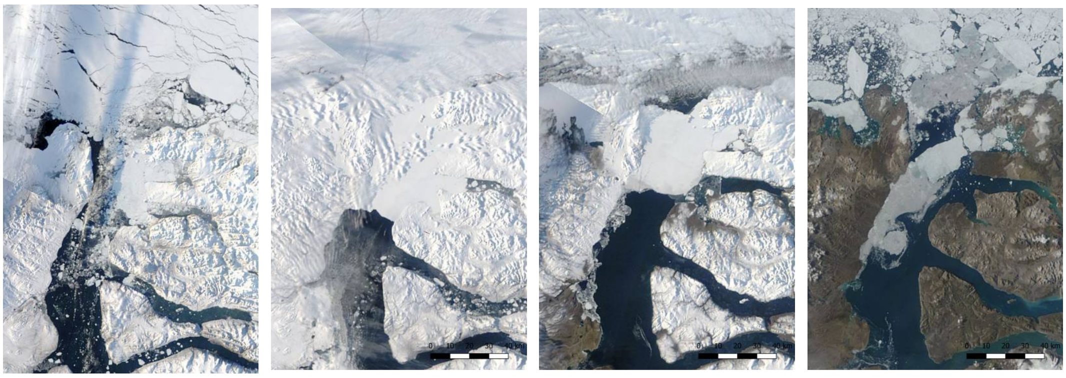

(A) 2016-09-16 (B) 2017-09-04 (C) 2018-09-11 (D) 2019-08-09

FIG. 4.1: MODIS images of the yearly minimum extents and the breakup of the plug in 2019.

For interpretation of the data collected in March 2017, the ice types after the freeze-up in 2016 must be known. The inspection of MODIS images starts in 2016 on 5 August after the ice plug broke up. In August, most of the plug ice appears to drift southward and is, at least to some degree, replaced by sea ice intruding from the Arctic Ocean. In September, the western shore is ice-free, while the ice consolidates at the eastern half of the former plug, see Fig. 4.2, first panel. This eastern section is referred to as Old MYI from now on. From 14 September onward, this ice cover appears continuous and does not change much in extent until 3 October, the last date with daylight. Ice is drifting into the fjord throughout autumn. From SAR images it could be confirmed that the Old MYI is still in place during freeze up, as well as some sparse drifting floes on Nansen Sound.

In 2017, the ice plug surface changes appearance from white to blueish between 23–26 June. The first cloud-free image from 5 July shows a variable melt pond cover, with the western second-year ice part interspersed with ponds, and fewer ponds in the eastern region of Old MYI, which is evident in the MODIS image in Fig. 4.2a. Also, the melt pond fraction seems larger on the second-year ice than on the landfast FYI. The color turns from bluish to grayish at the end of July, possibly indicating drainage of melt ponds. Fresh snow covers the plug from 17 August onward, and the surface appears more uniform and whiter. On 19 August, the southern fjord ice fractured and is subsequently drifting southward. The minimum southern extent is reached on 29 August. Open water to the north exists for short periods in July and the end of August only, most of the time dense pack ice fringes the northern edge. New ice on the sound forms in September, and at the end of the month, the ice cover appears non-uniform with leads.

In 2018, melt ponds appear on the FYI to the south, in the bays, and the western shore of the plug area around 14 June, spreading over the plug shortly before 22 June. Melting intensifies with a similar spatial pattern as that in 2017. As in the year before, the surface changes from a blue to a grey appearance, but earlier than in 2018, around the end of June. On 30 July, the southern edge fractures, and the ice gets removed during the next week. Throughout August, the edge advances northward. Open ocean conditions prevail throughout the month, and the northern edge advances to the south. The approximate minimum extent is at the beginning of September. The southern margin has lost 12 km compared to the minimum extent in the previous year, while the northern margin lost about 3 km. Between 19–24 September, a thin layer of grey ice forms to the south of the plug, which seems to thicken.

In 2019, the first hint of blue on the plug appears on 16 June and intensifies till July. In July, parts of the northern edge break off. Starting from 24 July, fractures advance northward until the barrier breaks up someday between 2–5 August. In contrast to the breakup in 2016, the sound is cleared of old ice completely during August.

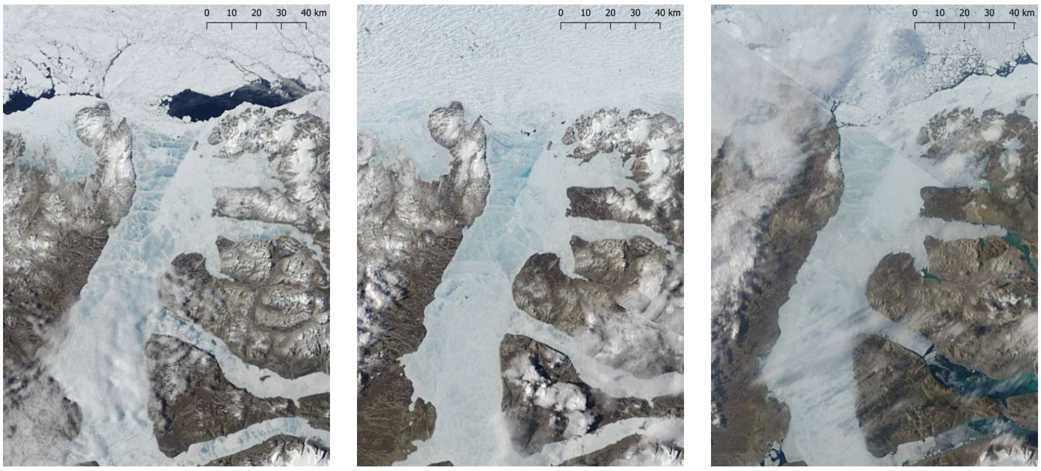

(A) 2017-07-17 (B) 2018-07-04 (C) 2019-17-07

FIG. 4.2: MODIS images at the yearly dates of apparent maximum melt pond coverage.

Tab. 4.1 gives the last date where the surface appears white, and the first date where the surface has turned blueish as the onset dates of melt pond formation.

TABLE 4.1: Earliest and latest date for appearance of melt ponds

Year	Earliest date	Latest date
2016	06-04	06-10
2017	06-23	06-28
2018	06-20	06-26
2019	06-13	06-17

4.2 Processing of altimeter data

Based on the signal coherence described in the previous chapter, I decided to use the surface height profiles obtained by filtering with the modified Hibler method. Because of the large coherence between altimeter ranges and the filtered heights, together with the low coherence between altimeter ranges and DGPS heights, it is reasonable to expect that the determined roughness parameters in 50-m sliding windows capture the magnitude of surface roughness accurately at least in 2018. For 2017 and 2019 the goodness of fit cannot be assessed.

4.3 Comparison of altimeter and ALS derived surface roughness

The RMS height, skewness, and excess kurtosis in 50-m windows is calculated for the filtered altimeter heights and from the ALS DEMs. The mean values for the regions of ice plug (A and B) and FYI (C) are listed in Tab. 4.2. The mean RMS heights for the altimeter deviate by no more than 2 cm from the ALS RMS heights. The sign and magnitude of skewness is consistent between altimeter and ALS. Skewness is positive, indicating a distribution with a slightly heavier tail of highest elevations. The average kurtosis for altimeter is below zero, indicating surface height distributions that are broader than the normal distribution, while the ALS kurtosis is positive throughout.

Histograms of the roughness parameters show distributions of RMS height and skewness for the altimeter heights that are generally broader than the distributions for the ALS DEM (see Fig. A.3 and A.4 in the appendix). The number of measurements which are used to compute the altimeter parameters in 50-m windows is smaller than the number for ALS roughness in the footprint of the EM Bird, therefore outliers will have a higher impact, explaining the broader distributions. Depending on the orientation of surface features, the roughness from the altimeter will over- or underestimate the true variability of surface heights within the EM footprint. That the profiles of the respective roughness measures for ALS and altimeter have similar magnitudes and means is illustrated in Fig. 4.6 and 4.7.

TABLE 4.2: Mean values of roughness parameters for ALS (50-m footprint) and altimeter (50-m sliding windows) for the respective profile sections and years.

Year	2017		2019		2018
	ALS	Altimeter	ALS	Altimeter	Altimeter
RMS height [cm]					
MYI (A)	8.9	9.3	8.6	7.5	9.6
MYI (B)	9.0	11.0	9.0	7.6	5.5
FYI (C)	7.5	6.5	7.2	5.8	9.4
Skewness					
MYI (A)	0.66	0.39	0.34	0.34	0.31
MYI (B)	0.67	0.31	0.35	0.40	0.15
FYI (C)	0.78	0.42	0.53	0.53	0.47
Kurtosis					
MYI (A)	0.34	-0.13	0.04	-0.25	-0.24
MYI (B)	0.43	-0.22	0.06	-0.18	-0.34
FYI (C)	0.90	0.11	0.21	-0.36	-0.04

4.4 Ice thickness and roughness evolution

4.4.1 Ice thickness evolution

The mean ice thickness of the plug is 1.7 m in 2017, 2.3 m in 2018, and 2.6 m in 2019 for region B. The mean ice thickness of the FYI (region C) in 2017, 2018, 2019 was 2.0 m, 2.3 m, and 1.9 m, respectively.

TABLE 4.3: Mean and modal ice thickness by year and section.

Region	Year	Mean [m]	Mode [m]
MYI (A)	2017	1.9	1.8
	2018	3.7	2.2
	2019	2.4	2.3
MYI (B)	2017	1.7	1.5
	2018	2.3	2.2
	2019	2.6	2.5
FYI (C)	2017	2.0	1.9
	2018	2.3	2.1
	2019	1.9	1.8

The ice thickness profile for the ice plug in Fig. 4.3 shows undulations at wavelengths of several hundred meters in 2017. The thickness in 2017 has a range of 1.7 m. Qualitatively, the aged ice in 2019 has less pronounced undulations compared to 2017, reflected in the ice thickness range that decreased to 1.3 m. The ice thickness distributions (Fig. 4.5) are symmetrical in 2017

and 2019 for MYI and FYI; the modes deviate downwards from the mean by 0.1–0.2 m for those years.
For 2019, the thickness distribution of section B has a second mode at the thickness of 2.8 m. This mode could be explained by spatial variation in summer ablation, caused by the melt pond pattern. We expect to see this difference in the mean ice thickness after the classification of surfaces in S2 summer images.
The Old MYI has the overall largest ice thickness and the largest thickness range of 8.8 m. This ice has undergone strong deformation, evident in skewed distribution and a significantly higher mean than modal thickness.
The ice thickness profiles for the FYI display similar characteristics in 2017 and 2019, while variations in thickness are larger and of shorter scale in 2018, indicating that the mode of sea ice formation could have been different in that year. This difference is also notable in the longer, heavier tail in the FYI thickness histogram.

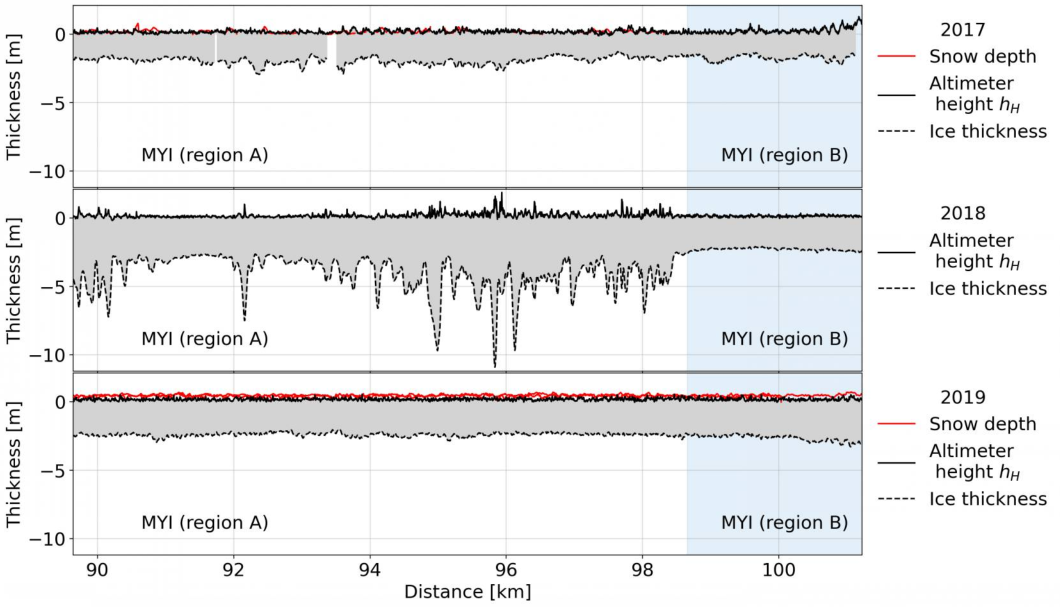

FIG. 4.3: MYI profiles (regions A and B) of altimeter surface height, snow depth, and negative ice thickness.

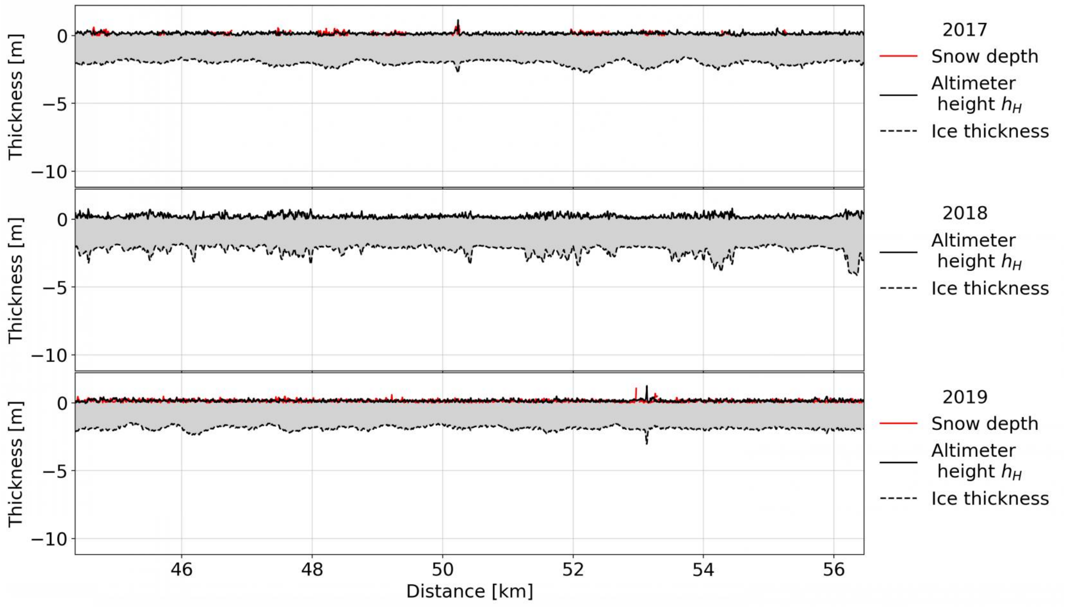

FIG. 4.4: FYI profiles (region C) of altimeter surface height, snow depth, and negative ice thickness.

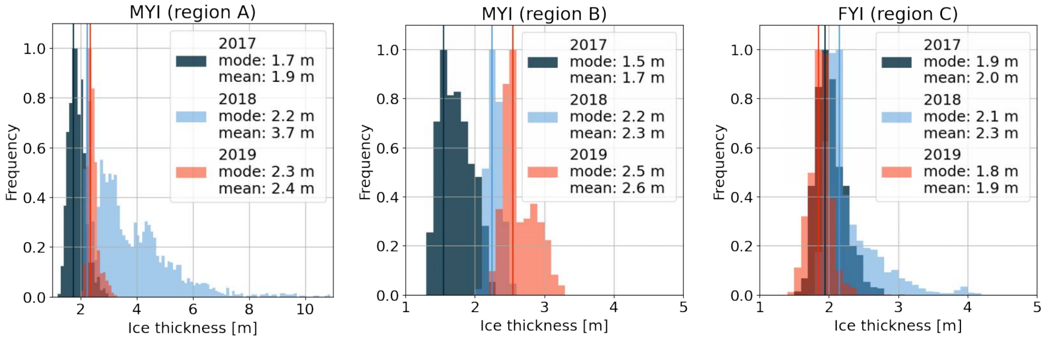

FIG. 4.5: Normalized ice thickness histograms.

4.4.2 Snow thickness

The average snow thickness on the ice plug is 0.20 m in 2017 and 0.42–0.48 m (averages of two different flights at different altitudes) in 2019. The mean snow thickness on the FYI is 0.18 m and 0.14 m in 2017 and 2019, respectively.

4.4.3 Surface and bottom roughness

The bottom RMS heights and slopes were calculated from the ice thickness in 50-m sliding windows and 500-m sliding windows. The bottom roughness is likely underestimated on the 50-m scale, because is within the diameter of the EM footprint. For the 500-m windows, the RMS height of ice thickness across all regions and years is higher by a factor of 3.1–5.7 than the RMS height in 50-m windows. The largest factor of 5.7 was found for the Old MYI in 2018. This scale-dependency of roughness and is further motivation to use the PSD and semivariogram approaches.

In order to compare the evolution of surface roughness to the evolution of bottom roughness, we asses that the decrease of bottom RMS height on the 50-m scale is 30% from 2017 to 2019, and 34% on a scale of 500 m. Building upon the result that the ALS topography shows no change in RMS height, the bottom roughness decreased more than the surface roughness. In 2018, sections with a larger mean surface roughness had a larger mean bottom roughness e.g., the Old MYI with largest bottom roughness has also the largest surface roughness. Such a behavior is not evident in the remaining years, where differences in roughness between the regions were smaller. The RMS slopes of the bottom roughness does not change from 2017–2019 while the surface RMS slope increases from 4.7 cm/m to 6.6 cm/m.

TABLE 4.4: Means of roughness parameters for ice thickness (Bottom, B) and single-beam altimeter (Surface, S).

	2017		2018		2019	
RMS height 50 m [cm]	B	S	B	S	B	S
MYI (A)	7.6	9.3	24.3	9.6	5.3	7.5
MYI (B)	6.7	11.0	3.1	5.5	5.2	7.6
FYI (C)	4.6	6.5	10.2	9.4	4.1	5.8
Old MYI			27.6	10.1		
RMS height 500 m [cm]	B	S	B	S	B	S
MYI (A)	28.5		138.6		18.8	
MYI (B)	22.0		9.7		22.7	
FYI (C)	20.4		39.1		15.1	
Old MYI			143.3			
RMS slope 50 m [cm/m]	B	S	B	S	B	S
MYI (A)	0.6	4.7	1.4	5.8	0.5	6.6
MYI (B)	0.5	4.8	0.3	5.1	0.5	6.6
FYI (C)	0.3	3.8	0.7	4.4	0.4	7.0
Old MYI			1.5	5 .2		

4.4.4 Melt pond fraction influence on thickness and roughness

The melt pond coverage of pixels coincident with the airborne measurement locations was extracted from S2 scenes after K-means clustering and classification. Refer to the profiles in Fig. 4.6 and 4.7 for thickness profiles color coded according to melt pond cover.

For the ice plug (section A) in 2017, the pond class has a mean thickness that is 18 cm larger than the mean thickness of the ice class. In contrast, the SYI (section B) in 2018 has a 10 cm larger thickness for the ice class, and the region of Old MYI has a 1.27 m larger thickness for the ice classes. In 2019, the ice class is 36 cm thicker than the pond class.

The differences in mean thickness between the classes for the FYI in 2017 and 2019 is negligible (absolute values below 5 cm). The rougher FYI in 2018 has a 13 cm difference between mean thickness of pond and ice class.

The RMS heights for the pond and ice class are similar, except for region A in 2018, which is a mix of SYI and Old MYI, where the pond class (predominately SYI) has half the RMS height of the ice class (predominately Old MYI).

TABLE 4.5: Regional means of ice thickness, melt pond fraction f_p, and altimeter RMS heights (50-m windows)

Year	2017			2018			2019		
Ice thickness [m]	pond	ice	f_p	pond	ice	f_p	pond	ice	f_p
MYI (A)	1.81	2.00	63	2.81	4.47	48	2.42	2.72	91
MYI (B)	1.73	1.57	93	2.29	2.38	99.6	2.57	2.93	82
FYI (C)	2.03	2.06	69	2.25	2.38	46	1.89	1.85	62
Old Ice				3.18	4.45	38			
RMS height [cm]	pond	ice		pond	ice		pond	ice	
MYI (A)	9.9	8.3		6.4	12.6		7.5	7.4	
MYI (B)	10.8	14.3		5.5	5.8		7.6	7.9	
FYI (C)	6.4	6.8		8.6	9.1		6.1	5.6	
Old Ice				7.6	11.6				

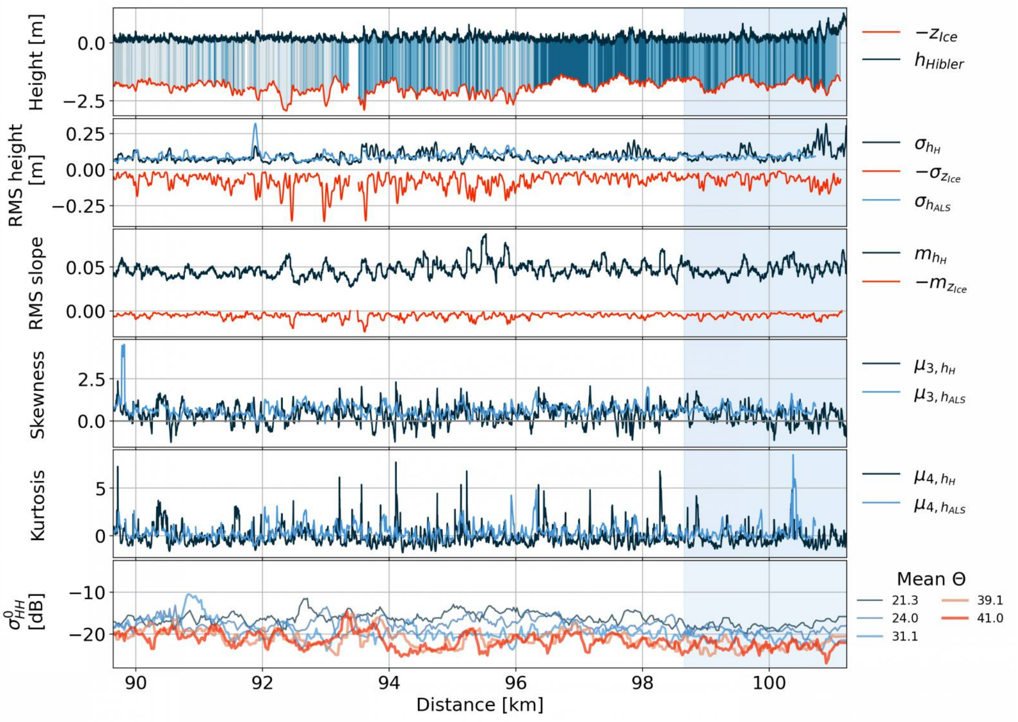

(A) 2017

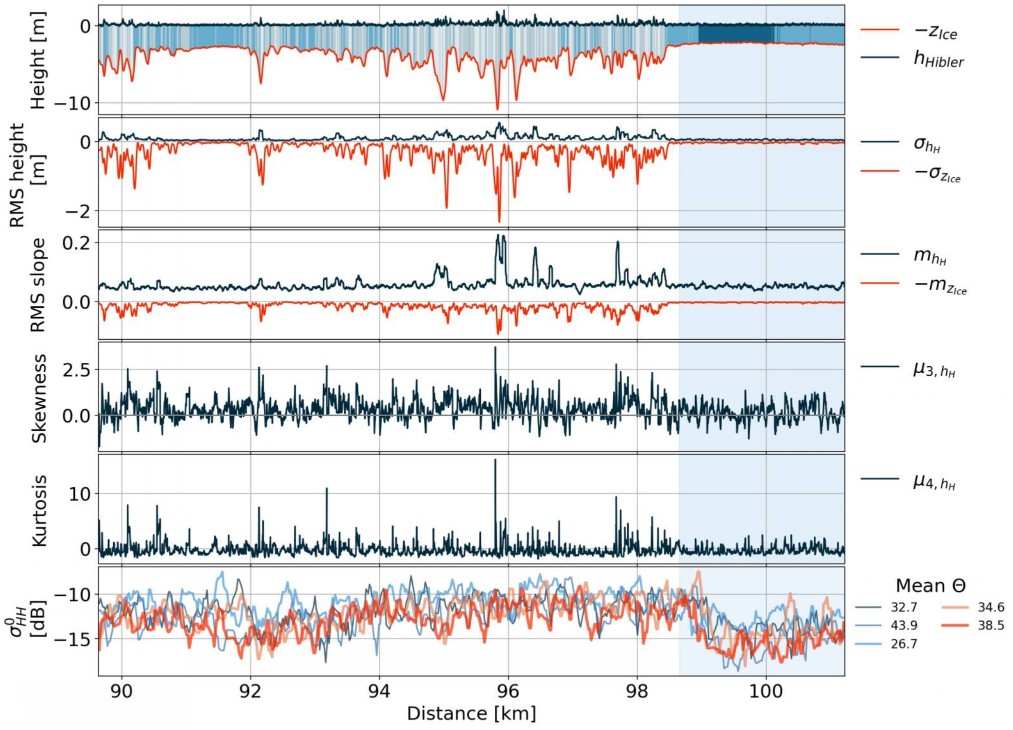

(B) 2018

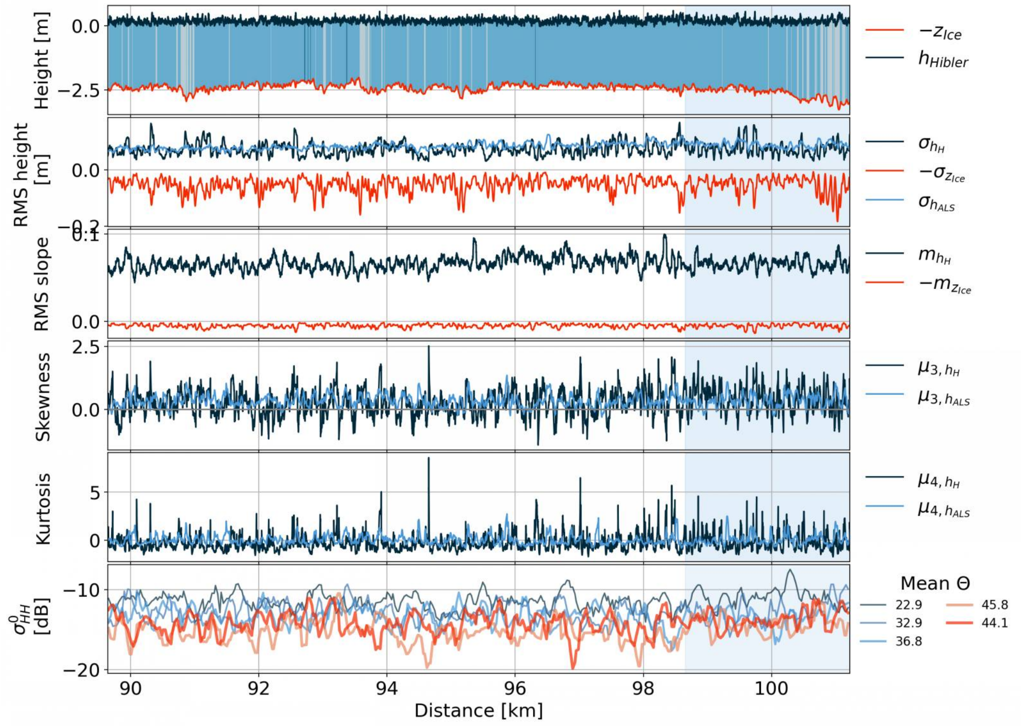

(C) 2019

FIG. 4.6: MYI profiles of various surface roughness parameters. Minus signs are used for all profiles of bottom roughness. The color scale of the ice thickness profile in the uppermost panel ranges from dark blue to white for the pond to ice class from clustered S2 images. The lowermost panel shows the backscatter profiles extracted from the S1 scenes with different incidence angles.

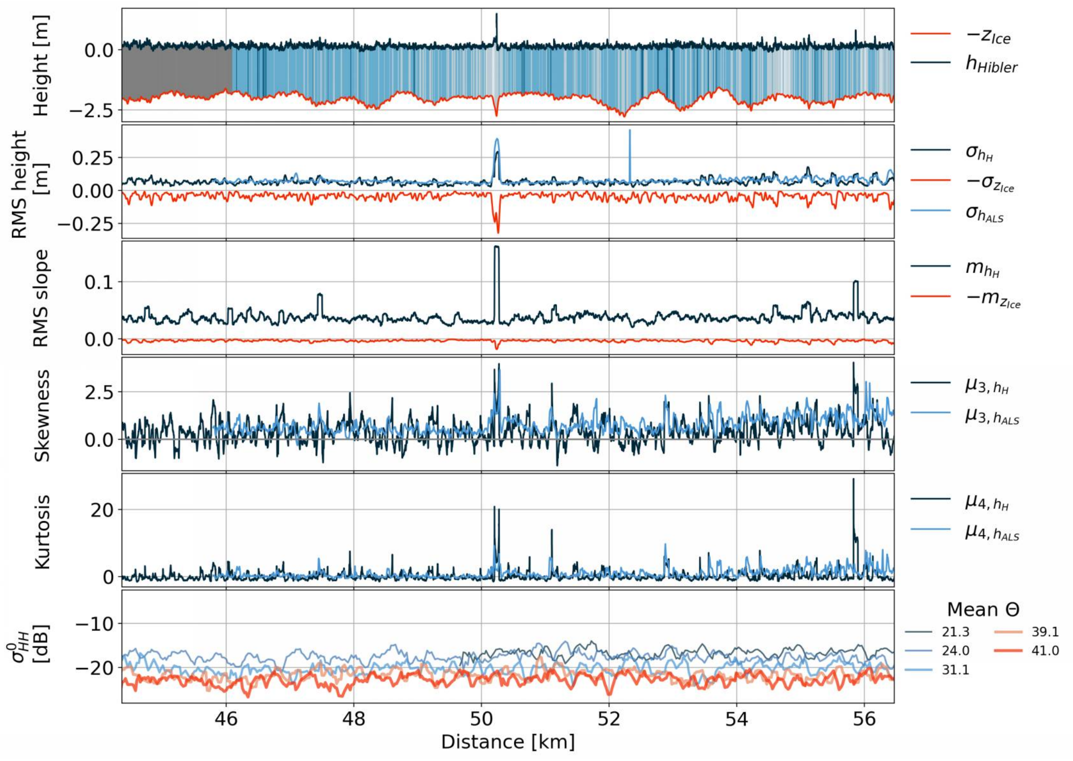
Height [m]
0.0
−2.5
$-z_{Ice}$
h_{Hibler}
RMS height [m]
0.25
0.00
−0.25
σ_{h_H}
$-\sigma_{z_{Ice}}$
$\sigma_{h_{ALS}}$
RMS slope
0.1
0.0
m_{h_H}
$-m_{z_{Ice}}$
Skewness
2.5
0.0
μ_{3,h_H}
$\mu_{3,h_{ALS}}$
Kurtosis
20
0
μ_{4,h_H}
$\mu_{4,h_{ALS}}$
σ^0_{HH} [dB]
−10
−20
Mean Θ
21.3
24.0
31.1
39.1
41.0
46
48
50
52
54
56
Distance [km]

(A) 2017

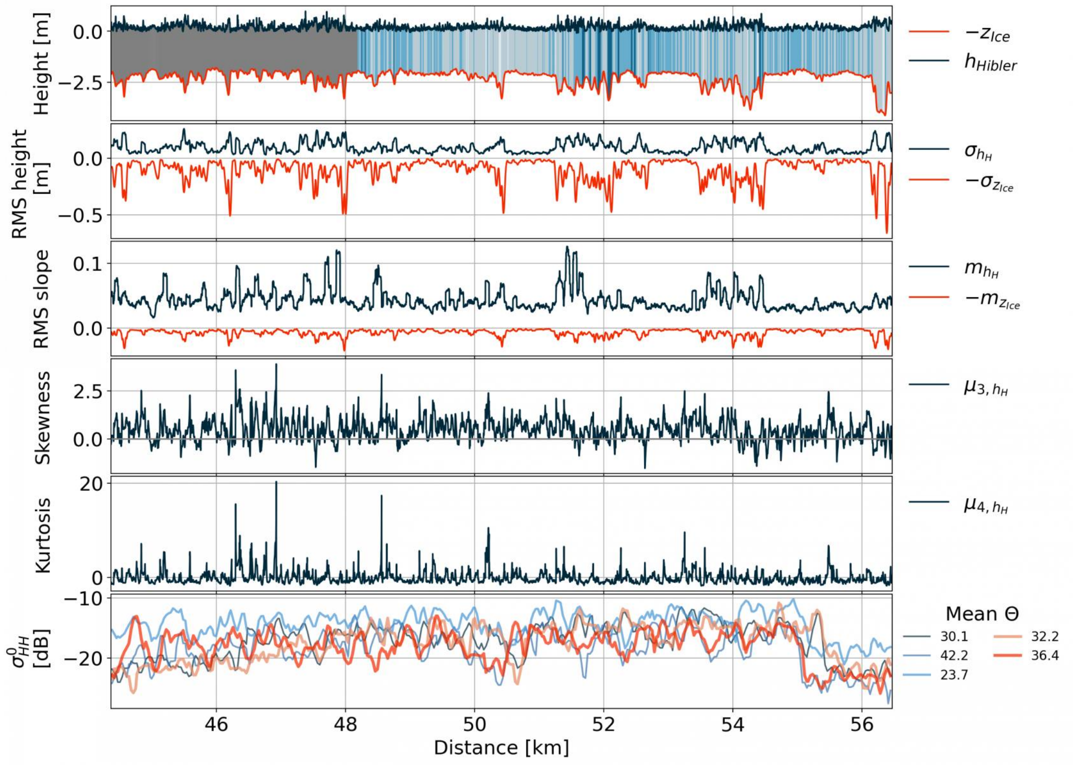
Height [m]
0.0
−2.5
$-z_{Ice}$
h_{Hibler}
RMS height [m]
0.0
−0.5
σ_{h_H}
$-\sigma_{z_{Ice}}$
RMS slope
0.1
0.0
m_{h_H}
$-m_{z_{Ice}}$
Skewness
2.5
0.0
μ_{3,h_H}
Kurtosis
20
0
μ_{4,h_H}
σ^0_{HH} [dB]
−10
−20
Mean Θ
30.1
42.2
23.7
32.2
36.4
46
48
50
52
54
56
Distance [km]

(B) 2018

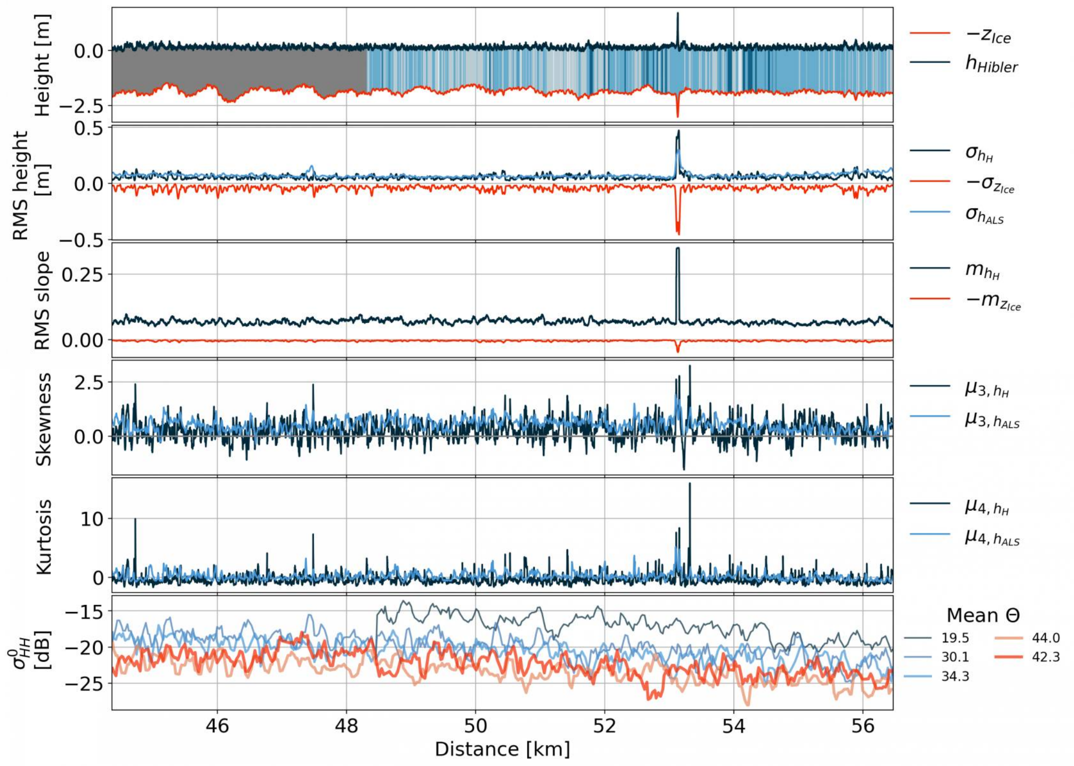

(c) 2019

Fig. 4.7: FYI profiles of various surface roughness parameters. Refer to Fig. 4.6 for a description. The brown color of the ice thickness profile in the uppermost panel is used for the section outside the S2 scenes i.e., the surface type is not classified.

4.4.5 Roughness estimation from PSD and semivariogram

Power spectral density

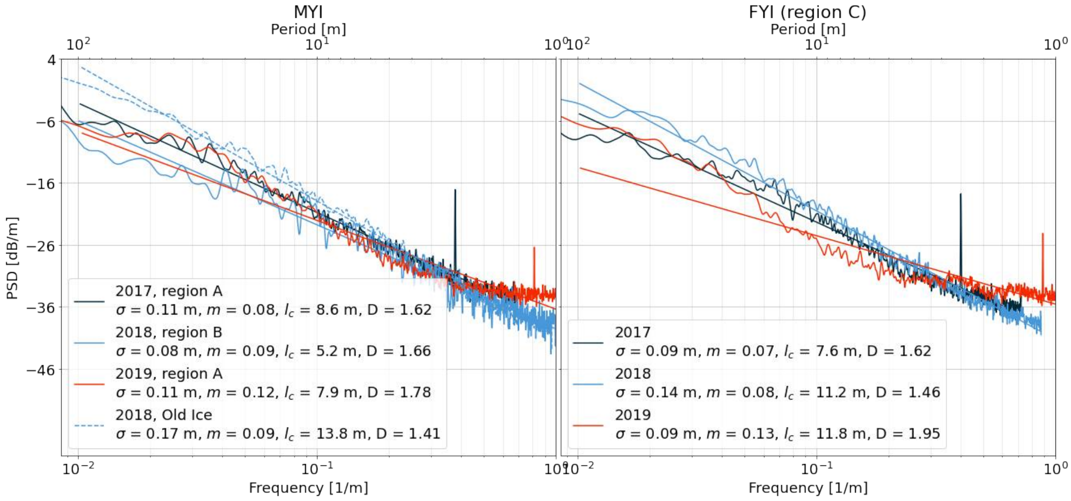

FIG. 4.8: PSD of surface height with estimates for RMS height σ, RMS slope m, correlation length l_c and fractal dimension D.

In the previous section, the RMS roughness for the surface was estimated on a scale of 50 m. By means of the PSD we can assess whether these estimates hold for the spatial scales of 0.5–100 m by calculating the zeroth moment of the PSD.

The PSDs for the surface heights in Fig. 4.8 have RMS heights of 11 cm for the ice plug in 2017 and 2019 (the corresponding RMS heights for the 50-m windows in Tab. 4.4 of the previous section were 9 cm and 8 cm). In 2018, the PSD estimate is 8 cm for the ice plug SYI (section B) and 17 cm for the Old MYI, while the 50-m windowing gave RMS heights of 6 cm and 10 cm. To summarize, the roughness estimates for the 0.5–100 m scale are consistently higher, but in the same order of magnitude as the roughness on a 50 m scale.

While the estimated RMS height in 2017 and 2019 is identical, the RMS slope increased slightly from 8 cm/m in 2017 to 12 cm/m in 2019. The respective 50-m-window estimates (Tab. 4.4) were 5 cm/m and 7 cm/m.

The correlation lengths range from 5.2 m to 13.8 m. In 2017 and 2019, the correlation lengths of the ice plug surface are similar with 8.6 m and 7.9 m, respectively. The FYI RMS heights, RMS slopes and correlation lengths fall in the same range as the respective parameters for the ice plug.

The slopes of the PSD on the log-log plot exhibit linear behavior on spatial scales from 100 m down to nearly 1 m, apart from the PSD of surface heights for 2019, which flattens out for scales smaller than 5 m. The fractal dimension D is estimated from a linear fit to the slopes. D covaries for MYI and FYI between the years, suggesting that the filtering of flight altitude variations could be responsible for the variability. The Old MYI and the FYI in 2018 have the lowest fractal dimensions. These sections had the highest RMS roughness.

The PSD of ice thickness (Fig. 4.9) has a steepening slope for wavelengths shorter than 50 m, where smoothing from overlapping footprint is expected to

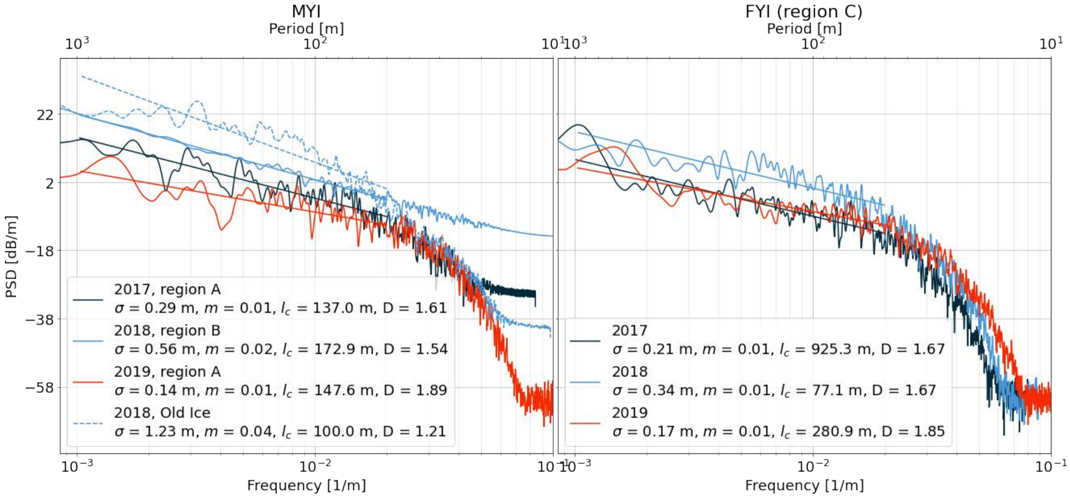

FIG. 4.9: PSD of ice thickness with estimates for RMS height σ, RMS slope m, correlation length l_c and fractal dimension D.

influence the signal. The RMS height from the PSD of ice thickness in region A halved from 29 cm in 2017 to 14 cm in 2019, while it is lower and more stable for the FYI, with 21 cm and 17 cm, respectively. The PSD estimate of RMS height is higher than that for the 50-m-windows. Instead, the PSD roughness estimates (29 cm in 2017, 14 cm in 2019 for region A) are in the same range as the RMS estimates for the 500-m-windows (29 cm in 2017, 19 cm in 2019, region A). The PSD method supports that the observed decrease in roughness on scales of 50 m and 500 m can be extrapolated to the spatial scale from 50–1000 m.

The correlation length l_c is shortest for the Old MYI and the FYI in 2018. l_c increases only slightly from 2017 to 2019. The estimation of fractal dimension largely depends on the choice of the frequency interval for fitting of a linear model, the absolute values should not be taken at face value. The rough Old MYI in 2018 has the lowest fractal dimension. An increase from 2017 to 2019 in fractal dimension is seen, but an increase is also observed for the landfast FYI, so a higher fractal dimension cannot be unambiguously attributed to MYI evolution.

Semivariance

The mean variograms of surface heights for the ice plug in Fig. 4.10 show a decrease in range over time (74 m in 2017, 42 m in 2018, and 38 m in 2019), indicating that the surface heights are spatially uncorrelated after shorter distances. The semivariogram for the Old Ice in 2018 can be found in Fig. A.5 in the Appendix. The Old ice has a range of 56 m. The sill value in 2017 of 0.021 m^2 corresponds to a standard deviation of $\sqrt{0.021}$ m $=$ 14 cm. In 2019, the sill of 0.009 m^2 corresponds to a standard deviation of 9 cm, which is of similar magnitude as the RMS heights in the previous section and show a slight decrease. The Old MYI in 2018 has the highest sill of 0.024 m^2 (15 cm).

All semivariograms show a "hole effect", where the variogram decreases from a local maximum located between 50–100 m to a local minimum located between

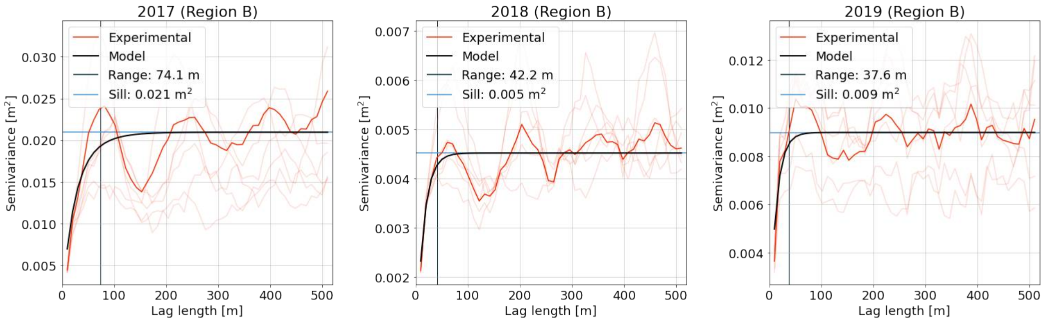

Fig. 4.10: Surface height semivariograms for MYI. For an overview of the mean variograms for each year drawn the the same scale, see the Appendix.

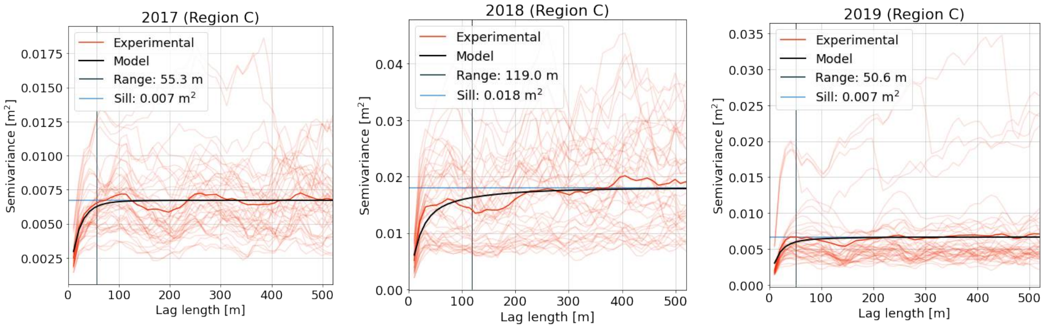

Fig. 4.11: Surface height semivariograms for FYI.

100–150 m and then increases again. This form arises from regular repetition in the process. A variogram that continues to fluctuate with a wave-like form with increasing lag distance indicates periodicity (Webster and Oliver, 2007). The hole effect is most pronounced in 2017 (see Fig. A.6 in the appendix for a plot of the semivariograms to the same scale).

For comparison, the semivariograms of the FYI can be found in Fig. 4.11.

Ice thickness variograms in Fig. 4.12 show a decrease in range from 2017 to 2019 in the MYI region B, together with a decrease in sill values, however, a similar variability of sill and range can be seen for the thickness profiles of the FYI in Fig. 4.13, therefore the observed decrease of the spatial scale where the ice thicknesses become spatially uncorrelated, and the decrease in roughness must not be a direct cause of the evolution of the MYI. It is not so clear weather the exponential model captures the ice thickness semivariograms well e.g., the modeled variogram for 2017 in Fig. 4.12 deviates from the experimental variograms for short lags.

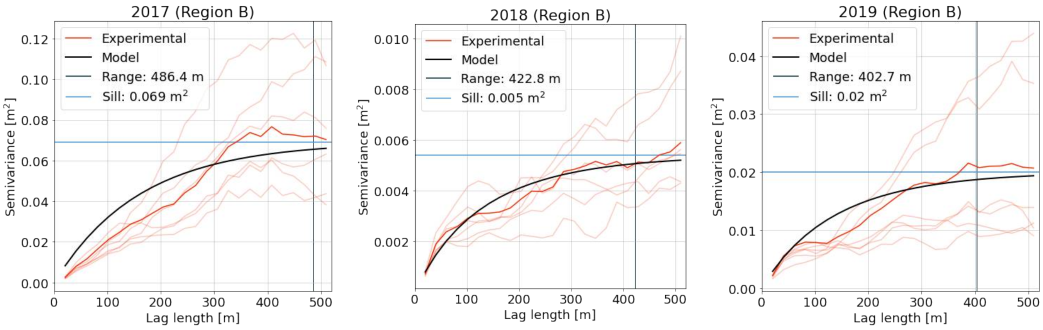

FIG. 4.12: Ice thickness semivariograms for MYI. For an overview of the mean variograms for each year drawn the same scale, see the Appendix.

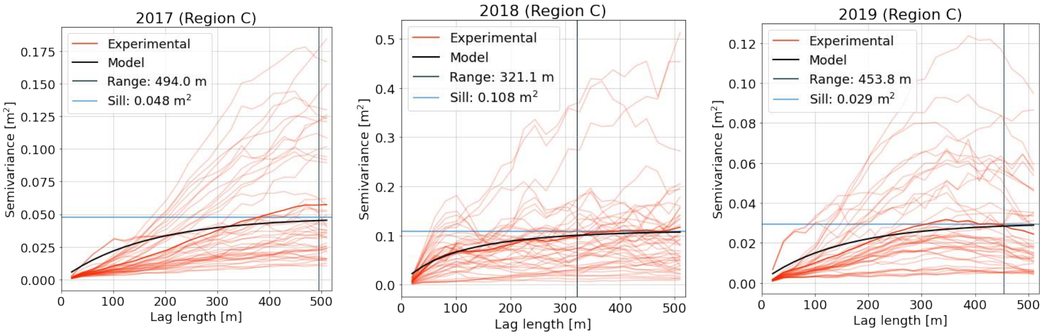

FIG. 4.13: Ice thickness semivariograms for FYI.

4.5 Sentinel-1 backscatter evolution

Fig. 4.14 shows Sentinel-1 images of σ^0_{HH} for October 2016, and the dates around the airborne surveys. The selected images have similar incidence angles. Enlarged views of the MYI regions A and B, and FYI (region C) are depicted in Fig. 4.15. In October 2016, the Old MYI in the east shows highly variable backscatter, which appears similar in pattern and intensity to the pack ice on the Arctic Ocean. Distinct areas of low backscatter within the consolidated pack ice could be heavily snow-covered ice or sub-surface melt ponds (refer to p. 97 in Carsey, 1992 for a case study of MYI floe backscatter). Until March 2017, the backscatter variability within the Old MYI ice remains high, but by 2018 the backscatter of this region became more uniform, a continuing until 2019.

The landfast ice which formed in situ in 2016 has a homogeneous backscatter with only small regions of higher return, where old floes were present during freeze-up in 2016. The backscatter contrast between the eastern Old MYI and the younger ice of the western part of the ice plug decreases over the years. The minimum extent of the plug in 2017 is clearly visible in 2018 through a higher backscatter of the SYI compared to the adjacent FYI. The same statement is valid for 2019, where the minimum extent from 2018 is distinguishable. In 2018, backscatter of the plug appears to be slightly higher where melt water pooled excessively in 2017, and where the sparse MYI floes were incorporated in 2016.

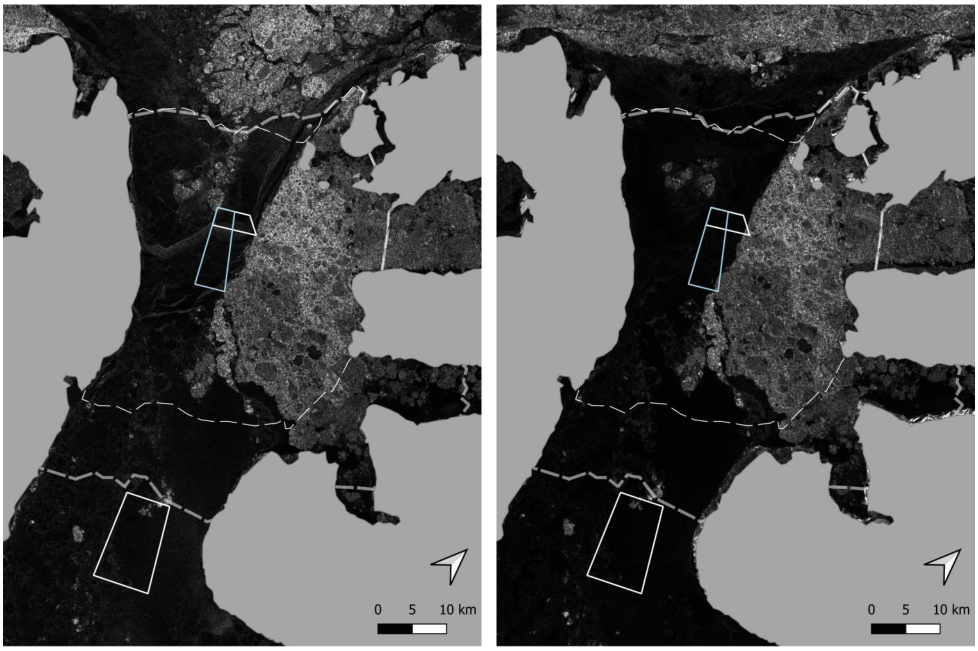

(A) 2016-10-31 (B) 2017-03-29, $\theta = 41°$

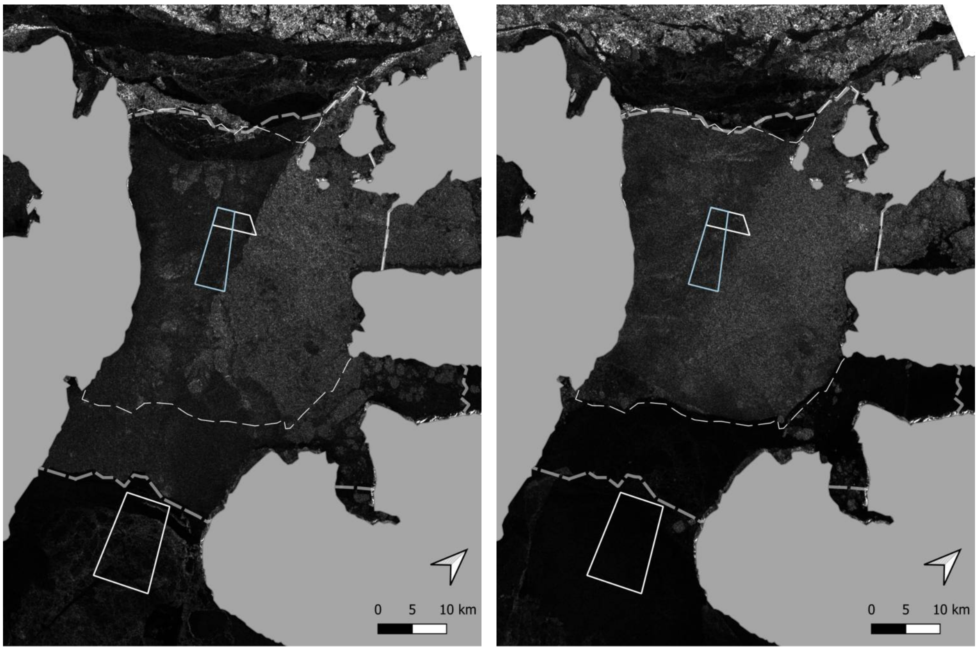

(C) 2018-04-06, $\theta = 44°$ (D) 2019-04-01, $\theta = 43°$

FIG. 4.14: Sentinel-1 backscatter σ^0_{HH} for autumn 2016 and the dates around the airborne surveys. θ is the mean incidence angle for pixels coincident with the survey tracks over the ice plug.

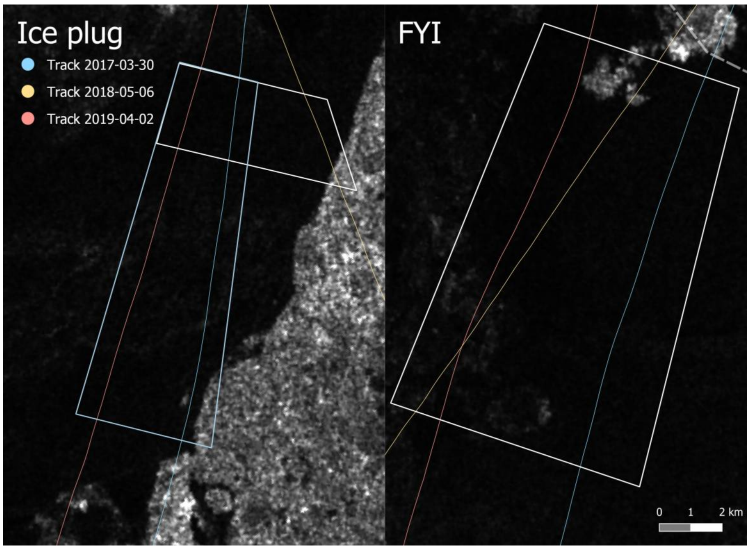

(A) 2017-03-29

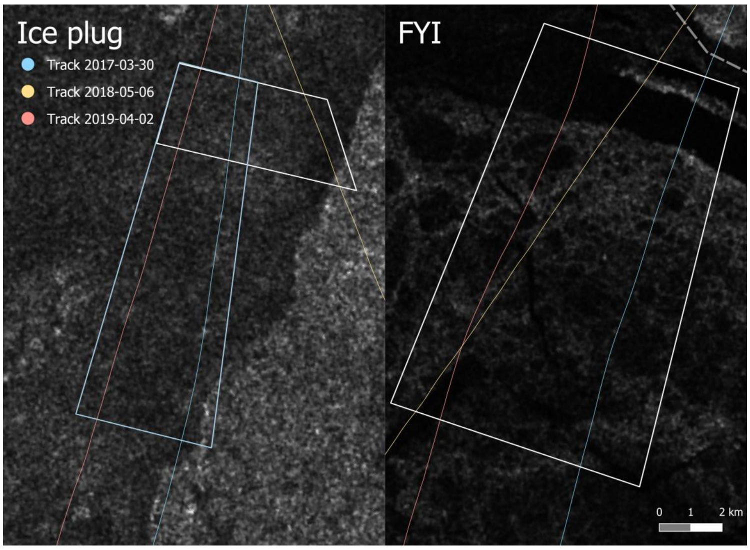

(B) 2018-04-06

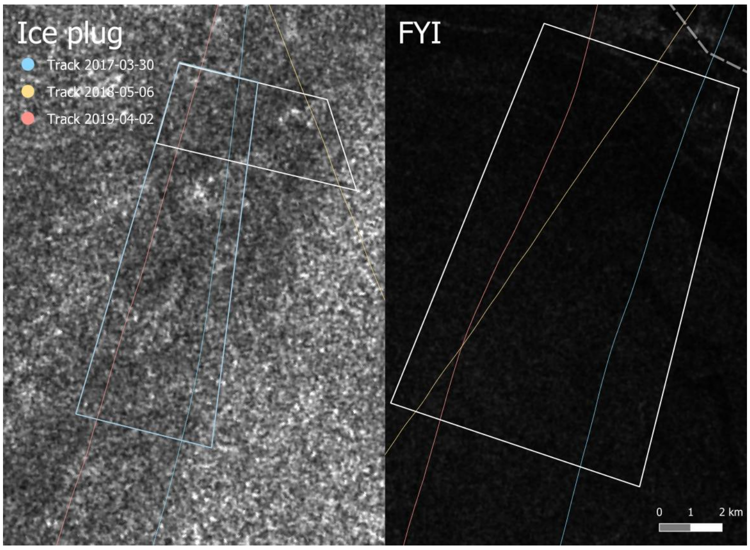

(C) 2019-04-01

FIG. 4.15: Sentinel 1 backscatter σ^0_{HH}. Enlarged sections of the scenes in Fig. 4.14.

σ^0_{HH} of the ice plug increased from -20.8 dB to -13.9 dB, and -13.0 dB throughout the years. The FYI ice had a mean σ^0_{HH} of -19.8 dB, -17.1 dB, and -20.7 dB around the dates of airborne surveys in 2017, 2018, and 2019, respectively.
For the ice plug, the mean σ^0_{HV} increased from -29.0 dB in 2017 to -25.3 dB in 2018, and -23.2 dB in 2019. This increase in backscatter is typical for MYI as a result from desalination and increasing porosity (Carsey, 1992). σ^0_{HV} of the seasonal landfast FYI was constant with -28.3 dB in 2017, -26.1 dB in 2018, and -29.5 dB in 2019.

4.5.1 Dependence of backscatter on incidence angle

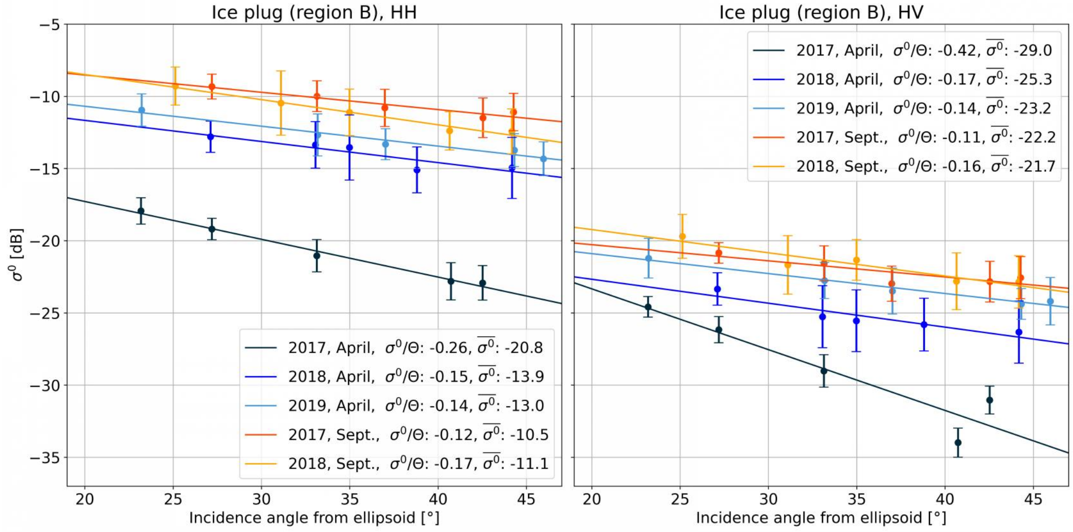

Fig. 4.16: Linear regression scatter plots for $\sigma^0(\theta)$ of the ice plug. Error bars are 1 standard deviation of σ^0.

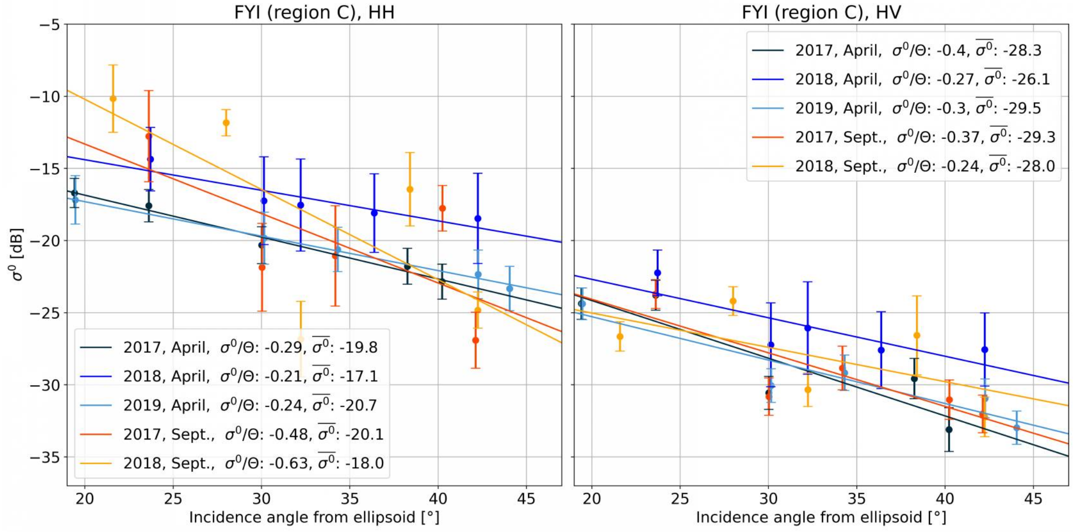

Fig. 4.17: Linear regression scatter plots for $\sigma^0(\theta)$ of FYI.

Fig. 4.16 shows the linear regression $\sigma^0(\theta) = a \cdot \theta + b$ of the backscatter versus incidence angle for the ice plug (region B) and Fig. 4.17 gives the result for the seasonal landfast FYI for HH and HV polarization.
For the ice plug, the slope a decreased from -0.26 dB/1° in spring 2017 to -0.15 dB/1° in spring 2018. a remained constant from spring 2018 to spring 2019. The slope in September 2017 (-0.12 dB/1°) is already smaller than the slope in spring 2017. The slope of $\sigma^0_{HV}(\theta)$ decreased from spring 2017 to autumn 2017, and remains between -0.11 to -0.17 dB after this first melt season.
The landfast FYI shows no trend in slopes for σ^0_{HH} or σ^0_{HV}, and the slopes are consistently higher than the MYI slopes. The highest recorded slopes are those for σ^0_{HH} in autumn 2017 and 2018, however the correlation is weaker, with $R^2 = 0.7$. For all other regressions R^2 is above 0.9 and the slopes range from -0.21 to -0.29 dB/1° (Tab. B.3).
In order to address the scattering evolution of the Old MYI overflown in 2018, we repeated the determination of incidence angle dependence and mean backscatter for the pixels below the track flown in 2018 (Fig. 4.18). The Old MYI has a near constant mean σ^0 and incidence angle dependence throughout 2016–2019. The part of the ice plug that formed in 2016 shows an increasing mean HH and HV backscatter, approaching the backscatter of the Old MYI in 2019, consistent with the visual impression of decreasing contrast of the ice types in Fig. 4.15.

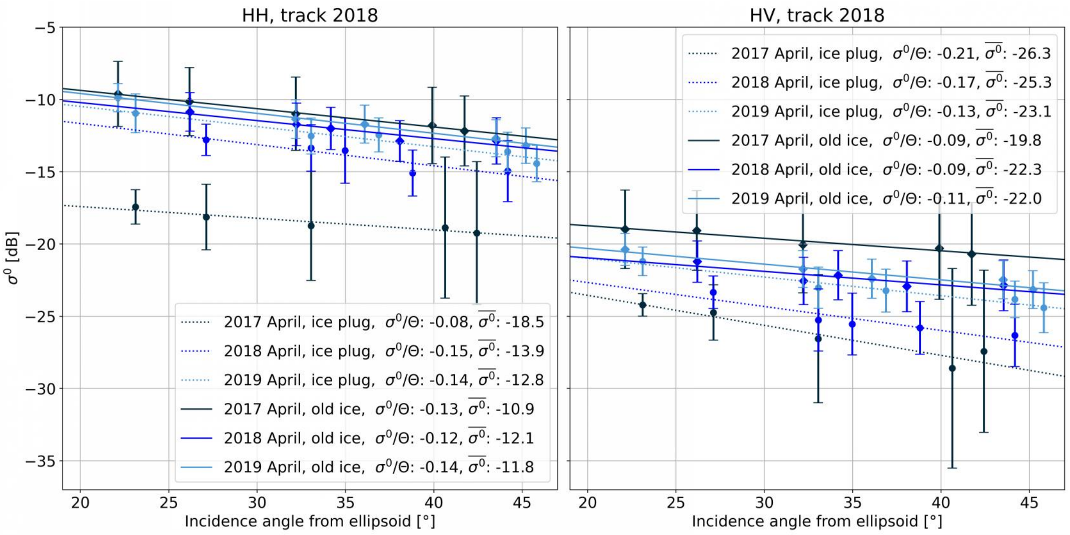

FIG. 4.18: Linear regression scatter plots for $\sigma^0(\theta)$ of pixels below the survey track from 2018 for the western section of the ice plug formed in 2016 (dashed lines), and the eastern section of the ice plug (Old MYI, solid lines).

4.6 Role of climatic conditions for stability

4.6.1 Surface energy budget

The seasonal evolution of the radiation budget in Fig. 4.19 exhibits the expected positive summer radiation balance and a negative balance in winter.

The surface energy budget (Tab. 4.6) for the summer seasons was highest in 2019, and lowest in 2018. The percentage difference between 2019 and 2018 is 114%. September–May radiation balance for 2016–2017, and 2018–2019 was similar, but the balance was lower for winter 2017–2018.

TABLE 4.6: Seasonal means of net surface radiation, and cumulative total precipitation

Season	Start date	End date	Radiation balance [W/m^2]	Total precipitation [cm]
summer	2016-06-01	2016-08-31	16.7	28.2
summer	2017-06-01	2017-08-31	16.3	30.4
summer	2018-06-01	2018-08-31	15.7	24.4
summer	2019-06-01	2019-08-31	18.0	21.4
winter	2016-09-01	2017-05-31	-2.9	30.7
winter	2017-09-01	2018-05-31	-3.5	20.6
winter	2018-09-01	2019-05-31	-2.6	22.6

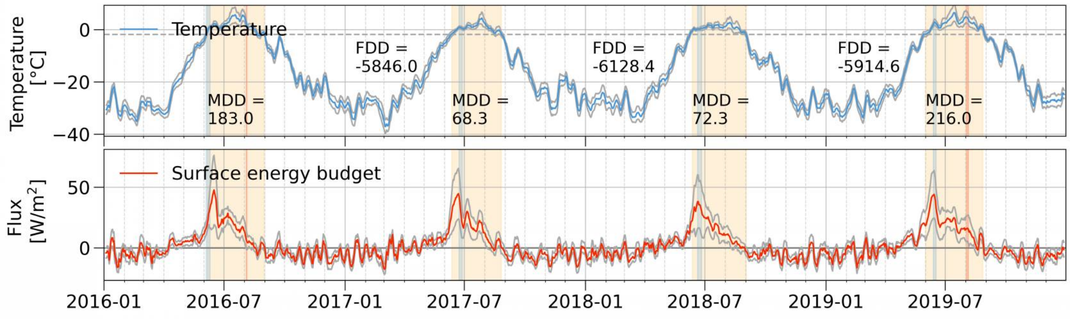

FIG. 4.19: ERA5 2 m air temperature and radiation balance (7-day moving averages). Grey lines are the standard deviation of the respective variable in the region. Highlighted in Orange: Seasons with daily mean temperatures above -1.8°C. Highlighted Blue: Onset of melt pond formation from MODIS images. Highlighted Red: Breakup events.

4.6.2 MDDs, mean temperatures, and melt periods

In every summer season, the radiation balance became positive 2–4 weeks earlier than the date where temperatures rose above -1.8°, as can be seen from the radiation and temperature cycles in Fig. 4.19.

The cumulative MDDs in 2018 and 2016 were in the order of 35% the MDDs in 2016 and 2019. The melt onset (Tab. 4.7) in the years 2016 and 2019 was 6 and 11 days earlier than in the years with a stable ice plug. Accompanying this, the start of melt pond formation on the ice plug from MODIS images indicates a later onset in the years where the ice plug remained intact. Melt season duration anomalies in the Canadian Arctic Archipelago from 1979–2018 are reported in Howell and Brady (2019). The melt onset was 10 days earlier than normal in 2016, 2 days earlier in 2017, but 10 days later in 2018.

The mean summer air temperatures in 2017 and 2018 were about 1.5°C colder than in 2016 and 2019. 2016 had a positive temperature anomaly, while 2017 and 2018 had negative anomalies according to the 1997–2018 temperature anomalies reported for June, July, and August, for the Canadian Arctic Archipelago (Dauginis and Brown, 2021).

TABLE 4.7: Melt season onset, offset, duration, average temperature, and MDDs.

Year	Melt onset date	Melt offset date	Duration [d]	$\overline{T_{2m}}$ [°C]	MDD
2016	06-06	08-31	86	2.4	183.0
2017	06-12	08-26	75	0.9	68.3
2018	06-12	09-02	82	0.9	72.3
2019	06-01	08-27	87	2.6	216.0

The start of the winter freezing season with temperatures below -1.8°C, the mean winter temperatures, and the FDDs exhibit no notable differences between the years.

TABLE 4.8: Freezing season onset, offset, duration, average temperature, and FDDs.

Onset date	Offset date	Duration [d]	$\overline{T_{2m}}$ [°C]	FDD
2016-08-31	2017-06-12	285	-20.7	-5846.0
2017-08-26	2018-06-12	290	-21.2	-6128.4
2018-09-02	2019-06-01	272	-21.6	-5914.6

4.6.3 Wind speeds

Fig. 4.20 shows the time evolution of the wind vector, wind speed, surface pressure, and total precipitation. The 10-m wind speed is assessed for anomalously strong winds or wind directions in the time period where the plug disintegrated in 2016 and in 2019. No extreme wind conditions were found (Tab. B.6 and Tab. B.5 in the Appendix). The surface pressure and total precipitation at the times of the break-ups do also not show any abnormal values.

4.6.4 Estimates of summer ablation

The positive surface radiation balance contributes 0.3–0.4 m of ice ablation, the variability between the years is small. The influence on the ablation from the snow cover, which is assumed to melt completely before the ice melts, is small. If no snow were melted, the ablation would be 0.1–0.2 m higher in each season.

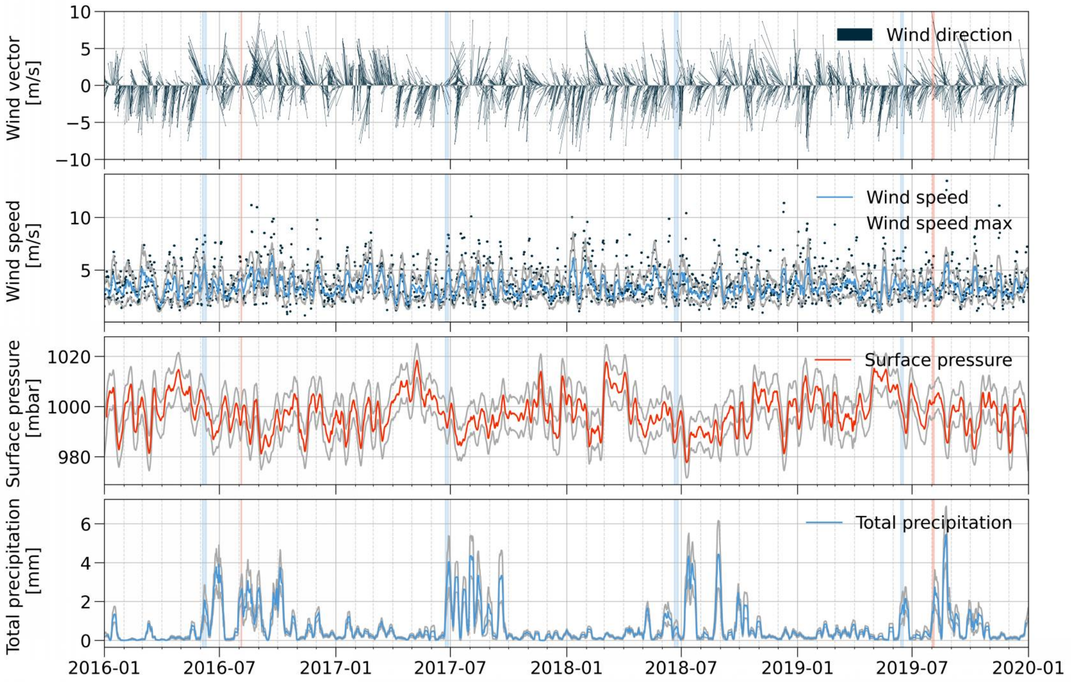

Fig. 4.20: ERA5 wind direction, wind speed, surface pressure, and total precipitation (7-day moving averages), grey lines are the standard deviation of the respective variable in the region.

Table 4.9: Summer ablation from mean net surface radiation.

Season	Net radiation [W/m^2]	Total mass melted [kg/m^2]	Snow depth [m]	Ice melted [m]
Summer 2016	16.7	397	0.2	0.4
Summer 2017	16.3	388	0.2	0.4
Summer 2018	15.7	374	0.2	0.3
Summer 2019	18.0	428	0.4	0.3

The annual ablation from the MDD model varies greatly. While the contribution to ablation in 2017 and 2018 is negligible, the summer melt in years with breakup is in the order of 0.7–1.4 m. This is certainly an overestimation of the melt rate, but illustrates that the effect of the increase in summer temperatures from 0.9°C to 2.5°C is an important factor to the instability of the ice plug.

Table 4.10: Minimum and maximum summer ablation for minimum degree day factor and maximum degree day factor.

Season	MDD	Snow depth [m]	Ice melted (min) [m]	Ice melted (max) [m]
Summer 2016	183	0.2	0.9	1.4
Summer 2017	68	0.2	0.01	0.02
Summer 2018	72	0.2	0.05	0.07
Summer 2019	216	0.4	0.7	1.0

5 Discussion

5.1 Processing of altimeter data

Two filtering methods of flight altitude variations from the single-beam altimeter heights were implemented. The assessment of the performance of the methods is based on the coherence of the DGPS signal with the raw altimeter signal for the survey in 2018. The coherence of the DGPS heights with the altimeter ranges demonstrates that for frequencies below 0.1 Hz (corresponding to a spatial scale of 500 m and longer) the flight altitude variations dominate the altimeter range signal. A sharp decrease in coherence is found between 0.1–0.5 Hz. Above 0.5 Hz, corresponding to distances shorter than 100 m, the surface altitude variations are responsible for about 90% of the signal power.

The first method fits a spline to the maximum ranges, which represent the local level surface height, by adjusting the weights of the data points in an iterative process. This method is inappropriate, because the coherence function does not follow the expected curve.

The second method represents a modification to Hibler's method in that it uses the curvature of an initial spline to find local maxima. This method is sensible to the spacing of knots for the initial spline. The spacing was chosen to be about 100 m, which leads to a coherence of raw range signal and filtered heights which closely follows the desired coherence behavior. The transition region is smaller than for the original Hibler method, which is a minor improvement for the flight in 2018, at least. The coherence for smooth ice is 0.7 and for rough ice is 0.9 on scales shorter than 50 m. For smooth surfaces, the aircraft altitude variations contribute proportionately more variability than for rougher surfaces, explaining the weaker performance over level ice. This might lead to larger percentage errors for surface roughness estimates over level ice. Prospectively, the analysis of coherence could precede the filtering in order to determine a suitable cut-off frequency for the high pass filter, at least for flights where DGPS data from the EM Bird is available.

Furthermore, I attempted to use the Bird DGPS heights directly to correct for the aircraft altitude variations, which left large low frequency oscillations, that could be explained by pitch and roll of the bird, which could be improved upon by employing an INS in the Bird. If one decides to use the combined DGPS and INS data to correct for the flight height variations, absolute surface heights above the ellipsoid can be obtained. This would enable surface profile characterization on spatial scales longer than the cut-off length in the high pass of the (modified) Hibler method.

5.2 Comparison of altimeter and ALS derived surface roughness

In 2017, the ALS data is compromised due to gaps in the GPS data, and in 2019 the ALS DEM suffers from drift in along-flight direction and tilt in across-flight direction. This makes the use of directional roughness parameters, and roughness determination on larger scales impossible, which would have been the added value of ALS compared to the single-beam altimeter.

Nevertheless, we can compare the regional mean values of the ALS roughness parameters within the EM footprints and the altimeter roughness parameters for 50-m moving windows. The RMS height and the skewness agree between the instruments, while the kurtosis is negative for the ALS but positive for the altimeter in three out of four cases.

The laser scanner mean RMS height was found to be stable for the ice plug (8.9 cm in 2017, 8.6 cm in 2019) and for the seasonal landfast ice on Nansen Sound (7.5 cm in 2017, 7.2 cm in 2019). The altimeter RMS height exhibits more variability between the years and suggest a decrease in surface roughness for the ice plug from 9.3 cm in 2017 to 7.5 cm in 2019. The broader distributions of roughness parameters from the altimeter indicate that the amount of extremely smooth ice and extremely rough ice is overestimated from the altimeter profiles, and the variability in skewness.

The EM ice thickness retrieval could benefit from the ALS, because a more accurate mean surface height within the footprint could be obtained. Furthermore, the DEMs could be used to determine a topography-dependent measurement uncertainty. If large off-nadir features e.g., leads or ridges are detected, the ice thickness is more likely to be underestimated, and hence should be attributed a larger uncertainty. Those benefits come with more complex data processing compared to an altimeter, thus the worth of a scanner compared to an altimeter is dependent on the survey objectives, the sampled surface, and the measurement platform (Beckers et al., 2015).

5.3 Ice thickness and roughness evolution

For tracking of the inter-annual evolution of the ice plug, it would have been preferential to have the tracks in proximity, which was not accounted for when planning the surveys. The spacing of the flight tracks is such that only short subsections are close enough, and therefore suitable to describe the ice evolution. Only the survey of 2018 covers the eastern cluster of old and rough MYI. Identifying the time evolution of this matrix of floes would have been an appropriate research goal, as it offers a target that is typical for MYI in the Arctic Ocean, but stationary and not subjected to deformation. It is suggested that in future campaigns, more attention should be paid to special features.

Landfast FYI thickness in the CAA was reported to be 2.0–2.3 m on average (Howell et al., 2016). The measured mean ice thickness of the landfast FYI south of Nansen Sound ice plug is 1.9–2.3 m, which coincides with the literature value within the limits of accuracy of the measurements (±15 cm). In 2017, the mean thickness of the ice that will remain in place as the ice plug is 1.9 m. After the second winter, this ice has thickened to a mean of 2.3 m. The two ice types that make up the ice plug were surveyed in 2018, evident in the multi-modal ice thickness distribution with the strongest mode at 2.2 m representing the locally formed SYI, and modes around 3 m and 4 m representing the old, deformed MYI. The values of the higher modes are a typical thickness for the pack ice at the Arctic Ocean north of the ice plug.

Historical excursus
Serson (1972) used a simple FDD model with a constant of 6000 FDDs, together with a summer ablation of 40 cm to arrive at 2.6 m and 3.1 m for SYI and third year ice thickness. ERA5 2-m temperatures for 2017–2019 show that the FDDs have not changes significantly, but the ablation rate in summer or the oceanic heat flux might well have changed. Sadler and Serson (1981) reported 3.5 m thick ice for the SYI of the Ice plug. This historic SYI thickness far exceeds the thickness in 2018, and also the thickness in 2019, indicating that climatic conditions must have been different.

The snow thickness in 2017 was 20 cm in the area that will remain landfast for the next two years, but the data is sparse, because measurements with high pitch or roll angles are excluded in the processing, and the flight was very turbulent (S. Hendricks, personal communication, April 30, 2021).

The snow in 2019 was 42 cm deep on the ice plug, compared to only 14 cm on the seasonal landfast FYI. This remarkable difference might have several reasons:

Snow can accumulate on the ice plug before FYI forms. From MODIS images and ice charts, the period between first snow fall and freeze-up of the sound is 16 September–1 October. At Eureka weather station, 5 of 23 mm of the whole winter precipitation were recorded in this period. Alert recorded 2 of 85 mm in the same period. Thus, it is unlikely that earlier accumulation on the ice plug alone accounts for the 28 cm difference in snow thickness at the end of winter. Very likely the decayed MYI of the plug with depressions from drained melt ponds, catches the snow better, compared to the level FYI. An indication of preferential snow accumulation in drained melt ponds is the brighter appearance of the surface in areas where melt ponds prevailed (Sentinel-2 image, Fig. 5.1). Regional differences in snow redistribution due to different topography of the adjacent mountains could also contribute to dissimilar snow depths between ice plug and landfast FYI.

In 2017, those ice plug sections covered by melt ponds in summer were 18 cm thinner in spring than those sections without melt ponds, if we look at the 11 km section A, however in the subsection B, the melt pond covered ice even had a 19 cm larger mean thickness. Similarly, Landy et al. (2014) observed for an in situ study of a 100 m x 100 m landfast FYI area that throughout the entire melt season, ponds were present on nearly the full range of premelt elevations. This is what we also observe on the FYI: Even the rougher FYI in 2018 has only a 13 cm difference between mean thickness for surfaces with differing melt

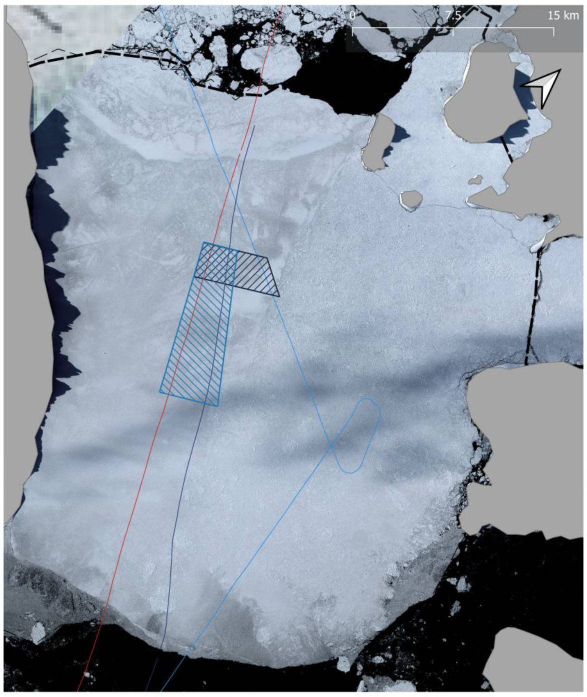

Fig. 5.1: Brightness and contrast enhanced Sentinel-2 scene from 2018-09-09. After snow fall, the areas which were covered by melt ponds appear brighter, indicating thicker snow.

pond cover in summer. The EM footprint might also be to large to resolve small-scale surface topography relevant for melt pond pattern.

In contrast to 2017, in 2019 the ice plug had a 36 cm larger mean thickness in areas where no melt ponds resided at the peak pond coverage of the previous melt season. This indicates that preferential melting below ponds over two melt seasons with similar pond patterns has had a detectable influence on the ice thickness. The higher summer ablation below ponds is not balanced by higher freezing rates of the thinned ice in winter.

Surface roughness obtained from the ALS DEMs exhibits no trend in the RMS heights. The mean skewness from ALS is decreasing from 0.7 to 0.3, indicating that the distribution of surface elevations became more symmetrical, hence losing the highest portion of elevations, which could be expected from weathering of peaks. The ALS kurtosis is also decreasing. However, the changes of skewness and kurtosis might not be attributed to the weathering and evolution of MYI. Because the FYI skewness and kurtosis values span have similar variability, the change in values for the ice plug is within the statistical fluctuation range. The consistency of surface roughness over two years can be attributed to snow smoothing out contrasts between areas of high and low summer ablation. This is supported by Nasonova et al. (2018) finding that snow masks surface roughness on the scales that we have considered.

For the undeformed ice, which is all regions except the Old MYI, the mean RMS heights in spring do not vary between pond covered ice and bare ice at the maximum melt pond extent in the following summer seasons. The Old MYI is the exception, where RMS height is about half for sections covered by ponds compared to sections with no ponds.

On the scale of 50 m, the ice thickness RMS height decreases from 7.6 cm to 5.3 cm, which is a 30% decrease. For the 500-m scale, this decrease is 34%, from 29 cm in 2017 to 19 cm in 2019. This difference of roughness on the two spatial scales is the combined effect of the smoothing of the ice thickness variations be the large footprint of the EM method and the rather large-scale variation in ice thickness for the undeformed sea ice. The decrease in ice roughness is either a result from the differing flight tracks or it reflects the basic principle, that thinner ice will grow faster, and hence differences in ice thickness should decrease over time, if forcing and physical properties are spatially uniform.

The PSD method was used to assessed roughness changes across spatial scales. The surface RMS height estimated from the PSDs stayed about constant from 2017 to 2019, in agreement with the ALS-derived RMS heights. In contrast to the surface, the ice thickness RMS height decreased from 28 cm to 14 cm, supporting the findings from the moving average method. The rougher FYI thickness profile in 2018 has the shortest correlation length, followed by the Old MYI. Interestingly, the shorter ice thickness correlation length of this old, rough ice comes with the longest surface height correlation length of all ice types.

Von Saldern et al. (2006) found 1.3–1.9 for the fractal dimension D for altimeter surface height profiles. In this study, the values of D for the surface heights are within this range. The range of D for ice thickness is slightly larger than that of Gneiting et al. (2012) from upward looking sonar (1.2–1.5). For both, surface and thickness fractal dimension, the roughness apparent from looking at the profiles does not seem to be reflected in the fractal dimension, as we would expect the rough Old MYI in 2018 to have a higher fractal dimension, where in fact it has the lowest D value of all profile sections, followed by the also notably rougher FYI in 2018.

The added value of the variogram method is not so clear, as the range and sill parameters depend on the choice of a valid model and should reflect the same inter-annual variability as the estimates of RMS height and correlation length from the PSD. The origin of the wave-like fluctuations with a spacing of about 100 m in the semivariograms of surface heights needs to be looked at closer. A possible explanation is offered by Iacozza and Barber (1999), who investigated snow depths over various types of sea-ice and found that the regular smooth ice topography of FYI produced a periodicity in the snow drifts. The most suitable variogram for this surface type was a combination of a wave (hole-effect) model with a Gaussian model. The more uneven ice topographies of the MYI sites were characterized by hummock-melt pond features that survived multiple melt seasons. These topographies produced a more irregular snow drift pattern, best modeled by a combination of the spherical and Gaussian variogram models (Iacozza and Barber, 1999). For studies with reliable ALS data, an effort could be made to calculate variograms in different directions, in order to address periodic surface structures and expected anisotropies in the topography e.g., from prevailing wind directions.

5.4 Sentinel-1 backscatter evolution

The angular dependence obtained for HH backscatter of MYI in this study is in agreement with -0.15 dB/1° reported by Aldenhoff et al. (2020) for MYI, but the slope for HV in this study (-0.14 to -0-17 dB/1°) is higher than the literature value of 0.07 dB/1°.

The backscatter dependence of the ice plug halved from spring 2017 (-0.26 dB/1°) to autumn 2017 (-0.12 dB/1°) and stays relatively constant after that, indicating that the processes during the first melt season are responsible for the shift in scattering behavior. The Old MYI at the eastern section has also the lowest slope (-0.12 to -0.14 dB/1°), which is not changing in 2017–2019. These findings for HH can be explained by the dominant scattering mechanisms for each ice type and polarization: Strongly angle-dependent surface scattering dominates for the smooth FYI in spring 2017, while volume scattering which is less impacted by different incidence angles, is characteristic for MYI, because desalination and percolation of melt water increases the fraction of air in the upper layers of ice, causing an increase in multiple scattering.

In this study, the incidence angle dependence of FYI HH backscatter ranges from -0.21 to -0.29 dB/1°, in agreement with the value of -0.24 dB/1° reported by Aldenhoff et al. (2020). The HV backscatter slope for FYI found in this study (-0.27 to -0.42 dB/1°) is much steeper than the value reported by Aldenhoff et al. (2020), but only slightly steeper than in other studies e.g., -0.24 dB/1° from Mäynen and Karvonen (2017) as summarized by Aldenhoff et al. (2020). The slope for HV in this study might be unreliable because the HV backscatter of the FYI is in the same order of magnitude as the noise floor at -28 dB. Aldenhoff et al. (2020) state that for low σ^0_{HV} the angular dependence could have been buried in the noise floor.

The mean HH backscatter values for FYI are lower than these of the MYI, explained by increasing volume scattering as the ice ages. The increase of scattering occurs over the first melt season in 2017, after which the winter backscatter remains stable. The higher mean values in autumn 2017 and autumn 2018 (-10.5 dB and -11.1 dB) compared to end of winter in the following years (-13.9 dB and -13.0 dB) is opposed to observations of increasing σ^0 with snow thickness made by (Gill et al., 2015), but they limited their study to FYI, where the brine volume is higher and can contribute to the wetting of the snow at the snow-ice interface. For MYI the influence of temperature might dominate; the snow cover will increase the temperature of the ice surface, potentially accounting for 2–3 dB lower scattering in springs than autumns. Another possible mechanism to decrease the backscatter throughout winter could be a decrease in the small-scale roughness of the surface ice layer.

Attempts have been made to predict summer melt pond fraction from winter backscatter over FYI and MYI, e.g., Scharien et al. (2017) found a significant negative correlation between pond fraction and backscatter. Here, in spring 2019, the smoother ice of the western section of the ice plug has similar mean backscatter, and similar incidence angle dependence as the much rougher Old MYI, while the two ice types experienced very different melt pond fractions in summer 2018. Predictions of summer melt pond fractions from backscatter would lead to be inaccurate estimates for this MYI case, exemplifying that information on ice type and roughness needs to be considered.

5.5 Role of climatic conditions for stability

Surface energy balance and weather conditions extracted from climate data from the ERA5 reanalysis product indicate that the inter-annual differences between 2016 and 2019 with ice plug breakups, and 2017 and 2018 with stable ice plug are higher summer temperatures, accompanied by earlier melt-onset in years with break-up. Differences in radiation balance, precipitation and wind speeds played only a secondary role in breakups.

This is opposed to Copland and Mueller (2017) who found that daily mean temperatures from Eureka show very little difference between years which featured complete plug breakups (e.g., 2005, 2007, 2008) and years with no breakups or with single plug fractures (e.g. 2004, 2006). To extend this into 2016–2019, we compare ERA5 temperatures at the ice plug to those at recorded by Eureka weather station (Fig. 5.2). While the mean daily summer temperatures measured at the station exceed the reanalysis temperatures for Eureka by 0.9–1.8°C, they also show much larger temperatures for years with breakup (4.9°C in 2016, 6.2°C in 2019) than for years with stable ice plug (2.7°C in 2017, 3.5°C in 2018; see Tab. B.7 in the Appendix).

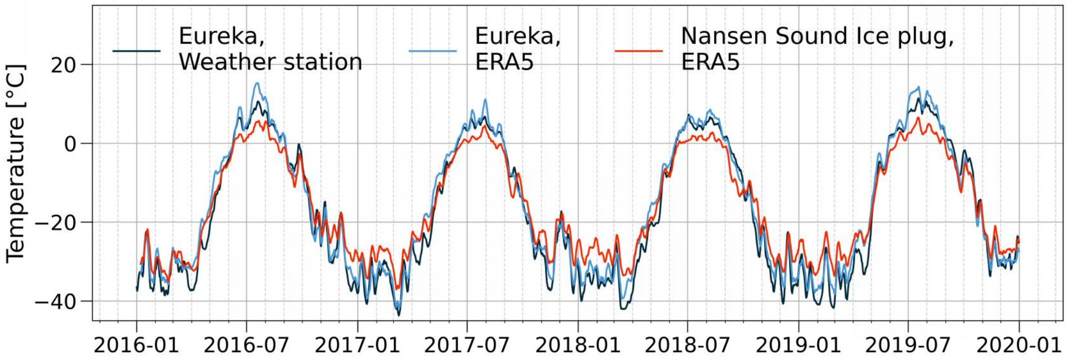

Fig. 5.2: 7-day moving averages of daily mean air temperatures recorded by Eureka weather station, and 2-m temperatures from ERA5 at Nansen Sound ice plug and Eureka.

In the past two decades, ice plug breakup events have occurred in young MYI (2005 and 2007) or in FYI (2008–2012, 2016). The breakups in 2005 and 2007 occurred in mid to late August, whereas in 2008 the breakup occurred at the beginning of August. Copland and Mueller (2017) attribute the difference in the timing to a correlation between sea ice age and thickness, which in turn determines the ice plug's ability to withstand melt and mechanical forcing. The timing of the breakups in this study do not support their hypothesis. The date of breakup was the beginning of August in 2016 and 2019 alike, whereas the plug in 2016 consisted of FYI and the plug in 2019 was thicker MYI.

Copland and Mueller (2017) add that an important variable associated with these recent simultaneous breakup events of Nansen and Sverdrup ice plug is "the presence of a lead of low sea ice concentration along the northern edges of the plugs, occurring as the pack ice is pushed away from the land" (p. 337). To verify this, we look at MODIS images of the ice concentration on about 20 km of ocean adjacent to the north of the ice plug. The ice concentration is classified as dense pack ice for days where the ice concentration exceeded 7/10. Ice cover is classified as sparse otherwise. The summer season (June–August) had 2 days of sparse ice cover in 2016, 12 days in 2017, 13 days in 2018, and 38 days in 2019. Notable is the long period of open water in July 2019, the month before the plug broke apart. This does not seem to be a necessary precondition for breakup, since in 2016 the northern ocean adjacent to the plug had a very low amount of open water days, but it might explain the similar timing of breakup in 2016 and 2019, despite thicker ice in 2019 and similar summer temperatures.

6 Summary

The roughness of sea ice is a key factor for modeling and measuring the interactions between ice, atmosphere, and ocean. MYI roughness evolution and melt season processes are interrelated, and sea ice roughness is sensitive to changing Arctic climatic conditions. This study evaluates sea ice thickness, surface and bottom roughness, and C-band SAR backscatter evolution of the semi-permanent landfast Nansen Sound ice plug throughout two melt season by airborne EM surveys carried out in springs 2017, 2018, and 2019 and dual polarization Sentinel-1 scenes.

For 2017 and 2019, 2D surface topography in the form of DEMs obtained with airborne laser scanning is available, complementing the single-beam altimeter surface profiles. The contribution of ALS to sea ice surface mapping in combination with EM measurements is evaluated. After adapting the filtering method for the altimeter profiles, a comparison between roughness parameters obtained from both instruments is undertaken and showed similar values for RMS height and skewness between the two instruments in both surveys on a scale of 50 m. About the evolution of surface roughness on a scale of 50 m can be summarized that the RMS height decreased slightly for the altimeter profiles while it stayed constant when using the ALS. The PSD method supports the ALS results of constant surface roughness, extending the spatial scale on which roughness was constant to 1–100 m. The unaltered topography, despite expected roughening from non-uniform summer ablation, was attributed to the snow cover, which masked those differences.

The mean thickness of the ice that formed in-situ in winter 2016/17 increased in thickness from 1.9 m in 2017, which is a typical value for landfast FYI in the CAA, to 2.4 m in 2019. Old MYI that originated from the arctic ocean and got incorporated into the ice plug upon freeze-up in 2016 had a mean thickness of 3.7 m. Melt pond distributions from summer Sentinel-2 true color images showed that spring RMS roughness did not co-vary with summer melt pond pattern. Furthermore, ice thickness was about 40 cm lower in pond covered sections of the three year old ice in 2019, while this difference was only 20 cm for the FYI of the ice plug in 2017. This is indicative of a non-uniform summer ablation influencing the evolution of ice thickness. Thinning in summer might not have been compensated by faster growth in winter.

The ice thickness was further used as a proxy for the bottom roughness. The percentage decrease in mean RMS height of the ice thickness profiles was about 30%, and therefore exceeds the change of surface roughness. The decrease in ice roughness is either a result from the differing flight tracks or an effect of slowing growth rates the thicker the ice gets.

The Sentinel-1 C-band backscatter is partly sensible to changes in surface topography, but also to bulk properties of the surface ice layers. For springs

2017, 2018, and 2019, as well as for autumns 2017 and 2019 we analyzed five EW scenes each by averaging the backscatter of the pixels coincident with the EM surveys. Average σ^0_{HH} of the ice plug increased from -21 to -13 dB and σ^0_{HV} increased from -29 to -23 dB. The angular dependence of HH backscatter decreased over the first melt season in 2017 from -0.26 dB/1° to -0.15 dB/1°, and remained the same from autumn 2017 to spring 2019. This decreasing angular dependence and the increasing backscatter is expected for enhanced volume scattering from the surface ice layers when porosity an air content increased after the first summer season. The HV backscatter is close to the noise floor therefore, angular dependence is unreliable. The seasonal landfast FYI on Nansen Sound has stable mean backscatter around -20 dB.

This work extends the documentation of Nansen Sound ice plug events, spanning 1962–2016 in Copland and Mueller (2017), to 2019. ERA5 Land climate reanalysis data was consulted to find reasons for the stability of the ice plug in 2017 and 2018, which is an exception in the past two decade. The survival of the ice plug was attributed to lower mean summer temperatures and thereby less MDDs, with significantly reduced ablation. Also, the later onset of surface melting, and shortened time periods of open water might have contributed to the stability of the ice plug in 2017 and 2018.

Declaration of Authorship

Declaration of honor

I hereby confirm on my honor that I personally prepared the present academic work and carried out myself the activities directly involved with it. I also confirm that I have used no resources other than those declared. All formulations and concepts adopted literally or in their essential content from printed, unprinted or Internet sources have been cited according to the rules for academic work and identified by means of footnotes or other precise indications of source. The support provided during the work, including significant assistance from my supervisor has been indicated in full. The academic work has not been submitted to any other examination office authority. The work is submitted in printed and electronic form. I confirm that the content of the digital version is completely identical to that of the printed version.

Bremen, ______________ ______________________________
Date Signature

Declaration of publication

☐ I hereby agree, that my thesis will be available for third-party review for the purpose of academic research.

☐ I hereby agree, that my thesis will be available after 30 years (§7Abs. 2 BremArchG) in the university archive for third-party review for the purpose of academic research.

✗ I hereby do not agree, that my thesis will be available for third-party review for the purpose of academic research.

Bremen, ______________ ______________________________
Date Signature

Acknowledgements

I would first like to thank my thesis adviser Prof. Dr. Christian Haas. His enthusiasm immediately caught me, when out on the glacier studying ice and snow up close. I am grateful for the guidance, inspiration and support, and the opportunities I received since then. He allowed this thesis to be my own work but steered me in the right direction whenever he thought I needed it.
In addition, I want to thank the Sea Ice Physics group at AWI as a competent contact for all questions about data processing. I am looking forward to coffee breaks in person!
I would like to thank Dr. Christian Melsheimer from the Institute of Environmental Physics, University of Bremen, who readily agreed to assess my work.
Finally, I must express my gratitude to my friends for providing me with continuous encouragement and feedback throughout my years of study and through the process of writing this thesis. Thank you,

Mara Neudert

A Appendix Figures

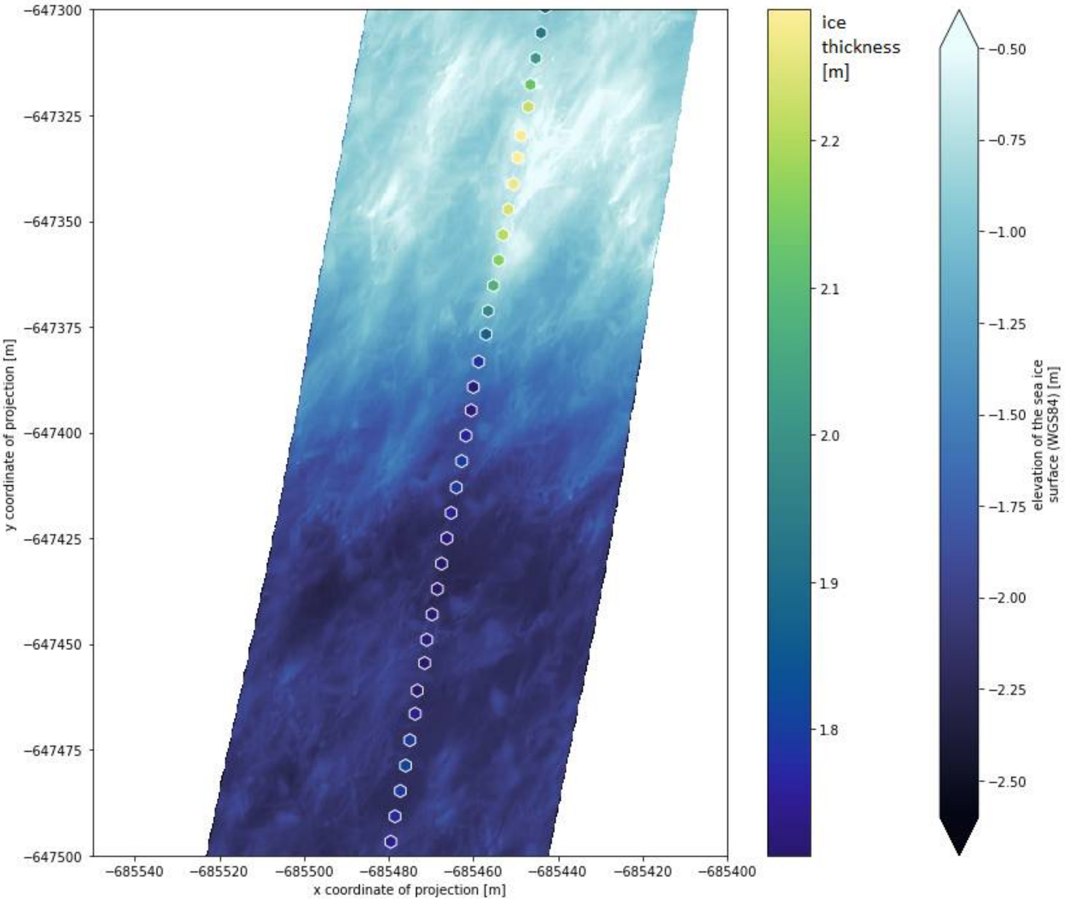

FIG. A.1: Section of the MYI ALS DEM and ice thicknesses (2017). The location corresponds to 92 km on the reference line shown in Fig. 3.10, where nadir elevations jump to a 1 m higher level. This was later attributed to incomplete GPS data.

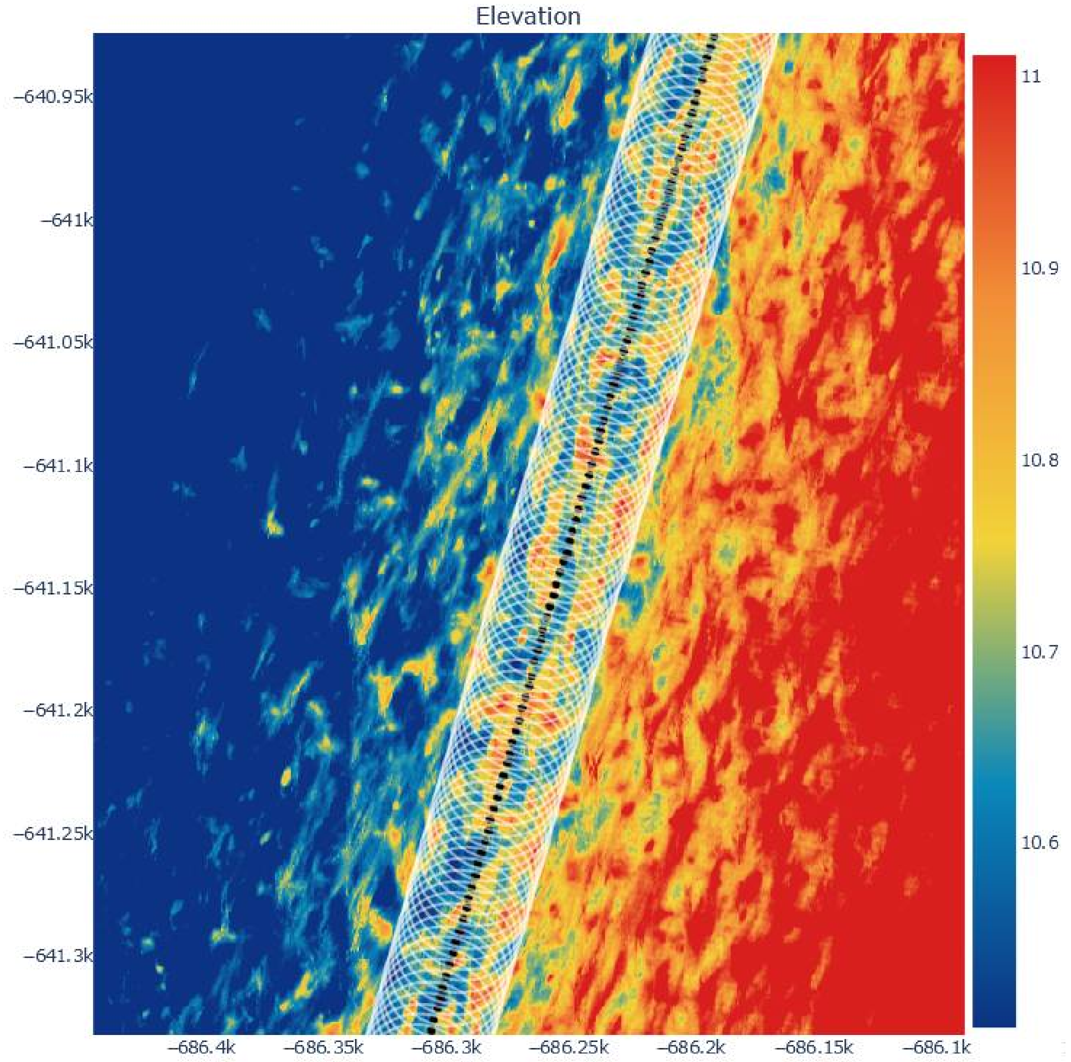

FIG. A.2: Section of the MYI ALS DEM (2017). x-axis shows the x coordinate of projection [m], y-axis the y coordinate of projection [m]. The are given in elevations [m]. The DEM is titled in across-track direction, which does not notably influence the DEM within the footprint of the EM measurements (white circles).

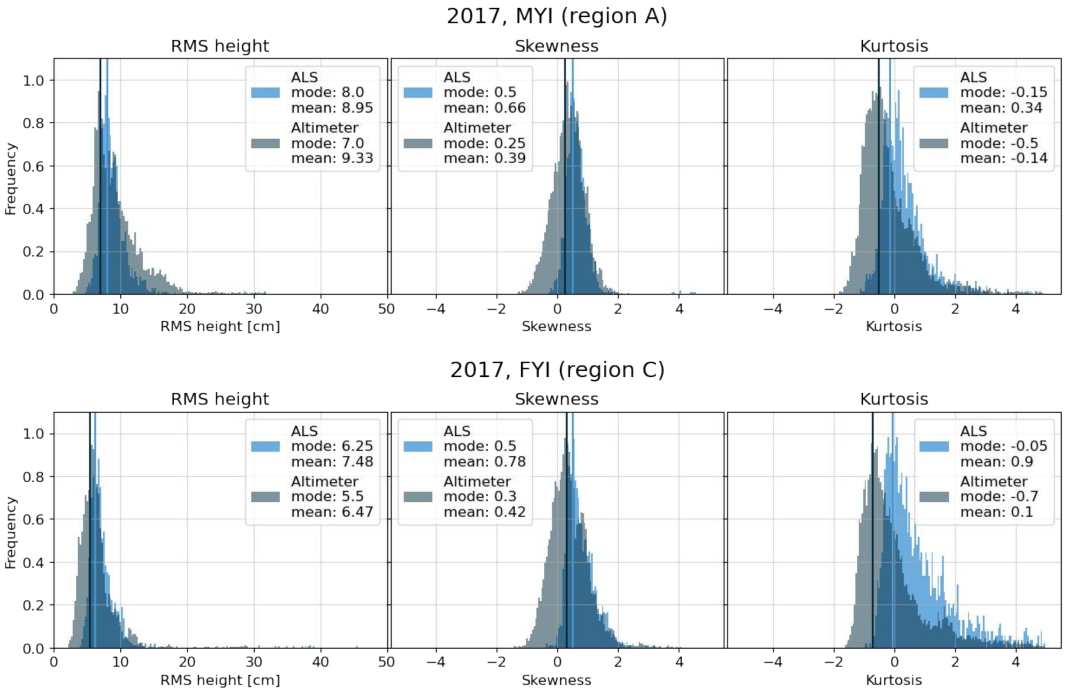

FIG. A.3: Histograms of ALS- and altimeter-derived surface roughness parameters for 2017.

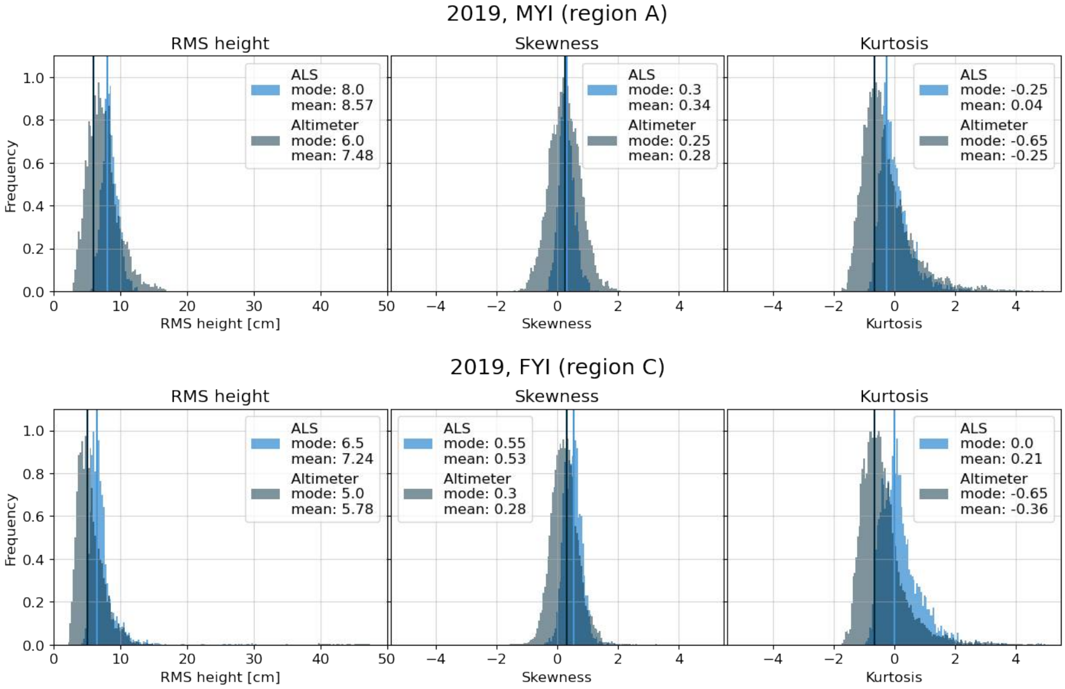

FIG. A.4: Histograms of ALS- and altimeter-derived surface roughness parameters for 2019.

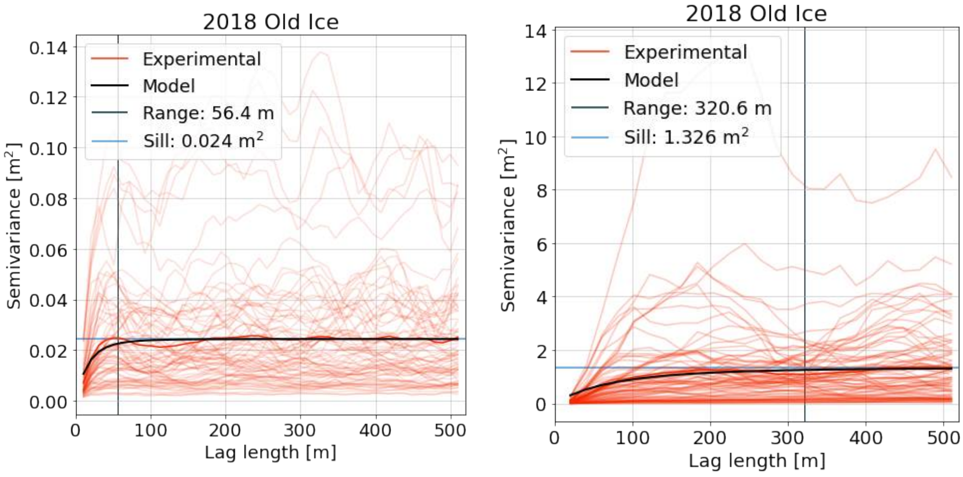

Variogram of surface height

Variogram of ice thickness

FIG. A.5: Semivariograms of the Old Ice in 2018

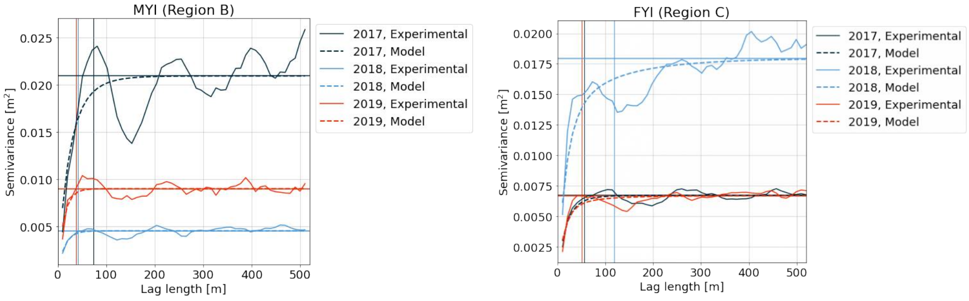

MYI

FYI

FIG. A.6: Mean semivariograms of surface heights

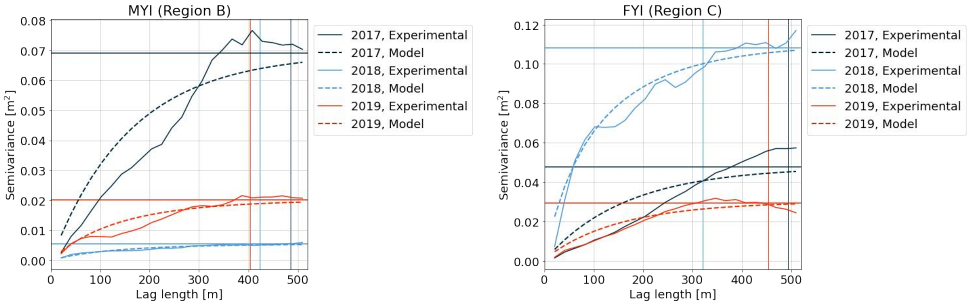

MYI

FYI

FIG. A.7: Mean semivariograms of ice thickness

B Appendix Tables

B.1 Additional tables for Chapter 3

Table B.1: List of the S1 products used

Product name	Acquisition date
S1B_EW_GRDM_1SDH_20170329T132933_20170329T133033_004924_0089B7_AEC1	2017-03-29
S1B_EW_GRDM_1SDH_20170330T141051_20170330T141151_004939_008A23_DA68	2017-03-30
S1B_EW_GRDM_1SDH_20170331T145115_20170331T145215_004954_008A93_3063	2017-03-31
S1B_EW_GRDM_1SDH_20170402T143523_20170402T143623_004983_008B67_76FC	2017-04-02
S1B_EW_GRDM_1SDH_20170403T133742_20170403T133842_004997_008BD2_9886	2017-04-03
S1B_EW_GRDM_1SDH_20170905T143531_20170905T143631_007258_00CCC0_D410	2017-09-05
S1B_EW_GRDM_1SDH_20170904T135425_20170904T135525_007243_00CC4D_435F	2017-09-04
S1B_EW_GRDM_1SDH_20170902T141100_20170902T141200_007214_00CB75_E96C	2017-09-02
S1B_EW_GRDM_1SDH_20170901T132956_20170901T133056_007199_00CB0C_CC00	2017-09-01
S1A_EW_GRDM_1SDH_20170902T132236_20170902T132341_018197_01E94C_8F86	2017-09-02
S1B_EW_GRDM_1SDH_20180403T134627_20180403T134727_010320_012C80_6497	2018-04-03
S1B_EW_GRDM_1SDH_20180401T140247_20180401T140341_010291_012B77_1135	2018-04-01
S1B_EW_GRDM_1SDH_20180328T143529_20180328T143629_010233_01298F_59A8	2018-03-28
S1B_EW_GRDM_1SDH_20180406T141058_20180406T141153_010364_012DE3_E446	2018-04-06
S1A_EW_GRDM_1SDH_20180406T132235_20180406T132339_021347_024BD6_EFD3	2018-04-06
S1B_EW_GRDM_1SDH_20180904T140255_20180904T140350_012566_0172EF_C5BC	2018-09-04
S1B_EW_GRDM_1SDH_20180903T132152_20180903T132252_012551_01727C_EC92	2018-09-03
S1B_EW_GRDM_1SDH_20180902T141918_20180902T142018_012537_01720D_91E8	2018-09-02
S1B_EW_GRDM_1SDH_20180901T133811_20180901T133911_012522_017193_E91A	2018-09-01
S1B_EW_GRDM_1SDH_20180905T144346_20180905T144447_012581_017369_1F5D	2018-09-05
S1A_EW_GRDM_1SDH_20190401T132241_20190401T132345_026597_02FB88_B44A	2019-04-01
S1B_EW_GRDM_1SDH_20190402T131341_20190402T131441_015628_01D4DD_9BBA	2019-04-02
S1B_EW_GRDM_1SDH_20190403T135430_20190403T135530_015643_01D55E_6DD3	2019-04-03
S1B_EW_GRDM_1SDH_20190402T145141_20190402T145241_015629_01D4E6_DD64	2019-04-02
S1B_EW_GRDM_1SDH_20190401T141105_20190401T141205_015614_01D465_4CC6	2019-04-01

Table B.2: Mean incidence angle $\overline{\theta}$ and mean backscatter $\overline{\sigma^0}$ for each season and region for pixels coincident with the EM survey in the respective year.

Polarisation	Year	Region	Month	$\overline{\theta}$ [°]	$\overline{\sigma^0}$ [dB]
HH	2017	FYI	April	30.39	-19.76
			September	34.04	-20.07
		ice plug	April	33.35	-20.78
			September	36.82	-10.54
	2018	FYI	April	32.94	-17.14
			September	32.49	-18.02
		ice plug	April	35.62	-13.95
			September	35.20	-11.13
	2019	FYI	April	34.05	-20.66
		ice plug	April	36.73	-13.00
HV	2017	FYI	April	30.39	-28.32
			September	34.04	-29.28
		ice plug	April	33.35	-28.95
			September	36.82	-22.15
	2018	FYI	April	32.94	-26.14
			September	32.49	-28.00
		ice plug	April	35.62	-25.26
			September	35.20	-21.67
	2019	FYI	April	34.05	-29.51
		ice plug	April	36.73	-23.20

Table B.3: Slopes and correlation coefficients of the linear regression for backscatter dependence on incidence angle $\sigma^0_{pq}(\theta)$.

Polarisation	Year	Region	Month	slope [dB/1°]	R^2
HH	2017	FYI	April	-0.29	-0.99
			September	-0.48	-0.70
		ice plug	April	-0.26	-0.99
			September	-0.12	-0.96
	2018	FYI	April	-0.21	-0.90
			September	-0.63	-0.68
		ice plug	April	-0.15	-0.92
			September	-0.17	-0.99
	2019	FYI	April	-0.24	-1.00
		ice plug	April	-0.14	-0.98
HV	2017	FYI	April	-0.41	-0.88
			September	-0.37	-0.84
		ice plug	April	-0.42	-0.94
			September	-0.11	-0.85
	2018	FYI	April	-0.27	-0.81
			September	-0.24	-0.60
		ice plug	April	-0.17	-0.93
			September	-0.16	-0.94
	2019	FYI	April	-0.30	-0.94
		ice plug	April	-0.14	-0.99

Table B.4: ERA5 variables and their units

name	units	old name	short name
10 metre U wind component	m s^{-1}		u_{10}
10 metre V wind component	m s^{-1}		v_{10}
2 metre temperature	K	-	T_{2m}
Surface pressure	P	surface_air_pressure	sp
Total precipitation	m	-	tp
Surface latent heat flux	J m^{-2}	surface_upward_latent_heat_flux	slhf
Surface net solar radiation	J m^{-2}	surface_net_downward_shortwave_flux	ssr
Surface net thermal radiation	J m^{-2}	surface_net_upward_longwave_flux	str
Surface sensible heat flux	J m^{-2}	surface_upward_sensible_heat_flux	sshf

Table B.5: Wind speed during break up period in August 2016

	Date	Wind speed [m s^{-1}]
0	2016-08-04 00:00:00	4.1
1	2016-08-04 12:00:00	1.7
2	2016-08-05 00:00:00	4.2
3	2016-08-05 12:00:00	3.2
4	2016-08-06 00:00:00	4.6

Table B.6: Wind speed during break up period in August 2019

	Date	Wind speed [m s^{-1}]
0	2019-08-01 00:00:00	5.5
1	2019-08-01 12:00:00	4.8
2	2019-08-02 00:00:00	5.2
3	2019-08-02 12:00:00	1.9
4	2019-08-03 00:00:00	3.6
5	2019-08-03 12:00:00	6.3
6	2019-08-04 00:00:00	3.1
7	2019-08-04 12:00:00	1.1
8	2019-08-05 00:00:00	1.6
9	2019-08-05 12:00:00	2.0
10	2019-08-06 00:00:00	2.5
11	2019-08-06 12:00:00	3.1
12	2019-08-07 00:00:00	2.6

B.2 Additional tables for Chapter 5

Table B.7: Seasonal mean ERA5 temperatures at Nansen Sound ice plug, Eureka and mean temperatures from daily weather station data for Eureka. Weather station data was downloaded via Environment and Canada (2021).

	Period		ERA 5		Weather station	$T^{E}_{ERA5} - T^{E}_{WS}$
	Start	End	Ice plug T^{IP}_{ERA5}	Eureka T^{E}_{ERA5}	Eureka T^{E}_{WS}	
s	2016-06-01	2016-08-31	1.6	6.6	4.9	1.7
s	2017-06-01	2017-08-31	0.2	3.8	2.7	1.1
s	2018-06-01	2018-08-31	0.4	4.4	3.5	0.9
s	2019-06-01	2019-08-31	2.2	8.0	6.2	1.8
w	2016-09-01	2017-05-31	-21.3	-23.4	-24.5	1.2
w	2017-09-01	2018-05-31	-22.3	-24.6	-26.4	1.8
w	2018-09-01	2019-05-31	-21.7	-23.6	-25.3	1.8

Bibliography

Aldenhoff, Wiebke, Leif EB Eriksson, Yufang Ye, and Céline Heuzé (2020). "First-Year and Multiyear Sea Ice Incidence Angle Normalization of Dual-Polarized Sentinel-1 SAR Images in the Beaufort Sea". In: *IEEE Journal of Selected Topics in Applied Earth Observations and Remote Sensing* 13, pp. 1540–1550.

Armstrong, Terence (1972). "World Meteorological Organization. WMO sea-ice nomenclature. Terminology, codes and illustrated glossary. Edition 1970. Geneva, Secretariat of the World Meteorological Organization, 1970.[ix], 147 p.[including 175 photos]+ corrigenda slip.(WMO/OMM/BMO, No. 259, TP. 145.)" In: *Journal of Glaciology* 11.61, pp. 148–149.

Beckers, Justin F, Angelika HH Renner, Gunnar Spreen, Sebastian Gerland, and Christian Haas (2015). "Sea-ice surface roughness estimates from airborne laser scanner and laser altimeter observations in Fram Strait and north of Svalbard". In: *Annals of Glaciology* 56.69, pp. 235–244.

Belter, H Jakob, Thomas Krumpen, Stefan Hendricks, Jens Hoelemann, Markus A Janout, Robert Ricker, and Christian Haas (2020). "Satellite-based sea ice thickness changes in the Laptev Sea from 2002 to 2017: comparison to mooring observations". In: *The Cryosphere* 14.7, pp. 2189–2203.

Bendat, JS and AG Piersol (1986). Random data, 2n New York.

Braithwaite, Roger J. (1995). "Positive degree-day factors for ablation on the Greenland ice sheet studied by energy-balance modelling". In: *Journal of Glaciology* 41.137, 153–160.

Brown, Stephen R (1987). "A note on the description of surface roughness using fractal dimension". In: *Geophysical Research Letters* 14.11, pp. 1095–1098.

Carsey, Frank D (1992). Microwave remote sensing of sea ice. American Geophysical Union.

Comiso, Josefino C (2012). "Large decadal decline of the Arctic multiyear ice cover". In: *Journal of Climate* 25.4, pp. 1176–1193.

Congedo, Luca (2016). "Semi-automatic classification plugin documentation". In: *Release* 4.0.1, p. 29.

Copland, Luke and Derek Mueller (2017). Arctic ice shelves and ice islands. Springer.

Dauginis, Alicia L.A. and Laura C. Brown (2021). "Sea ice and snow phenology in the Canadian Arctic Archipelago from 1997 to 2018". In: *Arctic Science* 7.1, pp. 182–207. 10.1139/as-2020-0024.

Ebert, Elizabeth E and Judith A Curry (1993). "An intermediate one-dimensional thermodynamic sea ice model for investigating ice-atmosphere interactions". In: *Journal of Geophysical Research: Oceans* 98.C6, pp. 10085–10109.

ECMWF (2021). URL: `https://cds.climate.copernicus.eu/cdsapp#!/home`.

Eicken, H, TC Grenfell, DK Perovich, JA Richter-Menge, and K Frey (2004). “Hydraulic controls of summer Arctic pack ice albedo”. In: *Journal of Geophysical Research: Oceans* 109.C8.

Environment and Climate Change Canada (2021). Past Weather and Climate. URL: `https://climate.weather.gc.ca/historical_data/search_historic_data_e.html`.

ESA (2015a). Sentinel-1 Data Products. URL: `https://sentinel.esa.int/web/sentinel/missions/sentinel-1/data-products`.

— (2015b). “SENTINEL-2 User Handbook”. In: *ESA Standard Document* 64.

— (2021). Copernicus Open Access Hub. URL: `https://scihub.copernicus.eu/dhus/#/home`.

Filipponi, Federico (2019). “Sentinel-1 GRD preprocessing workflow”. In: *Multidisciplinary Digital Publishing Institute Proceedings*. Vol. 18. 1, p. 11.

Florescu, I. (2014). Probability and Stochastic Processes. Wiley.

Gill, Jagvijay PS, John J Yackel, Torsten Geldsetzer, and M Christopher Fuller (2015). “Sensitivity of C-band synthetic aperture radar polarimetric parameters to snow thickness over landfast smooth first-year sea ice”. In: *Remote Sensing of Environment* 166, pp. 34–49.

Gneiting, Tilmann, Hana Ševčíková, and Donald B Percival (2012). “Estimators of fractal dimension: Assessing the roughness of time series and spatial data”. In: *Statistical Science*, pp. 247–277.

Haas, Christian and Stephen EL Howell (2015). “Ice thickness in the Northwest Passage”. In: *Geophysical Research Letters* 42.18, pp. 7673–7680.

Haas, Christian, John Lobach, Stefan Hendricks, Lasse Rabenstein, and Andreas Pfaffling (2009). “Helicopter-borne measurements of sea ice thickness, using a small and lightweight, digital EM system”. In: *Journal of Applied Geophysics* 67.3, pp. 234–241.

Haas, Christian, Andreas Pfaffling, Stefan Hendricks, Lasse Rabenstein, Jean-Louis Etienne, and Ignatius Rigor (2008). “Reduced ice thickness in Arctic Transpolar Drift favors rapid ice retreat”. In: *Geophysical Research Letters* 35.17.

Hersbach, Hans, Bill Bell, Paul Berrisford, Shoji Hirahara, András Horányi, Joaquín Muñoz-Sabater, Julien Nicolas, Carole Peubey, Raluca Radu, Dinand Schepers, et al. (2020). “The ERA5 global reanalysis”. In: *Quarterly Journal of the Royal Meteorological Society* 146.730, pp. 1999–2049.

Hibler, William D and Leonard A LeSchack (1972). “Power spectrum analysis of undersea and surface sea-ice profiles”. In: *Journal of Glaciology* 11.63, pp. 345–356.

Hibler III, WD (1972). “Removal of aircraft altitude variation from laser profiles of the Arctic ice pack”. In: *Journal of Geophysical Research* 77.36, pp. 7190–7195.

Howell, Stephen EL and Mike Brady (2019). “The dynamic response of sea ice to warming in the Canadian Arctic Archipelago”. In: *Geophysical Research Letters* 46.22, pp. 13119–13125.

Howell, Stephen EL, Frédéric Laliberté, Ron Kwok, Chris Derksen, and Joshua King (2016). “Landfast ice thickness in the Canadian Arctic Archipelago from observations and models”. In: *The Cryosphere* 10.4, pp. 1463–1475.

Iacozza, John and David G Barber (1999). “An examination of the distribution of snow on sea-ice”. In: *Atmosphere-Ocean* 37.1, pp. 21–51.

Jeffers, Sharon, Tom A Agnew, Bea Taylor Alt, Roger De Abreu, and Steve McCourt (2001). “Investigating the anomalous sea-ice conditions in the Canadian High Arctic (Queen Elizabeth Islands) during summer 1998”. In: *Annals of Glaciology* 33, pp. 507–512.

Jeffries, Martin O, Greta J Reynolds, and John M Miller (1992). “First Landsat multi-spectral scanner images of the Canadian Arctic north of 80 N”. In: *Polar record* 28.164, pp. 1–6.

Jutila, Arttu, Joshua King, John Paden, Robert Ricker, Stefan Hendricks, Chris Polashenski, Veit Helm, Tobias Binder, and Christian Haas (2021). “High-Resolution Snow Depth on Arctic Sea Ice From Low-Altitude Airborne Microwave Radar Data”. In: *IEEE Transactions on Geoscience and Remote Sensing.*

Kern, Stefan, K Khvorostovsky, H Skourup, E Rinne, ZS Parsakhoo, V Djepa, P Wadhams, and S Sandven (2015). “The impact of snow depth, snow density and ice density on sea ice thickness retrieval from satellite radar altimetry: results from the ESA-CCI Sea Ice ECV Project Round Robin Exercise”. In: *Cryosphere* 9, pp. 37–52.

Landy, Jack, Jens Ehn, Megan Shields, and David Barber (2014). “Surface and melt pond evolution on landfast first-year sea ice in the Canadian Arctic Archipelago”. In: *Journal of Geophysical Research: Oceans* 119.5, pp. 3054–3075.

Landy, Jack C, Jens K Ehn, and David G Barber (2015). “Albedo feedback enhanced by smoother Arctic sea ice”. In: *Geophysical Research Letters* 42.24, pp. 10–714.

Liu, Chengyu, Jinlong Chao, Wei Gu, Lantao Li, and Yingjun Xu (2014). “On the surface roughness characteristics of the land fast sea-ice in the Bohai Sea”. In: *Acta Oceanologica Sinica* 33.7, pp. 97–106.

Magsipoc, Earl, Qi Zhao, and Giovanni Grasselli (2020). 2D and 3D roughness characterization.

Maslanik, JA, C Fowler, J Stroeve, S Drobot, J Zwally, D Yi, and W Emery (2007). “A younger, thinner Arctic ice cover: Increased potential for rapid, extensive sea-ice loss”. In: *Geophysical Research Letters* 34.24.

Maykut, Gary A and Norbert Untersteiner (1971). “Some results from a time-dependent thermodynamic model of sea ice”. In: *Journal of Geophysical Research* 76.6, pp. 1550–1575.

Melling, Humfrey (2002). “Sea ice of the northern Canadian Arctic Archipelago”. In: *Journal of Geophysical Research: Oceans* 107.C11, pp. 2–1.

NASA (2021a). Earthdata FAQ. URL: `https://earthdata.nasa.gov/faq/lance-faq#ed-CRvsSR`.

— (2021b). NASA Worldview. URL: `https://worldview.earthdata.nasa.gov/`.

Nasonova, Sasha, Randall K Scharien, Christian Haas, and Stephen EL Howell (2018). “Linking regional winter sea ice thickness and surface roughness to spring melt pond fraction on landfast Arctic sea ice”. In: *Remote Sensing* 10.1, p. 37.

National Geospatial Intelligence Agency (2021). EGM96 Geoid Calculator. URL: `https://earth-info.nga.mil/GandG/update/index.php?dir=wgs84&action=egm96-geoid-calc`.

Perovich, DK, TC Grenfell, B Light, and PV Hobbs (2002). “Seasonal evolution of the albedo of multiyear Arctic sea ice”. In: *Journal of Geophysical Research: Oceans* 107.C10, SHE–20.

Pfaffling, Andreas, Christian Haas, and James E Reid (2007). “Direct helicopter EM—Sea-ice thickness inversion assessed with synthetic and field data”. In: *Geophysics* 72.4, F127–F137.

Ricker, Robert, Stefan Hendricks, Veit Helm, Henriette Skourup, and Malcom Davidson (2014). “Sensitivity of CryoSat-2 Arctic sea-ice freeboard and thickness on radar-waveform interpretation”. In: *The Cryosphere* 8.4, pp. 1607–1622.

Sadler, HE and HV Serson (1981). Observations on a Plug of Old Sea Ice in the Entrance to Nansen Sound, Ellesmere Island. Tech. rep. Defence Research Establishment Pacific Victoria (British Columbia).

Scharien, Randall K, Rebecca Segal, Sasha Nasonova, Vishnu Nandan, Stephen EL Howell, and Christian Haas (2017). “Winter Sentinel-1 backscatter as a predictor of spring Arctic sea ice melt pond fraction”. In: *Geophysical Research Letters* 44.24, pp. 12–262.

Segal, Rebecca A, Randall K Scharien, Silvie Cafarella, and Andrew Tedstone (2020). “Characterizing winter landfast sea-ice surface roughness in the Canadian Arctic Archipelago using Sentinel-1 synthetic aperture radar and the Multi-angle Imaging SpectroRadiometer”. In: *Annals of Glaciology*, pp. 1–15.

Serson, HV (1972). “Investigation of a plug of multi-year old sea ice in the mouth of Nansen Sound. Defence Research Establishment, Ottawa”. In: *Technical Note* 726, p. 4.

Shokr, Mohammed and Nirmal Sinha (2015). Sea ice: physics and remote sensing. John Wiley & Sons.

Stover, John C (2012). “Optical scattering: measurement and analysis”. In: Society of Photo-Optical Instrumentation Engineers.

Thomas, David N and Gerhard S Dieckmann (2008). Sea ice: an introduction to its physics, chemistry, biology and geology. John Wiley & Sons.

Torres, Ramon, Paul Snoeij, Dirk Geudtner, David Bibby, Malcolm Davidson, Evert Attema, Pierre Potin, Björn Rommen, Nicolas Floury, Mike Brown, et al. (2012). “GMES Sentinel-1 mission”. In: *Remote Sensing of Environment* 120, pp. 9–24.

Tschudi, Mark A, Julienne C Stroeve, and J Scott Stewart (2016). “Relating the age of Arctic sea ice to its thickness, as measured during NASA’s ICESat and IceBridge campaigns”. In: *Remote Sensing* 8.6, p. 457.

Ulaby, Fawwaz and David Long (2015). Microwave radar and radiometric remote sensing. Artech House.

Von Saldern, Carola, Christian Haas, and Wolfgang Dierking (2006). “Parameterization of Arctic sea-ice surface roughness for application in ice type classification”. In: *Annals of glaciology* 44, pp. 224–230.

Webster, Richard and Margaret A Oliver (2007). Geostatistics for environmental scientists. John Wiley & Sons.

Welch, Peter (1967). “The use of fast Fourier transform for the estimation of power spectra: a method based on time averaging over short, modified periodograms”. In: *IEEE Transactions on audio and electroacoustics* 15.2, pp. 70–73.

Wikipedia (2021). k-means clustering. URL: `https://en.wikipedia.org/wiki/K-means_clustering`.

WMO-IOC et al. (2014). “Ice Chart Colour Code Standard, Version 1.0, 2014.” In.